Local Regulation of Interchange Turbulence in a Dipole-Confined Plasma Torus using Current Injection Feedback

Thomas Maximillian Roberts

Submitted in partial fulfillment of the
Requirements for the degree
of Doctor of Philosophy
in the Graduate School of Arts and Sciences

COLUMBIA UNIVERSITY

2015

ABSTRACT

Local Regulation of Interchange Turbulence in a Dipole-Confined Plasma Torus using Current Injection Feedback

Thomas Maximillian Roberts

Turbulence in plasma confined by a magnetic dipole is dominated by interchange fluctuations with complex dynamics and short spatial coherence. We report the first use of local current-collection feedback to modify, amplify, and suppress these fluctuations. The spatial extent of turbulence regulation is limited to a correlation length near the collector. Changing the gain and phase of collection results in power either extracted from or injected into the turbulence. This mechanism is analogous to the magnetospheric-ionospheric coupling by field-aligned currents. The measured plasma response shows some agreement with calculations of the linear response of global interchange-like MHD and entropy modes to current-collection feedback.

Contents

List of Figures vi

List of Tables xv

1 Introduction 1

1.1 Dipole-Confined Plasmas . . . 1

1.1.1 Planetary Magnetospheres . . . 2

1.1.2 Laboratory Magnetospheres . . . 4

1.2 Basis Physics of Dipole Confined Plasmas . . . 6

1.2.1 Charged Particle Motion . . . 6

1.2.2 Fluid Description and the Interchange Instability . . . 8

1.2.3 Interchange Turbulence in Dipole Plasmas . . . 9

1.3 Feedback in Plasmas . . . 10

1.3.1 Feedback on Interchange Unstable Plasmas . . . 10

1.3.2 Feedback on Turbulent Plasmas . . . 11

1.4 Organization . . . 13

2 The Collisionless Terrella Experiment 14

2.1 Magnetic Field . . . 16

2.2 Electron Cyclotron Resonance Heating . . . 18

2.3 Diagnostics . . . 20

2.3.1 Floating Potential Probes . . . 20
2.3.2 Biasing Electrodes . . . 20
2.3.3 Langmuir Probe . . . 21
2.3.4 Polar Imager . . . 21
2.3.5 Rake Array . . . 23
2.4 Turbulent Plasma Parameters . . . 24

3 Feedback System Design **28**
3.1 Principles of Feedback . . . 28
3.2 Feedback System Design . . . 30
3.2.1 Overall Feedback Circuit Design . . . 30
3.2.2 Pre-Amplifier/Buffer . . . 31
3.2.3 High-Pass Filter . . . 32
3.2.4 All-Pass Filter (Phase Shifter) . . . 34
3.2.5 Measured Performance of Circuit . . . 36
3.3 Feedback Configuration in the CTX Device . . . 39

4 Plasma Response to Feedback **41**
4.1 Testing the Open-loop Response: Feedforward . . . 41
4.2 Closing the Loop: Feedback . . . 46
4.3 Phase Scan . . . 50
4.4 Gain Scan . . . 55
4.5 Power Flow . . . 57
4.6 Observations of Feedback with Azimuthal Angle . . . 64
4.7 Varying the Azimuthal Separation . . . 69
4.8 Zero Net Injected Current . . . 71
4.9 High-Pass Filtered Feedback . . . 73

5 Gyro-Fluid Model **75**

5.1 Building the Model: Gyro-Fluid Equations . . . 76

5.1.1 Particle Continuity . . . 77

5.1.2 Current Constraint . . . 79

5.1.3 Pressure Dynamics . . . 81

5.1.4 Linearized Equations . . . 82

5.1.5 Normalized Equations . . . 83

5.1.6 Localized Equations . . . 85

5.1.7 Including the Feedback . . . 87

5.2 Solving the Global Eigenvalue Problem . . . 89

5.2.1 Equations to be Solved . . . 89

5.2.2 Equilibrium Profiles . . . 90

5.2.3 Matrix Structure . . . 92

5.2.4 Eigensystem . . . 94

5.2.5 The Addition of Current Injection . . . 96

5.2.6 Quantifying the Effects of Current Injection . . . 98

5.2.7 Phase and Gain Scans . . . 99

5.3 Comparing the Model to the Experiment . . . 101

6 Conclusion **103**

6.1 Discussion of Results . . . 104

6.2 Questions and Opportunities for Continued Research . . . 106

Bibliography **108**

Appendix A CTX Parameters **113**

Appendix B Dipole Coordinates **116**

B.1 Intro to Generalized Coordinates . . . 116

B.1.1 Test it out: Spherical Coordinates . . . 119
B.2 Generalized Coordinates to Dipole Coordinates . . . 121
B.3 Dipole Field Lines . . . 123
B.4 Flux Tube Integration . . . 123

Appendix C CTX Equipment and Running **125**
C.1 Starting Up Procedures for Running CTX . . . 125
C.2 Vacuum Procedures . . . 128
C.2.1 Going "Up to Air" . . . 128
C.2.2 Pump Down . . . 129

Appendix D Polar Imager **131**

Appendix E Rake Array **133**

Appendix F Filter Theory **138**
F.1 Introduction to Filters . . . 138
F.2 Active Filters . . . 141

Appendix G Additional Circuits **144**
G.1 Triggering Circuit . . . 144
G.2 Isolation Transformer . . . 145

Appendix H HEIsim Equations and Numerical Methods **146**
H.1 Equations . . . 146
H.1.1 Poisson's Equation . . . 147
H.1.2 Cold Ion Fluid . . . 148
H.1.3 Kinetic Electron Dynamics . . . 149
H.1.4 Normalization . . . 150
H.2 Numerical Techniques . . . 151

H.2.1 Trapezoidal Leap-Frog Method 151
H.2.2 Nonlinear Solve for $\frac{\partial \hat{\Phi}}{\partial t}$ 152
H.2.3 Flux-Corrected Transport Algorithm 153
H.2.4 Numerical Dissipation in Potential 154
H.3 Particle Conserving Source/Sink 155

List of Figures

1.1 Left, pressure from the solar wind distorted the Earth's magnetosphere. Right, aurora on Saturn's southern pole indicating the presence of a magnetosphere. . . . 2

1.2 Left, convection in the magnetosphere is transferred to and damped in the ionosphere. Right, field aligned currents connecting the magnetosphere to the ionosphere. 3

1.3 a) Birkeland's terrella experiment. b) Shaikhislamov's ionospheric current experiment. c) An image of a plasma in CTX. d) A plasma confined in a levitated dipole field (LDX). 5

1.4 The three particle motions in a dipole magnetic field; gyration, bounce and drift. Related to each is an adiabatic invariant; μ for gyro motion, J for bounce motion, and ψ for drift motion. 6

1.5 Left, experimental configuration for Prater's flute-mode suppression work. Middle and right, normalized mode amplitude with gain and phase (respectively), showing strong suppression of the single mode. 10

1.6 a) Experimental configuration on the TEXT tokamak. b) The positioning of driver and sensors on magnetic surface. c) The local response to feedback shows amplification and suppression, while the influence is reduced further away (d). 12

2.1 Top: Photo of the CTX device. Bottom: Rendering of the CTX vacuum chamber, cut away to expose the magnet and probes inside. 15

2.2 Cross-section of dipole magnet current-winding. Six coils are wound into 12x14 pancakes such that the cabling can be all internal. 16
2.3 The spherical and flux coordinates in the dipole geometry. The electron cyclotron resonance layer is also highlighted. 17
2.4 The waveguide connecting the magnetron to the vacuum chamber. Directional microwave antennas measure input and reflected microwave power. 19
2.5 Biasing electrode with a collection area of $\sim 20\,\mathrm{cm}^2$ will be the "actuator" for feedback. Notice the 12" alumina shaft which connects to the stainless steel feedthrough shaft. 21
2.6 Left, a photograph of the Polar Imager in the CTX vacuum chamber. Right, a depiction of the Polar Imager with the magnetic field lines (red) and surfaces of constant B (blue). The 96 gridded particle detectors are all positioned roughly on the 2 kG surface. 22
2.7 Diagram of gridded particle detectors in polar imager. For all the experiments in this work, these detectors were biased to collect flux-tube integrated ion saturation current. 22
2.8 Installed Rake array. 31 tips, alternating floating potential and ion saturation probes, give measurements of potential and density fluctuations with enhanced azimuthal resolution. 23
2.9 Top, a spectrogram of floating potential fluctuations. Right, the ensemble average of the spectrogram displaying the stationary spectrum. Bottom, ion saturation current fluctuations, approximately proportional to density fluctuations. 24
2.10 Viewing the plasma with the Polar Imager. An m = 1 mode is observed to rotate in the electron magnetic drift direction. Notice the amplitude varies in time (all color bars the same), and the appearance of some higher order modes. 25
2.11 Fluctuations display power law trends indicative of the inverse energy cascade. . . 26

3.1 An example feedback system; a car's cruise control. 29

3.2 Block diagram of the plasma-feedback system. Notice the control is only applied to the fluctuations of the potential, as indicated by the low-pass and high-pass filters. . 29
3.3 The fundamental components for the feedback circuit. 30
3.4 Buffer element. Gain is set through choice of the gain and feedback resistors. . . . 31
3.5 Second-order Sallen-Key high-pass filter. 32
3.6 Amplitude and phase response of the high-pass filter. 33
3.7 Circuit diagram for first-order all-pass filter. 34
3.8 Phase response of first order all pass filter for various resistor settings. 35
3.9 Complete feedback circuit. The signal from the sensor is passed through a pre-amplifier, high-pass filtered, then phase shifted. This is then input to a four-quadrant amplifier and AC coupled to the electrode with a series 12 μF bipolar capacitor. The phase is varied by adjusting "R" in the all-pass filters, and gain is determined by the "R_F" resistor in the pre-amplifier. 36
3.10 Comparison of the measured and SPICE simulated phase response of the feedback circuit. Top, the circles show the measured phase response with applied feedback at the indicated phase setting (at 3 kHz) as determined from the cross phase between the sensor and electrode voltage measurements. The triangles show the spice calculated phase response at the same resistor settings. Bottom, the measured and calculated phase shifts at the tuning frequency of 3 kHz. There is an approximately constant shift of $\sim 5°$. 38
3.11 The possible sensor and electrode positions in the CTX vacuum chamber. The indicated mode rotation direction, determines a convention. Red is a "downstream" region of the plasma (relative to Electrode A), blue is an "upstream" region. 39

4.1 Experimental configuration for open-loop tests. An electrode is driven at 4 kHz, 80 V peak-to-peak. The azimuthally positioned floating probes are used to measure the attenuating influence in the direction of mode rotation. 42

4.2 Top, power spectra of three floating potential probes while driving a 4 kHz signal on the electrode. Bottom, the relative change in spectral power at the driven frequency as measured on all five floating probe. The amplitude decreases with separation and the oscillations appear to be carried only in the direction of mode rotation. 43
4.3 Current (red) and bias (blue) of the electrode when driving the 4 kHz signal. Note the limit of ion saturation current and the DC floating potential. 44
4.4 Top, IV trace from the 4 kHz driven signal. Bottom, analysis of the IV sweep indicates resistive sheath behavior with a resistance of 400 Ω near floating potential. 45
4.5 Experimental configuration for feedback. Notice here the sensor is a floating potential probe located 12° upstream from the electrode. 46
4.6 The sensor voltage (a), electrode voltage (b) and current (c) during feedback which is in phase with the measured fluctuations (red) and 180° out of phase (blue). The lower plots are of the IV characteristics during negative (d) and positive feedback (e). Note that the data shown in the IV plots are from a much longer time period than shown in the three above plots. 47
4.7 Triggering events as measured by the sensor. a) RMS, raw. b) Averaged over 18 triggering events. c) Zoom in of the trigger off time. 49
4.8 Spectra measured by the sensor without feedback (black), with positive feedback (red) and negative feedback (blue). Feedback results in significant changes to the turbulent spectrum. 50
4.9 Top, standard deviation with frequency plotted about the natural spectrum to display the variation in spectral content on a shot to shot basis. Bottom, percent variation in the spectrum. An average variation of 18% is assumed for all spectra in this document. 51
4.10 Phase scan using the 12° separation configuration. 52
4.11 Frequency integrated intensity (a) and frequency integrated, frequency weighted intensity (b) with applied phase. 54

4.12 Coherence and cross phase between sensor voltage and electrode voltage (blue), and sensor voltage and electrode current (green) with increasing gain. As the gain is increased too high with amplifying feedback, the power supply limits begin to have an effect. 55
4.13 Top, measured spectrum as gain is increased from -4 to 4. Bottom, the frequency integrated intensity. Positive gain amplifies the spectrum while negative gain suppresses it. 56
4.14 Illustration of the circuit model used to describe power flow. The electrode is biased by the fluctuations in floating potential (measured by the sensor) multiplied by a complex gain. A current is driven across the resistive sheath (not to scale) in proportion to the voltage difference $V_E - V_P$. 57
4.15 An example of the instantaneous power of the electrode, into the plasma and into the sheath. 59
4.16 Time averaged power for positive feedback (Gain = 4) and negative feedback (Gain = -4). The total power and power into the sheath are positive for both cases. The reversal of the sign of power into the plasma indicates the plasma acting as a load during positive feedback and a generator during negative feedback. 60
4.17 A cartoon of the simplified circuit diagram representing the coupled plasma-feedback system during positive and negative feedback. The plasma is represented as a voltage source which can act as a load or a generator, depending on the phase of the feedback. 61
4.18 Intensity (a) and conductance (b) with frequency, and the band integration of the two (c) indicate that positive conductance leads to amplification of the fluctuations, while negative results in suppression. 63

4.19 Experimental configuration for measuring influence of feedback with azimuth. Notice here the sensor is a floating potential probe located 12° downstream from the electrode. The other diagnostics discussed in the analysis are also displayed including the azimuthally separated floating potential probes and polar imager detectors. 64

4.20 Response to triggered feedback measured by floating potential probes at various azimuthal separations from the electrode. The influence of feedback is strongest closer to the electrode in the downstream direction and attenuates with increased separation. 65

4.21 The normalized RMS levels from the polar imager detectors (circles) and the floating probes (triangles) for positive (red) and negative (blue) feedback. Each measurement is normalized to its multishot averaged RMS level without feedback. We observe a 30% reduction in RMS levels with suppressing feedback, and a 30% increase with amplifying feedback. This only occurs downstream in the direction of mode rotation, sharply defined after the electrode. 66

4.22 The peak coherence between the sensor and various polar imager detectors for amplifying (red), suppressing (blue) feedback, and without feedback (black). Again, the influence of the feedback on coherence is downstream from the electrode. . . . 67

4.23 The spectrum as measured by the various polar imaging detectors on the L = 5 radius. Black is without feedback, red is amplifying and blue is suppressing feedback. The plots are positioned according to the detector azimuth in the plasma. The influence is observed to attenuate with increased separation. 68

4.24 (a-c) show various sensor-electrode configurations with the direction of mode rotation and azimuthal separation indicated. (d-f) show a comparison of phase scans performed with the various configurations. The trend shifts with the azimuthal separation as long as the separation is small enough that the effects of feedback are not attenuated significantly. 70

4.25 a) Two independent feedback systems driven by one sensor apply oppositely phased feedback, pulling nearly opposite currents. b) One system is driven by the sensor and two electrodes are coupled to the outputs of the amplifier. The current through the electrodes is equal and opposite, and the circuit completes through the electrodes. 71
4.26 Phase scans performed using the two configurations of Figure 4.25. The similar response suggests that whether the circuit completes through the chamber wall or through another electrode does not effect the plasma response to feedback. 72
4.27 Phase scans performed with high-pass filtered feedback. Dashed lines indicate the corner frequencies of the high-pass filters. Excitation of higher frequencies does not appear to drive the inverse energy cascade. 74

5.1 The profile function h and its derivative. Notice the change in sign of the derivative term at $y = 1$. 91
5.2 Density and temperature profiles used for the calculations. 92
5.3 Structure of matrices and vectors in terms of the potential, density and pressure components. The matrix representation on the left displays the organization of the coupling. 93
5.4 Structure of the $\mathcal{M}$ matrix. The potential involves off-diagonal terms due to the radial derivatives. 94
5.5 Structure of the $\mathcal{N}$ matrix. The coupling of the potential, density and pressure from the three equations can be observed from the non-zero elements (black). 94
5.6 The 100 eigenvalues from the solve. The real part (rotation rate) is on the x-axis, and the imaginary part (growth rate) is on the y-axis. The dominant mode is taken to be the mode with the largest growth rate, here roughly 3.5×10^4 s^{-1} 95
5.7 The real and imaginary parts of the potential, density, and pressure components of the dominant mode. 96
5.8 The two dimensional structure of the dominant eigenmode in potential, density and pressure. 96

5.9 The radial locations of the sensor and electrode elements superimposed on the dominant potential eigenmode. 97
5.10 Phase scan performed with current injection term included in model. Left, Equation 5.34 with applied phase. Right, Equation 5.35 with applied phase. 100
5.11 Gain scan performed with current injection. Left, Equation 5.34 with gain. Right, Equation 5.35 with gain. 100
5.12 Comparison of the experimental phase scan results (blue) to the current injection scans of the eigensystem (red). Top is the relative change in intensity/mode amplitude, and on bottom is the relative change in dominant mode frequency. . . . 101
5.13 Comparison of the experimental gain scan results (blue) to the current injection scans of the eigensystem (red). Top is the relative change in intensity/mode amplitude, and on bottom is the relative change in dominant mode frequency. 102

A.1 Left: The equatorial magnetic field strength (green), the magnetic flux (blue). Right: The differential flux tube volume increase like r^4. 113
A.2 Electron and ion gyro frequencies (dashed) and Larmor radii (solid) with radius. The electron gyro frequency is resonant with the microwaves near to 27 cm. 114
A.3 Approximated bounce frequency for electrons (left) and ions (right). 115

D.1 Polar Imager detectors with mapping to digitizer locations. 132

E.1 Installation of Rake array (left top and bottom). 31 tips, alternating measurements of floating potential and density, give 15 measurements of radial transport (right, top and bottom). 134
E.2 Top, the complete circuit for the Rake array. The grey ribbon cable connects to the Rake array, the colored twisted pair ribbon cable connect to the digitizer. Bottom, the circuit diagram for the floating potential probes (left) and the ion saturation probes (right). The 1 mF cap and 100 kΩ resistor in the ion saturation circuit allow the use of one power supply for all probes. 135

E.3 PCB for the entire Rake array. Red is the top layer copper, green is the lower layer, black is the silk screen. 136
E.4 Connector for the array to the PCB enclosure (female side). Tip 1 connects to “B”, and the tips follow sequentially to Tip 31 on “j”. “A” is not connected. 137

F.1 High-pass filter and frequency response. 139
F.2 A first order high-pass filter. 142
F.3 Sallen-Key and MFB second-order high-pass filter topologies. 143

G.1 Triggering circuit for feedback experiments. 144
G.2 Isolation transformer for “zero-net-current” experiments. 145

List of Tables

2.1 Plasma and turbulence parameters at L = 45 cm 27

Acknowledgements

This thesis would not have been possible without the guidance and mentoring from the many people I interacted with at Columbia. First and most influential is my advisor Michael Mauel. In addition to being a wizard of all things science and engineering, he has his students best interests at heart, and his guidance has made me the confident and well-rounded researcher I am today. I'd also like to thank Jay Kesner and Darren Garnier at MIT for valuable conversations and advice over the years.

I also received vital support from my fellow graduate students. Abed Balbaky spent way too much time tutoring me on the basics of circuit design, and Qian Peng was the only person to explain generalized coordinates in an understandable manner. Jeff Levesque and Nick Rivera were not only great sources of knowledge, but also my daily sources of conversation. Matt Worstell was a full time "CTX instructor", sensi, and friend who is solely responsible for my working knowledge of running our machine. Matt Davis, Daisuke Shiraki and Aaron Senter are also some of the best people I met in New York and I'm better for knowing them. I'd also like to thank my girlfriend Kat Kennedy for patiently listening to me ramble about science and tolerating my unpredictable future.

Finally, and most importantly, I'd like to thank my family. My parents, brother and sister have been moral support throughout my entire academic life (and before) and I am forever grateful. In particular, I'd like to dedicate this thesis to my Mom. Not only were you my first science teacher, but your continual love and encouragement are the only reasons I'm a physicist and not an inmate.

Chapter 1

Introduction

This thesis investigates the application of feedback to interchange-turbulent dipole-confined plasma via inserted probes and electrodes. This work was performed at Columbia University on the Collisionless Terrella Experiment (CTX). This chapter introduces some of the key concepts and important physics of these plasmas, which apply both in Space and in the laboratory. Related work in feedback of a similar nature is also briefly discussed, followed by a description of the organization of this document.

1.1 Dipole-Confined Plasmas

Plasmas confined by dipolar magnetic fields occur commonly in two places in our solar system; planetary magnetospheres and laboratory experiments. These magnetic fields, having neither magnetic shear nor helicity, often exhibit low-frequency plasma dynamics dominated by interchange instabilities. Collective plasma motion is perpendicular to the magnetic field lines and is driven by gradients in plasma density and pressure.

1.1.1 Planetary Magnetospheres

Long before Spitzer's stellarator [1] or the ZETA Z-pinch experiments [2], plasmas were being confined by the nearly dipolar magnetic fields of many of the planets in our solar system. The Earth's magnetic field is produced by a dynamo action of interior liquid metal where convection drives electric currents. These currents in turn produce closed magnetic field lines which can extend out for 10 Earth radii. This field, which can be represented by a dipole to first order, is then distorted by pressure from the solar wind (Figure 1.1, left). Planets further from the Sun, such as Jupiter and Saturn (Figure 1.1, right), experience reduced solar wind pressure and therefore are better represented by the dipole magnetic geometry at larger radii.

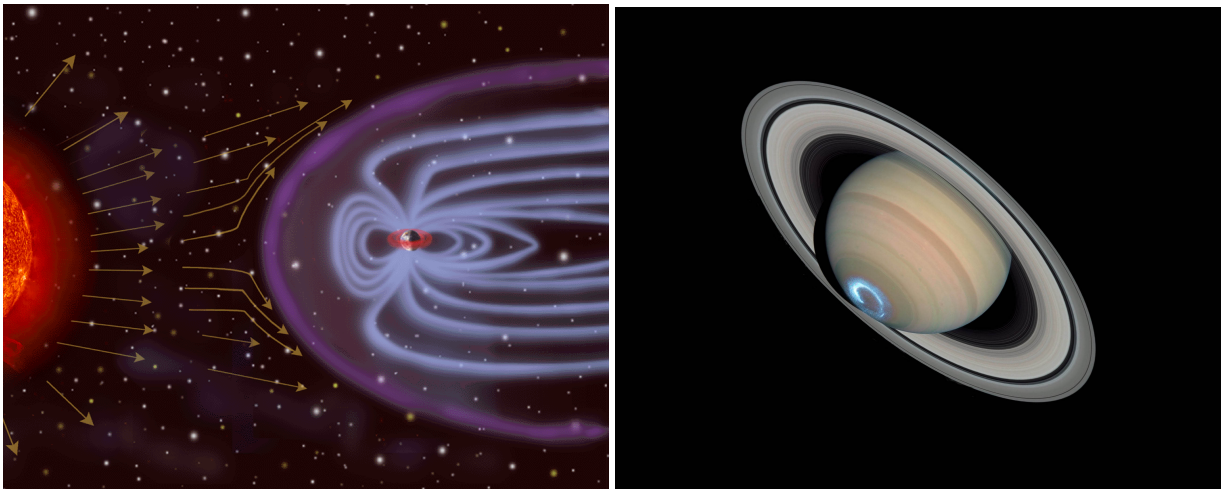

Figure 1.1: Left, pressure from the solar wind distorted the Earth's magnetosphere. Right, aurora on Saturn's southern pole indicating the presence of a magnetosphere.

Plasma from the solar wind (dominantly protons and electrons with some helium ions) is incident on the sun facing side of the planet. The plasma trapped in the magnetosphere is partly from the solar wind, but also from gas ionized in the ionosphere, such as oxygen. This plasma is non-uniformly distributed in two (or sometimes three) "radiation belts", located between 2-6 Earth radii, as well as in the plasmasphere at lower altitude. It is this plasma that exhibits interchange dynamics and convection similar to those observed in the laboratory.

In addition to the magnetosphere, planets also have ionospheres at significantly lower altitudes. Ionospheres are the upper boundary of the planet's atmosphere where a significant portion of the

particles are ionized. This effectively creates a surface on the planet with a significantly higher perpendicular conductivity than that of the magnetosphere. This conducting surface is connected to the magnetosphere by the field lines which terminate on the surface of the planet, mostly at the poles. As such, field aligned currents end up coupling magnetospheric dynamics to the ionosphere [3]. A picture of these currents is shown on the left of Figure 1.2[1]. Here, magnetospheric plasma convection twists a flux tube, driving currents along the field line to the footprints in the ionosphere. The conductive ionosphere can then carry these currents to the footprint of another field line, effectively shorting them (right of Figure 1.2).

If the ionosphere is a good conductor, these currents can be maintained, which in turn maintains the twist of the magnetic flux tube and the convection of the magnetospheric plasma. Alternatively, if the ionosphere acts resistively, the ionospheric current is dissipated, reducing the field line helicity and damping the plasma convection (i.e. fluctuations) in the magnetosphere [2]. It is these currents which cause the phenomenon known as aurora as precipitating electrons collide and ionize neutral particles in upper atmosphere, creating amazing light shows in the sky around 10-20° latitude from the geomagnetic poles.

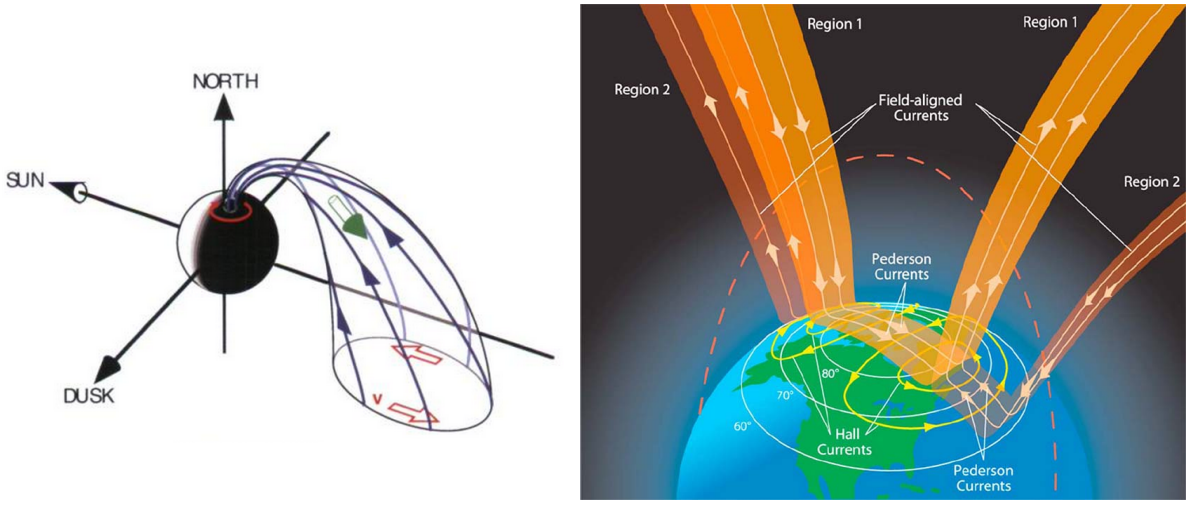

Figure 1.2: Left, convection in the magnetosphere is transferred to and damped in the ionosphere. Right, field aligned currents connecting the magnetosphere to the ionosphere.

[1] Figure credit to Paschmann [3].

[2] Interestingly, neutral winds driving plasma convection in the ionosphere can reverse this process, driving plasma convection in the magnetosphere [3]. The ionosphere can put energy into the magnetosphere!

Given these currents and assuming quasi-neutrality, the field-line integral of the divergence of the perpendicular magnetic drift current must be balanced by field-aligned currents to the polar ionosphere [4, 5, 6]. This statement is fundamental to describing the dynamics of plasma confined in a planetary magnetosphere, but is not always true in laboratory magnetospheres. We will see that the feedback described in the following chapters is in many ways analogous to this ionospheric damping of magnetospheric plasma convection!

1.1.2 Laboratory Magnetospheres

The laboratory studies of dipole-confined plasma are among the first controlled plasma physics experiments. Birkeland's studies of the aurora [7] motivated the construction of the first "terrella" experiment (Figure 1.3 a.), where a dipole magnet surrounded by a conductor was bombarded with electrons. Almost exactly 100 years later, similar experiments were performed by Shaikhislamov et al. [8], where ionospheric-like currents were observed in the laboratory with pulsed plasmas discharges incident on a small dipole magnet surrounded by a segmented conducting shell (Figure 1.3 b.[3]). In both of these experiments, currents from the confined plasma can travel along the field lines, pass through the conductor ("ionosphere") and return to the plasma through a field line elsewhere.

Another study of laboratory magnetospheres has taken place for the last 20 years. The CTX/LDX group has studied the dynamics of dipole-confined plasmas produced by steady microwave heating. CTX, which like the above experiments has a mechanically supported magnet (Figure 1.3 c.), has focused on the study of radial diffusion, interchange modes, and interchange turbulence [9, 10, 11, 12, 13, 14]. LDX, which uses a levitated current ring (Figure 1.3 d.) to produce the magnetic field, focuses on peaked density and pressure profiles shaped by plasma compressibility [15, 16]. In both of these experiments, the parallel dynamics have been measured to be approximately zero ($k_{\|} \approx 0$) and there are no field aligned currents. In LDX these current are prevented by short field lines which close on themselves, while in CTX the termination points of the field lines are insulating.

[3] Figure credit to Shaikhislamov et al. [8]

In these last two experiments, the field-line integral of the divergence of the perpendicular magnetic drift current must be equal to zero [17]. Here, the electron diamagnetic current is balanced by the ion polarization current. We will later see that by introducing a source of current with a biasing electrode, we can simulate the effects of the field aligned currents in these systems. In this manner, we impose an effective "ionospheric regulation" of fluctuations in laboratory confined plasma.

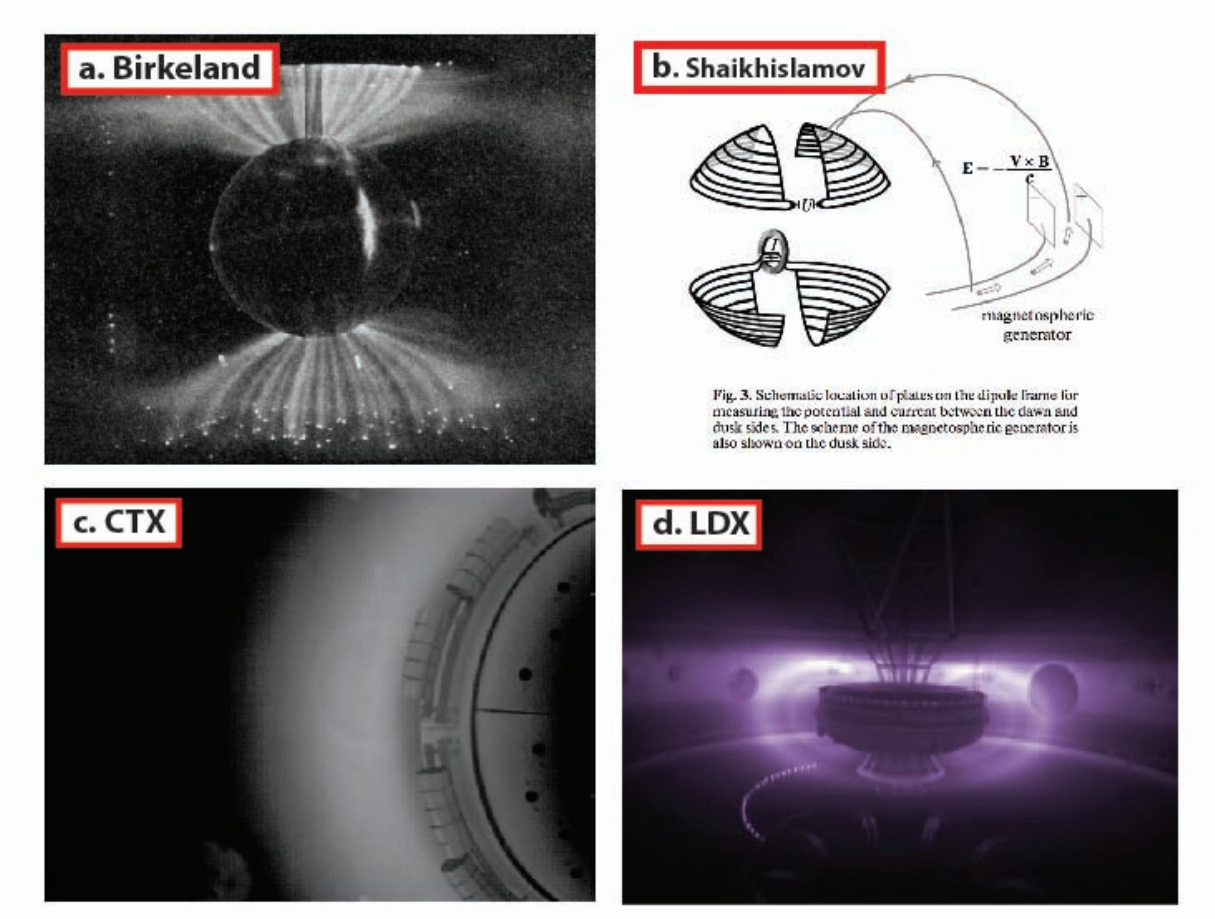

Figure 1.3: a) Birkeland's terrella experiment. b) Shaikhislamov's ionospheric current experiment. c) An image of a plasma in CTX. d) A plasma confined in a levitated dipole field (LDX).

1.2 Basis Physics of Dipole Confined Plasmas

There are many ways to describe the motions of plasma confined by a magnetic field. In this section we discuss the two extremes; the path of an individual particle as it moves in a magnetic dipole geometry, and the motions of a continuum of these particles behaving as a fluid. Each picture has insights that help us gain more intuition for the complicated dynamics of these systems.

1.2.1 Charged Particle Motion

The three fundamental motions exhibited by a charged particle in a magnetic field are depicted in Figure 1.4. Assuming a dipole field, there will be gyration about the field line (green), bouncing along the field (blue), and a drift in the symmetric direction of the field. Associated with each of these motions is an adiabatic invariant [18]. For a large enough separation in the time scales of these motions ($\omega_c >> \omega_b >> \omega_d$), these quantities will be effectively conserved. We'll go through these particle motions for completeness.

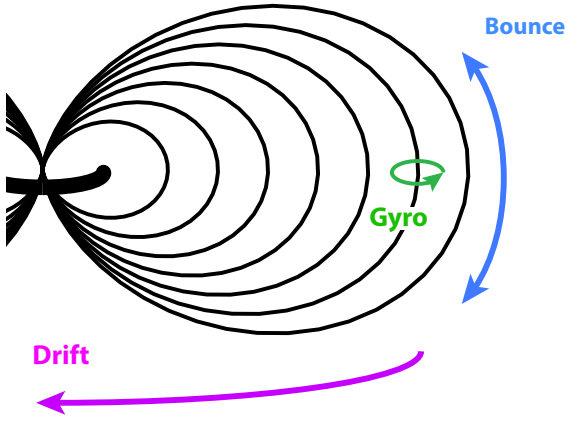

Figure 1.4: The three particle motions in a dipole magnetic field; gyration, bounce and drift. Related to each is an adiabatic invariant; μ for gyro motion, J for bounce motion, and ψ for drift motion.

Every student of physics knows that a charged particle in a magnetic fields is subject to the Lorentz force, guiding any motion perpendicular to the field into circular orbits about the field lines. The particle will orbit at the cyclotron frequency, given as:

$$\omega_{ce,ci} = \frac{eB}{m_{e,i}} \tag{1.1}$$

This gyrating charged particle is a tiny current loop, and therefore has a magnetic moment $\mu = W_\perp/B$. It can be simply shown with $\nabla \cdot B$ and conservation of energy that this quantity μ must be conserved if the particle moves along the field line. A force, referred to as the mirror force, parallel to the field line will oppose the motion of the particle toward a region of increasing field strength. In a dipole this results in another periodic motion as the particle bounces back and forth along a field line between regions of high field strength. This bounce motion occurs with period $2\pi/\omega_b$, while the particle is also spiraling at ω_c. Note that this gyro frequency increases in the regions of increasing B, and this diamagnetic response can also be used to describe the invariance of μ. The invariant for the parallel bounce motion is given as:

$$J = \int_a^b v_\parallel ds \qquad \text{Invariant of bounce motion} \tag{1.2}$$

where a and b are the bounce points of the particle.

Finally, considering the effects of perpendicular gradients in the field strength, we see the particle will experience a nonuniform gyro orbit. This manifests itself as a "drifting" of the center of gyration and the particle will now begin to orbit the entire system in the periodic direction of symmetry. This last motion is once again periodic. The related invariant effectively comes from conservation of flux as the particle drifts around the dipole. As such, the invariant is simply the magnetic flux, ψ in a drift orbit. This motion is generally much slower than the other two, and due to collisionality is often not conserved very well.

Comparisons of these time scales specific to the CTX device are given in the following chapter, and a more complete explanation of the calculation of these parameters is given in Appendix A.

1.2.2 Fluid Description and the Interchange Instability

Often a fluid description can be the simplest and a surprisingly accurate way to describe a plasma, even in the case of low collisionality! Fluid descriptions can either treat the ions and electrons as separate, mixed fluids obeying different rules, or as a single fluid, ions and electrons effectively bound together. For simplicity, we will discuss the ideal MHD (magnetohydrodynamic) [19] case, where the plasma is "frozen" to the magnetic field lines. In a dipole, we discuss volumes of the plasma as tubes of magnetic flux. Motion of the plasma can be viewed as the exchange of the positions of two flux tubes. Given that the field of a dipole goes like $1/R^3$ [20], the volume of a flux tube goes like R^4 (as is shown in Appendix B). With motion in the radial direction, significant changes to the flux-tube volumes can occur, adiabatically heating the inward moving flux tube, and cooling the outward moving one. This motion can be described as a mechanism for minimizing the potential energy of the system. This swapping of flux-tubes is referred to as an interchange, or flute, instability. By definition the magnetic topology does not change and $k_{\|} = 0$. Following Rosenbluth and Longmire [21], we see that a plasma is interchange unstable when

$$\Delta E = \delta p \delta V + \gamma p \frac{(\delta V)^2}{V} = V^{-\gamma} \delta(pV^{\gamma}) \delta V < 0 \tag{1.3}$$

This equation is the basis for designing plasma confinement devices with "good" curvature ($\delta V < 0$), but dipoles are characterized by "bad" curvature. In order to be interchange stable in a dipole, the other differential term in Equation 1.3 must be larger than zero. Given the volume of a flux tube, we see this condition can only be satisfied for a sufficiently gentle pressure profile,

$$V \sim R^4, \delta(pV^{\gamma}) \sim \delta(pR^{4\gamma}) \tag{1.4}$$

So for $p \sim R^{-4\gamma}$, the condition for marginal stability is met ($\Delta E = 0$). A similar argument can be applied to the density profile in a dipole field [22]. This concept has been studied for both the pressure [16] and density [15] profiles in a levitated dipole.

Interchange motions are not unique to dipole-confined plasma and can occur in a variety of

natural and laboratory settings. These include convective ionospheric storms [23], outward flows from rotating magnetospheres [24, 25], space weather [4, 5, 6], plumes and fingers at the edge of the plasmasphere [26], and filamentary structures, called "blobs", at the edge of magnetic confinement devices [27, 28]. The fundamental importance of interchange instability in magnetized plasma has motivated several laboratory investigations of the structure, growth, and saturation of interchange instabilities driven by energetic particles [9, 29], pressure gradients [30, 10, 13, 14, 31], and plasma rotation [32, 33].

1.2.3 Interchange Turbulence in Dipole Plasmas

Under certain conditions, the interchange motions in dipole confined plasmas result in fully developed turbulent dynamics. Because interchange motion is everywhere perpendicular to the magnetic field, interchange turbulence is essentially two-dimensional in these devices. When the field-aligned currents are relatively weak, as is the usual case in laboratory experiments[13], during night-time ionospheric storms [34], and when the dipole is magnetically levitated, interchange instabilities develop into a state of 2D turbulence with a power-law fluctuation spectrum. Cross-field plasma transport results from chaotic, low-frequency convective vortices that are field-aligned and generate intermittent filaments [14, 15, 35]. A more detailed description of the turbulence specific to CTX is given in the next chapter.

The majority of laboratory plasma turbulence studies have focused on drift-wave turbulence which is believed to significantly enhance cross-field transport in many magnetic confinement devices [36]. That being said, flute-like modes can develop at the edge of these devices which are normally interchange stable, and turbulence there will drive enhanced outward transport [27, 28]. We can study interchange turbulence easily in dipole confinement devices as these plasmas can be globally interchange turbulent (as opposed to only at the edge) and the large plasma volume allows for simple diagnostic access. These studies could give insight to the edge turbulence found in other machines.

1.3 Feedback in Plasmas

The application of feedback to unstable plasmas is by no means a new concept [37, 38]. Examples of the various forms of feedback include the stabilization of drift-waves via directly applied currents [39] to the control of MHD kink modes with magnetic coils [40, 41]. Here we will focus on two applications of feedback that contain elements related to the experiments described in this thesis. Both involve the insertion of probes into the plasma and applying bias/currents to suppress instabilities.

1.3.1 Feedback on Interchange Unstable Plasmas

In 1971, Prater was able to suppress large growth rate flute modes in a multipole-like magnetic geometry driven unstable by bad curvature and a steep pressure profile [42]. The experiment, shown in Figure 1.5 [4], used a sensor to measure plasma density fluctuations which were then phase shifted and amplified and passed to capacitively coupled global biasing electrodes. By tuning a plasma collimator it was possible to destabilize a dominant $m = 1$ mode drifting in the ∇B direction at 18 kHz.

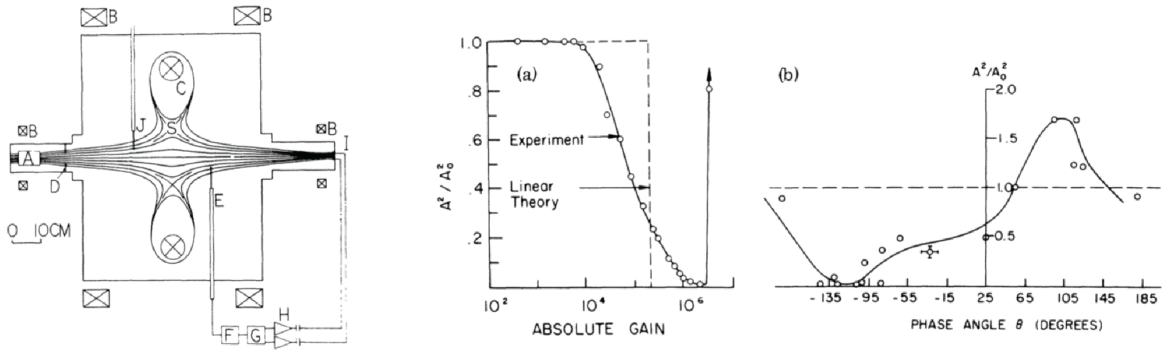

Figure 1.5: Left, experimental configuration for Prater's flute-mode suppression work. Middle and right, normalized mode amplitude with gain and phase (respectively), showing strong suppression of the single mode.

By performing scans of applied phase and gain (Figure 1.5, right), the optimal parameters were established where significant suppression of this flute mode was achieved. This work is one

[4] Image credit to Prater [42]

of the few cases of feedback being applied to interchange unstable plasmas. Note though that the experiment was configured specifically to produce a discrete number of modes and avoid the broadband interchange turbulence we are discussing in this thesis.

1.3.2 Feedback on Turbulent Plasmas

More recently, researchers on the TEXT experiment studied the application of feedback with a biasing electrode to drift-wave turbulence at the tokamak edge [43, 44, 45]. Here, field-aligned fluctuations were measured and a bias was applied to the same field line in a similar manner to that of Prater. The experimental configuration is shown in Figure 1.6 a, b[5], with a sensor for the feedback both near the biasing electrode and far (further along the field line). By applying broadband feedback to these fluctuations, it was observed that the plasma local to the driver could be significantly amplified or suppressed (Figure 1.6 c.). Further from the driver on the same surface (field line), there was a reduced effect of the feedback on the turbulent spectrum (d.).

The application of feedback to turbulent plasma is similar to the experiments described in this thesis, though the nature of the turbulence is very different from the turbulence in CTX. In TEXT, the turbulence was due to drift-waves and was localized to the edge of the machine. Additionally, the response to the feedback is measured only on the same field line, where as we will see in CTX, the feedback influence is a cross-field effect.

[5]Image credit to Richards and Uckan [44, 45]

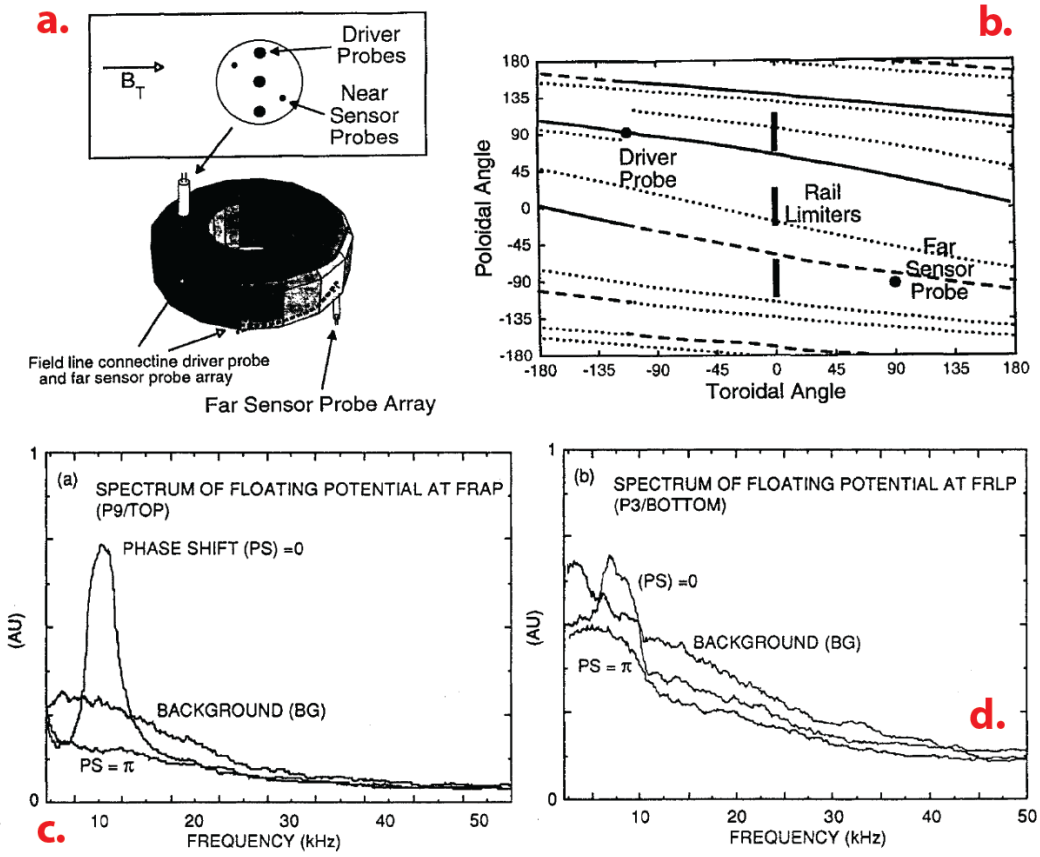

Figure 1.6: a) Experimental configuration on the TEXT tokamak. b) The positioning of driver and sensors on magnetic surface. c) The local response to feedback shows amplification and suppression, while the influence is reduced further away (d).

1.4 Organization

The organization of this thesis is as follows; Chapter 2 overviews the Collisionless Terrella Experiment, CTX, and the nature of the confined plasma. In particular, the magnetic field, vacuum chamber, plasma source and diagnostics are described in detail. Some of the more important plasma parameters are discussed and tabulated for reference. In Chapter 3 the feedback system is described. This includes discussion of the input measurement, circuit design and feedback output to the plasma. Chapter 4 covers the various experiments performed in characterizing the feedback system and the response of the plasma to feedback. These include observations of fluctuations as feedback is triggered on and off in time, as well as the spectral influence as the gain and phasing of feedback system are varied. Additionally, the effects of turbulent decorrelation on the feedback influence are explored. Chapter 5 discusses a gyro-fluid model of dipole-confined plasmas. The nonlinear equations are linearized to yield as eigensystem of potential, density and pressure. The numerical calculations are explained and the solutions compared to the experimentally measured values. Chapter 6 then concludes and provides several suggestions for experiments the author feels would provide answers to questions that are still unresolved.

The main chapters of this thesis have been purposefully written as a concise overview of the experiments and calculations performed in gaining an understanding of the effects of current-injection feedback on interchange turbulent dipole-confined plasmas. Minimal background is discussed in these chapters to deliver the subject matter efficiently to the knowledgeable reader. Having not forgotten the work involved in achieving an understanding of the disperse and sometimes difficult concepts required to conduct this research, an extensive appendix of various key topics has been included. Reference to these are made throughout the text where further background might be desirable. This is also an effort to compile a resource for future students of dipole-confined plasma physics, as some subjects are less well documented than one might expect.

Chapter 2

The Collisionless Terrella Experiment

The experiments conducted in this thesis were performed on a device known as CTX, the Collisionless Terrella Experiment, shown in Figure 2.1. CTX creates laboratory scale dipole-confined plasmas in a vacuum chamber roughly 1.5 m in diameter and length. These plasmas are unstable to the interchange instability described in the previous chapter, and under certain conditions exhibit dynamics indicative of fully developed two-dimensional turbulence. The plasma parameters are measured by dozens of diagnostics at various locations, allowing for resolved spatial and temporal analysis of the fluctuations. This chapter discusses the design and parameters of the CTX device, the diagnostics used, and the conditions and nature of the plasma. A description of the configurations, "turn-on" procedures, and tips for using the equipment involved in running CTX is included in Appendix C for the aid of future students.

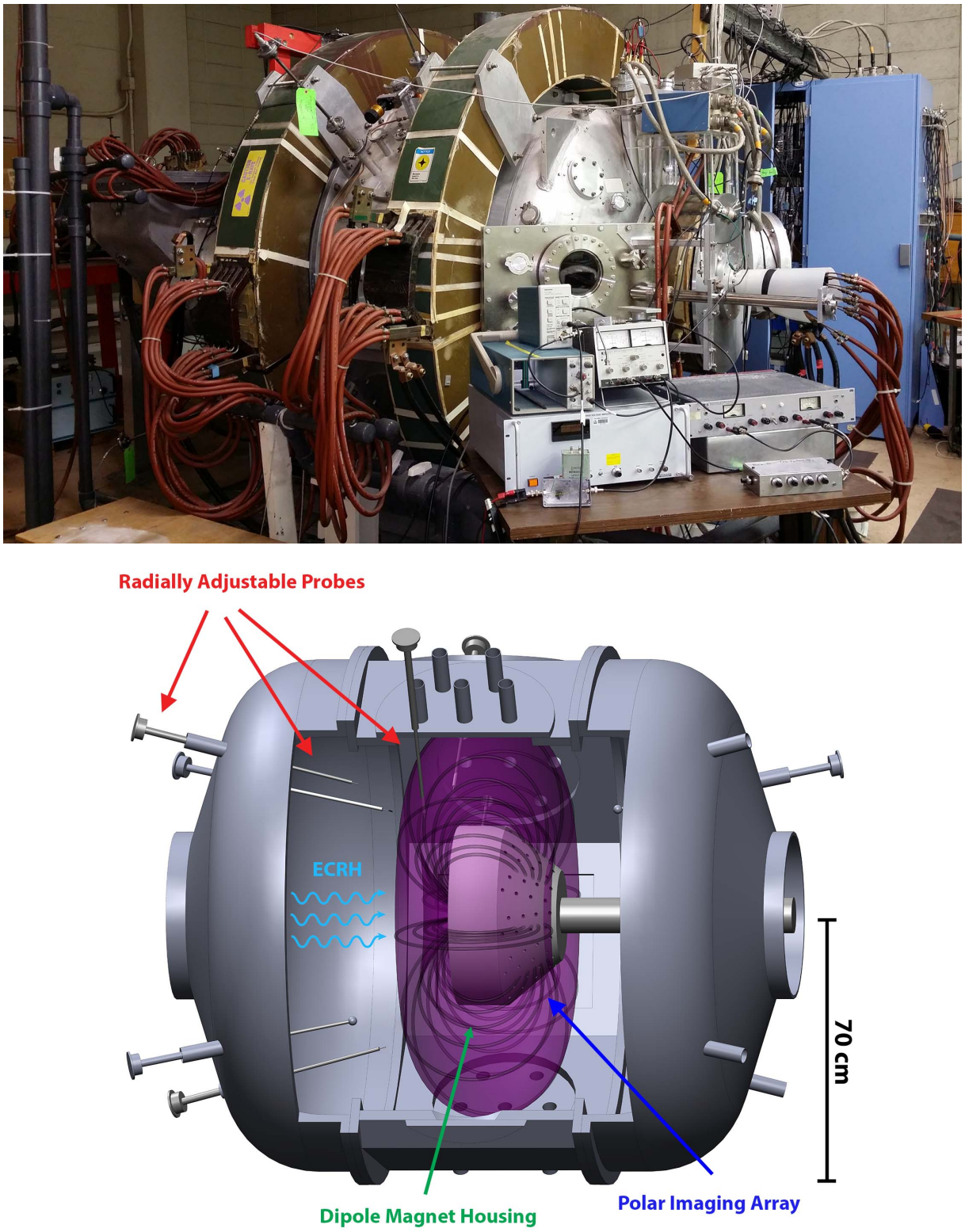

Figure 2.1: Top: Photo of the CTX device. Bottom: Rendering of the CTX vacuum chamber, cut away to expose the magnet and probes inside.

2.1 Magnetic Field

The dipolar magnetic field of CTX is produced by a mechanically supported current-winding, housed in an insulating, alumina-coated casing. The current winding is composed of six coils in 12x14 pancakes, wound such that the connections are on the inside and in series, as shown in Figure 2.2. The wire is hollow for water cooling, which is performed in parallel.

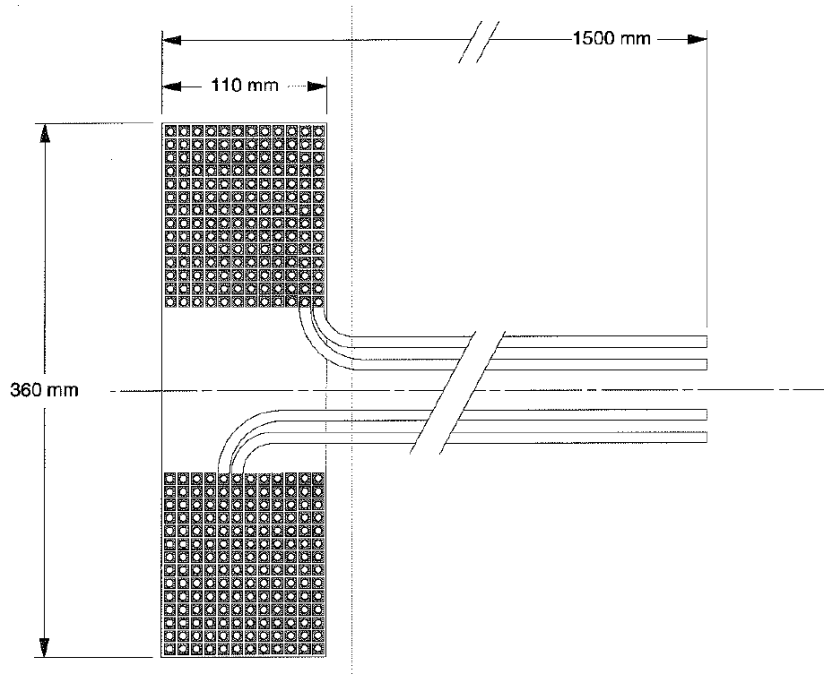

Figure 2.2: Cross-section of dipole magnet current-winding. Six coils are wound into 12x14 pancakes such that the cabling can be all internal.

The field is modeled as a point dipole, as was shown in [46] to be a good approximation. At the inner face of the magnet (21 cm) the field strength is near 1500 Gauss, and falls to around 50 Gauss at the chamber wall (68 cm). The magnetic dipole moment of CTX is 0.00172 Tm^3, and from this we can write the field at the midplane as:

$$|B| = \frac{0.00172}{R^3} \tag{2.1}$$

where R is the equatorial radius. As the dynamics of the plasma are highly dependent on the magnetic field strength it is convenient to use the dipole field as a coordinate system. From electromagnetic theory, the field of a point dipole in spherical coordinates has the form:

$$\vec{B} = \frac{2M}{r^3}\cos\theta\hat{r} + \frac{M}{r^3}\sin\theta\hat{\theta}, \qquad |\vec{B}| = \frac{M}{r^3}\sqrt{1+3\cos^2\theta} \tag{2.2}$$

We can visualize the geometry of a dipole from the equation for a field line. By definition a field line points in the direction of the field at all points in space, so the ratio of the field components yields the equation of the field line. In spherical coordinates:

$$\frac{dr}{rd\theta} = \frac{B_r}{B_\theta} = \frac{2M/r^3\cos\theta}{M/r^3\sin\theta} = \frac{2\cos\theta}{\sin\theta} \tag{2.3}$$

Rearranging and integrating,

$$\int\frac{dr}{r} = \int\frac{2\cos\theta d\theta}{\sin\theta} \rightarrow \ln r = \ln\sin^2\theta + C \rightarrow r = R\sin^2\theta \tag{2.4}$$

where again $R = r(\theta = 0)$. The field lines at various R are plotted in black in Figure 2.3.

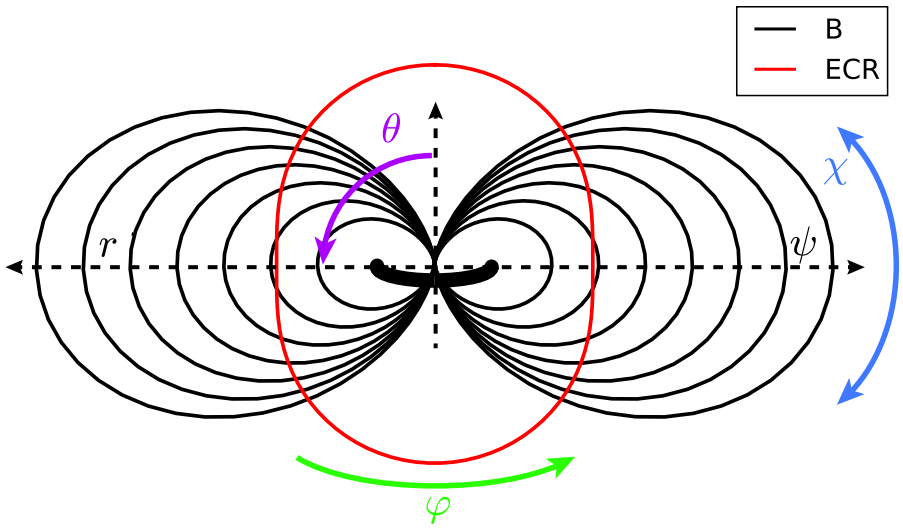

Figure 2.3: The spherical and flux coordinates in the dipole geometry. The electron cyclotron resonance layer is also highlighted.

From the above equations, we see that the dipole field strength is symmetric in the azimuthal direction, but varies in the polar and radial directions. Therefore, as a particle moves along a field line both its radial location and polar angle change. Coordinates in which the periodic bounce motion of a particle only changed one variable would simplify this issue. As explained in Appendix

B, we can move to a coordinate system of magnetic flux ψ, magnetic scalar potential χ and azimuthal angle φ. Here, magnetic flux acts as a radial coordinate, and the magnetic scalar potential is related to the position along a field line and the magnetic field takes the form:

$$\vec{B} = \nabla\varphi \times \nabla\psi = \nabla\chi \tag{2.5}$$

Using this coordinate system (labeled in Figure 2.3), the position of probe locations in the plasma can be mapped to specific field lines, as is well described in [46], and the theory of plasma dynamics in dipole fields is greatly simplified. Additionally, it is often convenient to describe volume in this coordinate system in terms of magnetic flux-tubes,

$$\delta V(\psi) \equiv \int_{-\infty}^{+\infty} \frac{d\chi}{B^2} \tag{2.6}$$

where the flux-tube δV is a differential volume per unit magnetic flux. Integration along the field line results in a dramatic simplification in the description of low frequency plasma dynamics, allowing investigation of the interchange motions of interest. A detailed description of these integrals is given in Appendix B.

2.2 Electron Cyclotron Resonance Heating

The plasmas confined in CTX are created through the application of plane-polarized microwaves at 2.45 GHz to injected neutral hydrogen. A 1.6 kW magnetron is connected to the main vacuum chamber through the wave guide system shown in Figure 2.4, in which both the input and reflected microwave powers are measured. The microwaves are reflected by the chamber walls, passing through the plasma many times before being absorbed.

The energy from the microwaves is absorbed by electrons with cyclotron frequency equal to the input microwave frequency, increasing their perpendicular velocity. This resonance occurs where the magnetic field strength satisfies $qB/2\pi m$ = 2.45 GHz, or 875 Gauss, as shown in Figure 2.3 in

red. When this resonance coincides with the midplane, it effects all the trapped electrons on that field line. In CTX this occurs at a radius of 27 cm where hot, deeply trapped electrons form a radial peak in plasma density and temperature. These electrons are responsible for an energetic particle instability known as the Hot Electron Interchange instability, which was the study of early work on CTX [9, 10, 12] and is observed on all dipole-confined devices [47, 48]. The parameters at this location in the plasma will be used as values for the normalization performed in Chapter 5.

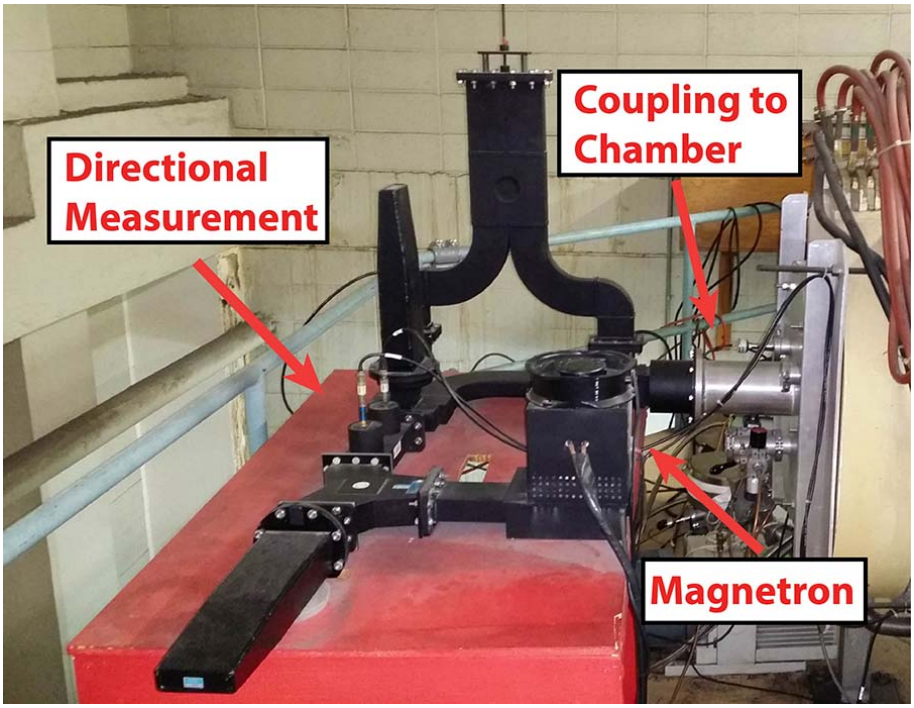

Figure 2.4: The waveguide connecting the magnetron to the vacuum chamber. Directional microwave antennas measure input and reflected microwave power.

From the dispersion relation for an electromagnetic wave propagating in an unmagnetized plasma [49], one can solve for the condition where the wave number becomes imaginary, and hence the microwaves are reflected by the plasma. This occurs when the plasma density reaches a critical threshold, determined by the plasma frequency, yielding a cutoff density for the 2.45 GHz wave:

$$\omega_{pe} = \sqrt{\frac{e^2 n}{\epsilon_0 m_e}} \approx 18\pi\sqrt{n}, \qquad n_c \approx 7.7 \times 10^{16}\mathrm{m}^{-3} \tag{2.7}$$

This sets roughly the upper limit on the densities CTX plasmas can attain.

2.3 Diagnostics

CTX plasmas are observed with a multitude of diagnostics which allow for measurement of dynamics at various azimuthal and radial locations. These include indirect measurements such as photodiodes, a fast camera and x-ray detectors, and direct measurements of plasma parameters via inserted Langmuir probes and gridded energy analyzers. In this section we focus on the latter of these diagnostics as they were primarily used for the work in this thesis. For a review of the other diagnostics, refer to [50]. All of the diagnostics in this section are recorded at 250 kHz on Jorway A14 transient recorders.

2.3.1 Floating Potential Probes

During these experiments, CTX was equipped with 5 radially adjustable floating potential probes located at 5 different azimuthal locations. Three were built or rebuilt during the course of this work, and all were removed and tested to confirm they had similar impedance and dimensions. These probes consist of a stainless steel wire tip with a 100 kΩ resistor immediately after the tip. This resistor and coaxial connections are housed inside a 12” long alumina shaft, which then connects to a stainless steel shaft which exits the vacuum chamber via a KF-40 sliding feedthrough. Some of these probes will be the sensors for the feedback experiments.

2.3.2 Biasing Electrodes

Figure 2.5 shows one of the large diameter biasing electrodes on the bench. The spherical collection area is roughly 20 cm^2. The collecting surface is connected to a shielded conductor, with a design similar to the floating probes described above. These electrodes will serve as the “actuators”, or output, of the feedback system. Due to the large diameter, these probes are always positioned off the midplane ($\theta \neq 90$, where θ is the polar angle in Figure 2.3) so as to minimize the perturbation to the plasma.

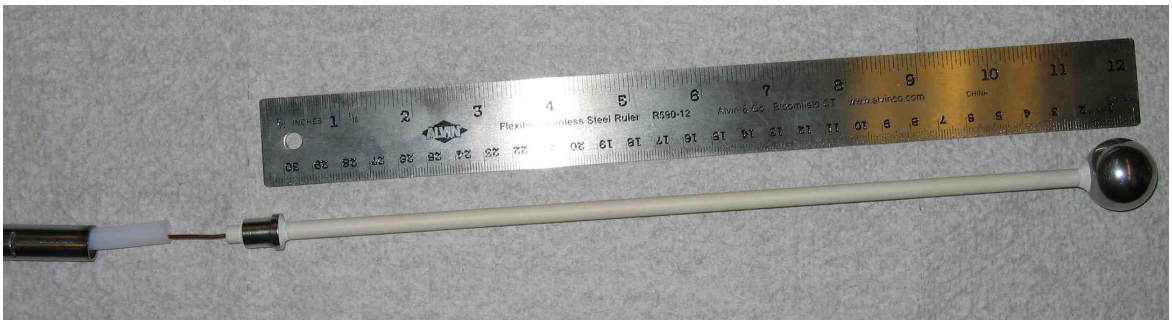

Figure 2.5: Biasing electrode with a collection area of ~ 20 cm^2 will be the "actuator" for feedback. Notice the 12" alumina shaft which connects to the stainless steel feedthrough shaft.

2.3.3 Langmuir Probe

The radially adjustable Langmuir probe used in this study consists of a small square plate, with a collection area of 1 cm^2 on each side. For all experiments this probe was biased to -180 V to collect ion saturation current, as -180 V $>> T_e/e$. This bias is provided by a battery with a parallel 0.1 μF capacitor to improve high frequency response. The structural probe design is similar to the floating potential probe described above.

2.3.4 Polar Imager

A plasma imaging diagnostic, which will be referred to as the "Polar Imager", is positioned on one of the poles of the magnet housing. Consisting of 96 individual gridded particle detectors, it provides measurement of plasma parameters at 12 azimuthal locations on 8 radii. These detectors are positioned on the B $\approx$ 2 kG surface, thus the particles entering each detector have the same gyro radius. Figure 2.6 displays a photograph of this diagnostic as well as an illustration of the magnetic field geometry relative to the detectors.

The housing for this diagnostic is stainless steel spray-coated with 12 mils of alumina, which prevents the generation of field aligned currents. Holes in this housing allow ambipolar flow of plasma to the gridded particle detectors inside. Figure 2.7 is a diagram of these detectors, showing the individually biased stainless meshes in front of a collection plate. By tuning these biases, a particle species, and energy, can be selected for collection, allowing for the mapping of the

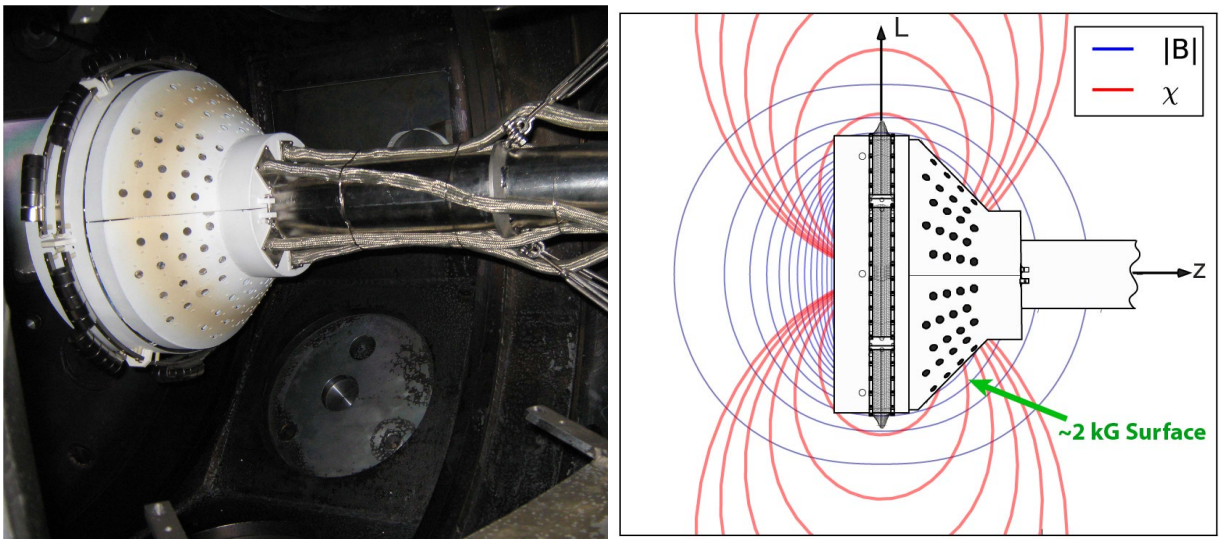

Figure 2.6: Left, a photograph of the Polar Imager in the CTX vacuum chamber. Right, a depiction of the Polar Imager with the magnetic field lines (red) and surfaces of constant B (blue). The 96 gridded particle detectors are all positioned roughly on the 2 kG surface.

phase-space. The first grid is biased to repel electrons, while the second can be biased to repel ions. The third is always biased at -9 V to suppress secondary electron emission at the collector plate.

For the experiments in this work, the bias on these detectors was tuned to collect flux-tube integrated ion saturation current, giving a measure of plasma density at each detector location. A current mapping of the detectors to the corresponding digitizer locations is provided in Appendix D, along with additional details. For a complete description of this diagnostic, refer to the work of the original installation [46], and the upgrade performed to measure the higher density plasmas [50].

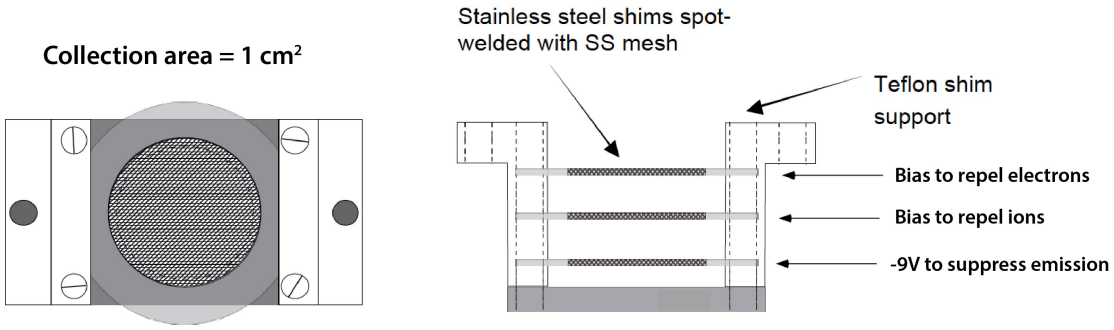

Figure 2.7: Diagram of gridded particle detectors in polar imager. For all the experiments in this work, these detectors were biased to collect flux-tube integrated ion saturation current.

2.3.5 Rake Array

A new diagnostic has been installed on CTX with the potential for multipoint measurement of azimuthal structure with significantly improved resolution. The "Rake" array consists of 31 tips, which alternate as floating potential probes (16) and ion saturation probes (15). With the 16 potential measurements, we can approximate the electric field at the location of the 15 measurements of density. Figure 2.8 shows this diagnostic installed in CTX. Though this diagnostic was installed during the course of this work, no measurements from the array are used in the analysis presented here. A technical description of the Rake array and connections to the digitizing equipment is included in Appendix E for use by future researchers.

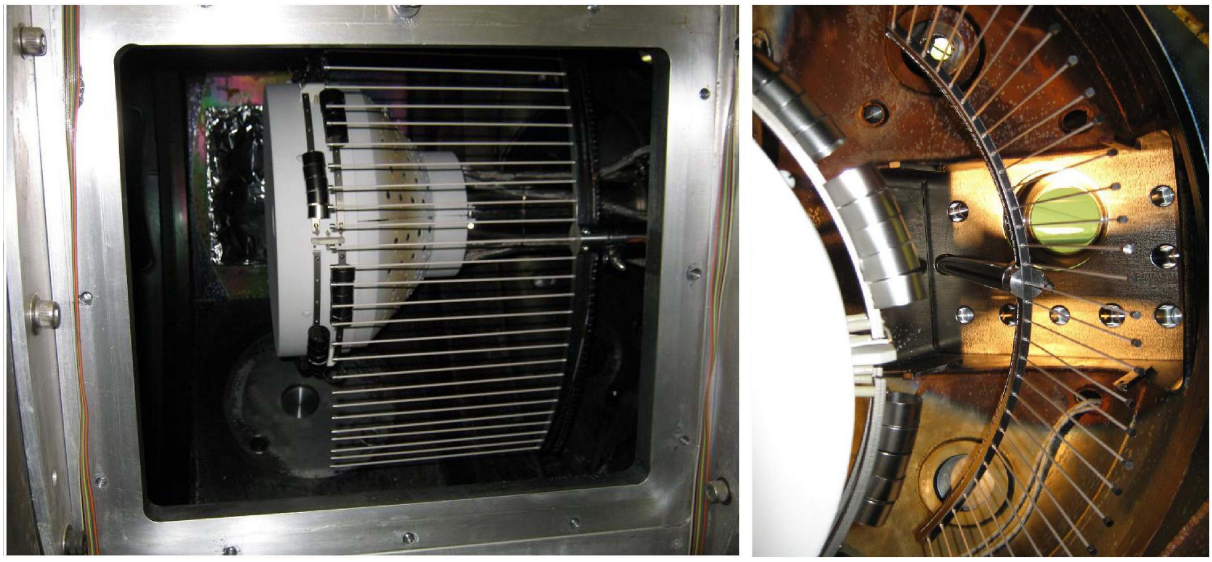

Figure 2.8: Installed Rake array. 31 tips, alternating floating potential and ion saturation probes, give measurements of potential and density fluctuations with enhanced azimuthal resolution.

2.4 Turbulent Plasma Parameters

With sufficient neutral background, the plasmas created in CTX are characterized by quasi-steady turbulence with large amplitude fluctuations in potential and density [50]. This turbulence is produced by interchange motions driven by an unstable pressure profile from microwave heating. The lower portion of Figure 2.9 plots ion saturation current which displays these large fluctuations in density while the upper plot is a log spectrogram of floating potential fluctuations showing the spectral content with time. In this turbulent regime the plasmas are near the cutoff density given by Equation 2.7.

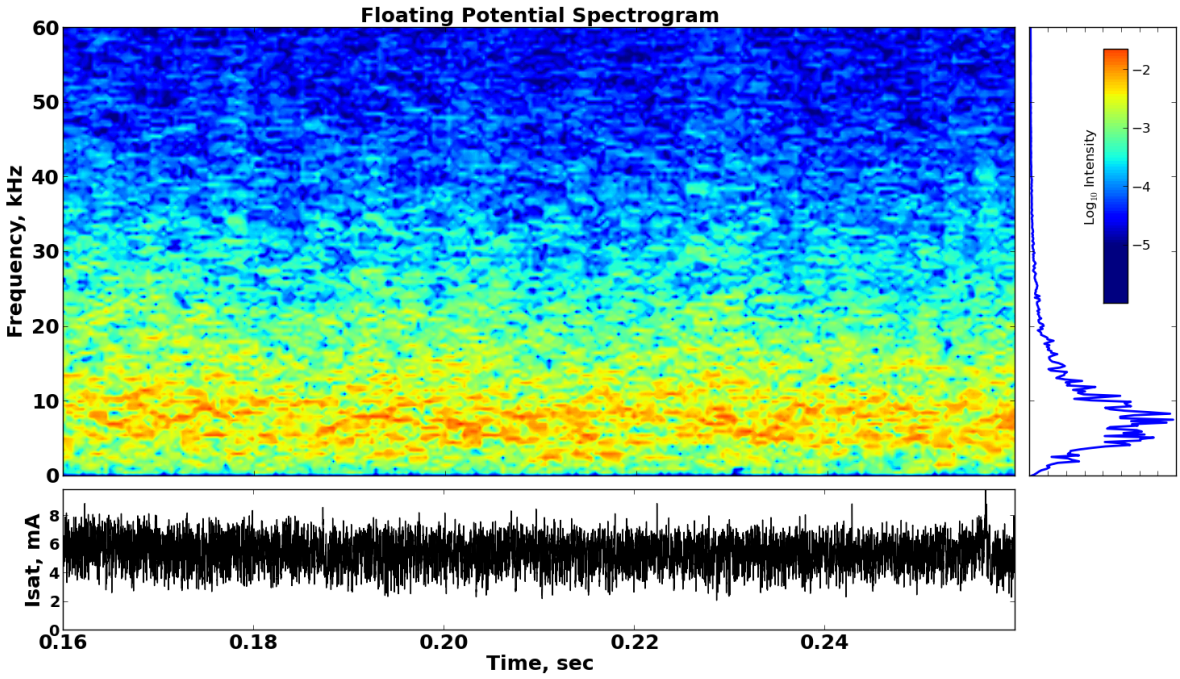

Figure 2.9: Top, a spectrogram of floating potential fluctuations. Right, the ensemble average of the spectrogram displaying the stationary spectrum. Bottom, ion saturation current fluctuations, approximately proportional to density fluctuations.

These plasmas are produced for hundreds of milliseconds, and from the long time records we perform ensemble statistics to observe the stationary spectrum, which is shown on the right of Figure 2.9 for the data in the spectrogram. From these spectra, we observe the turbulence is dominantly in the audio range. Also in the audio range is the electron magnetic drift frequency for electrons with

$T_e \sim 25 - 50$ eV.

Grierson characterized this turbulence and found the modes to be radially broad, low-order, and flute-like in structure [50]. We can visualize these modes with the Polar Imager, as shown in Figure 2.10. These modes are dominantly m = 1, 2 and 3 in structure, rotating in the electron magnetic drift direction with amplitudes and phases which varies chaotically in time [13]. Cross correlation analysis gives a combined turbulent correlation length of $50° - 75°$ azimuthally.

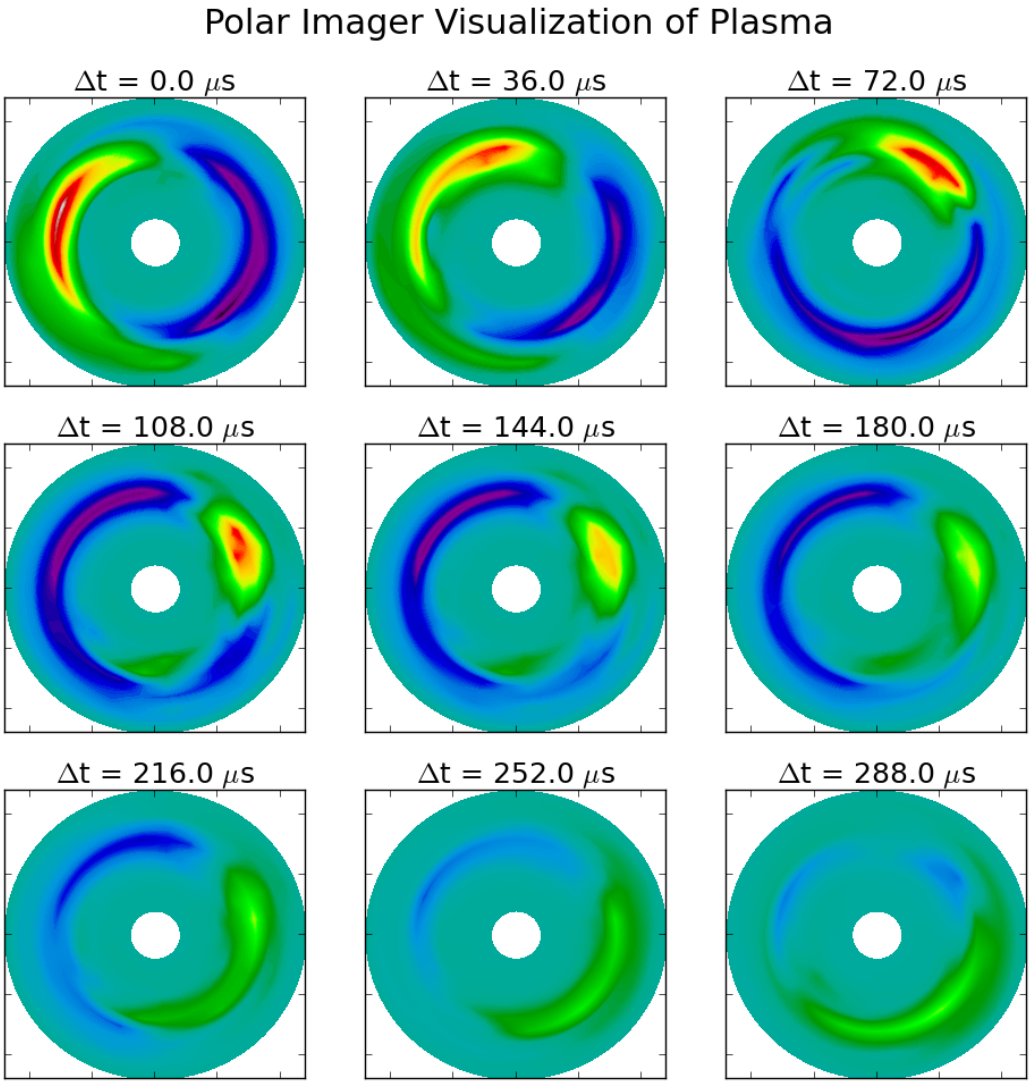

Figure 2.10: Viewing the plasma with the Polar Imager. An m = 1 mode is observed to rotate in the electron magnetic drift direction. Notice the amplitude varies in time (all color bars the same), and the appearance of some higher order modes.

The turbulent spectra are also observed to obey power law scalings representative of turbulent cascades. Figure 2.11 [1] shows the power spectrum for potential and density, and energy spectrum [51, 52] given by,

$$E_k = \left(\frac{\tilde{n}_k}{\bar{n}}\right) + k^2\rho_s^2\left(\frac{e\tilde{\Phi}}{T_e}\right) \tag{2.8}$$

where the slopes (-5 and -3) indicate of a forward enstrophy cascade and an inverse energy cascade, a signature of two dimensional turbulent dynamics [50, 53].

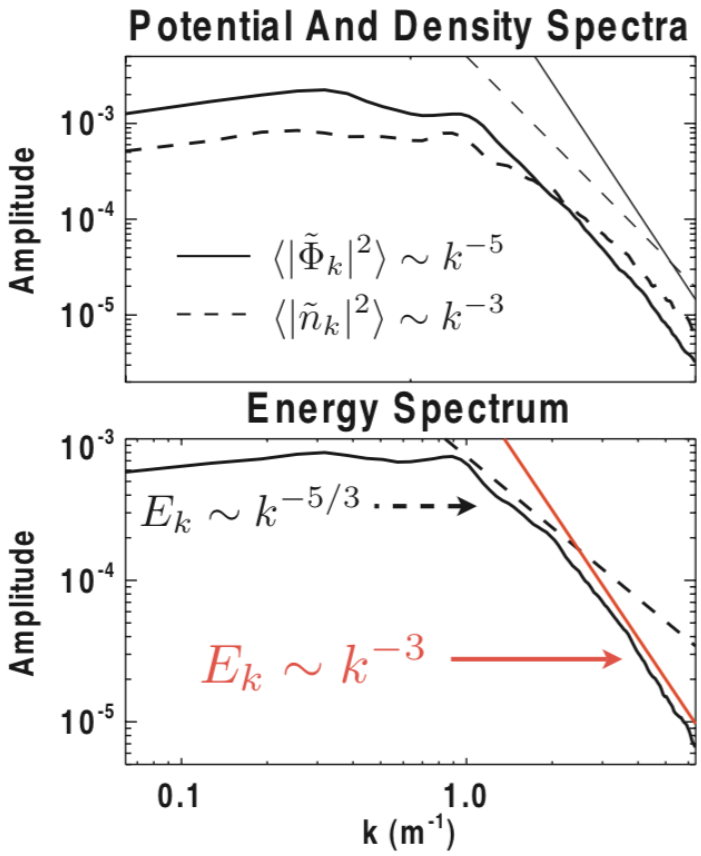

Figure 2.11: Fluctuations display power law trends indicative of the inverse energy cascade.

Most of the experiments described in this thesis were performed near an equitorial radius of 45 cm. For a quick reference of the relevant plasma parameters and the characteristics of the turbulence, Table 2.1 is provided. A more detailed discussion of the CTX parameters is given in Appendix A.

[1] Image credit to Grierson [13]

Table 2.1: Plasma and turbulence parameters at L = 45 cm

Mean Plasma Density	$\bar{n}$	$\sim 7 \times 10^{10}$ cm^{-3}
RMS Plasma Density	$\tilde{n}$	$\sim 3 \times 10^{10}$ cm^{-3}
Floating Potential	$\bar{V}_f$	~ 25 V
Fluctuating Potential	$\tilde{V}_f$	~ 4 V
Electron Temperature	T_e	$25 - 50$ eV
Electron Drift Frequency	ω_{de}	2-4 kHz
ECR Frequency	f_μ	2.45 GHz
Electron Cyclotron Frequency	f_{be}	500 MHz
Ion Cyclotron Frequency	f_{bi}	250 kHz
Electron Bounce Frequency	f_{be}	1.5 MHz
Ion Bounce Frequency	f_{bi}	7 kHz
B Field @ Resonance	B_0	875 Gauss
Correlation Time	τ_c	$\sim 75\mu$s
Correlation Length (m)	l_c	40-60 cm
Correlation Length (°)	θ_c	50-75°

Chapter 3

Feedback System Design

The experiments mentioned in Chapter 1 and described in detail in Chapter 4 were performed using a feedback system composed of a sensor, filtering/amplifying circuit and electrode. This chapter briefly discusses the theory of this simple feedback system, then describes the design of the feedback circuit. As will be shown, this analog circuit is composed of various filters and amplifiers in series which apply variable phase shifts and gains to the input signal.

3.1 Principles of Feedback

Before discussing the specifics of the feedback system, we briefly review the basic control theory applicable to these experiments. Due to the simple nature of the control law applied, this introduction is minimal. For a more complete introduction, a fantastic review of feedback theory is provided by Bechhoefer [54].

Several of the basic concepts from control theory can be described with the simple example of a car's cruise control system. The car is traveling down the highway at some speed, v. The driver sets the cruise control system at this speed v and takes his or her foot off the gas pedal. A sensor measures the velocity of the car and compares the measured velocity to the "set point" velocity. If drag due to air and rolling resistances has slowed the car, the difference between the measured velocity and the set point produces an error signal. A "control law" is applied to this error which

determines the response sent to an actuator which rotates the valve on the throttle body, increasing air/fuel flow to the engine, accelerating the car. The velocity is measured again and the cycle repeats. The block diagram for this system is shown in Figure 3.1.

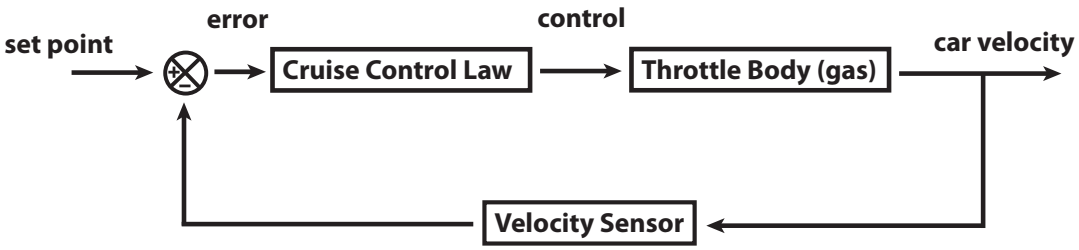

Figure 3.1: An example feedback system; a car's cruise control.

The control law used determines the dynamics of the system with feedback. The simplest control law is referred to as "proportional gain", where the error signal is multiplied by a constant which is then passed to the actuating system. This is the nature of feedback we apply to the turbulent fluctuations in CTX. The fluctuating potential of the plasma is measured by a sensor, which is then passed to the feedback circuit which applies a gain to that signal. This "control signal" is then input to the plasma via an electrode (actuator) and the plasma responds. The sensor measures the change in the plasma and the loop starts again. This system is displayed in Figure 3.2.

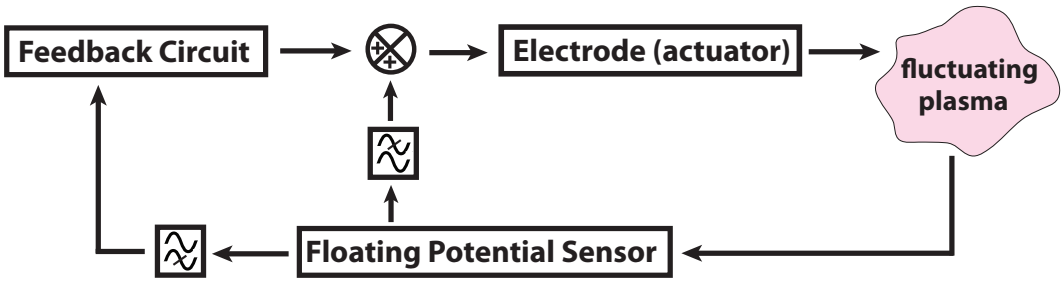

Figure 3.2: Block diagram of the plasma-feedback system. Notice the control is only applied to the fluctuations of the potential, as indicated by the low-pass and high-pass filters.

A subtle difference between this system and the car's cruise control is the set point used. For the car, a fixed value was set as the desired speed of the car. In the plasma, we are measuring only fluctuations in the potential, and the control signal is added to the DC potential of the plasma, as illustrated in Figure 3.2. This will be explained in the following section.

3.2 Feedback System Design

The feedback system for these experiments is composed of three main elements; a sensor, an actuator and a circuit to adjust the signal between the first two. The sensor is a floating potential probe which measures fluctuations of potential in the plasma. The actuator is a large diameter biasing probe with which we can drive current into the plasma. The circuit that connects the sensor and actuator represents the block labeled "Feedback Circuit" in Figure 3.2 and applies the control law. Some of the fundamentals of filter/op-amp theory are explained in detail in Appendix F, but are more thoroughly reviewed elsewhere [55, 56, 57].

3.2.1 Overall Feedback Circuit Design

The phasing of the input signal determines whether we are applying positive or negative feedback and is adjusted with a filter that imposes a linear phase shift on the measured plasma fluctuations. Next, we wish to apply feedback only to the fluctuations of interest, excluding the low frequency oscillations (and DC offset) of the plasma. The signal from the sensor is input to the feedback circuit, but also recorded. We prevent the measured signal from being distorted with a buffer between the sensor signal and the high-pass filter. We also use this buffer to pre-amplify the input signal. A block diagram of the entire circuit is shown in Figure 3.3.

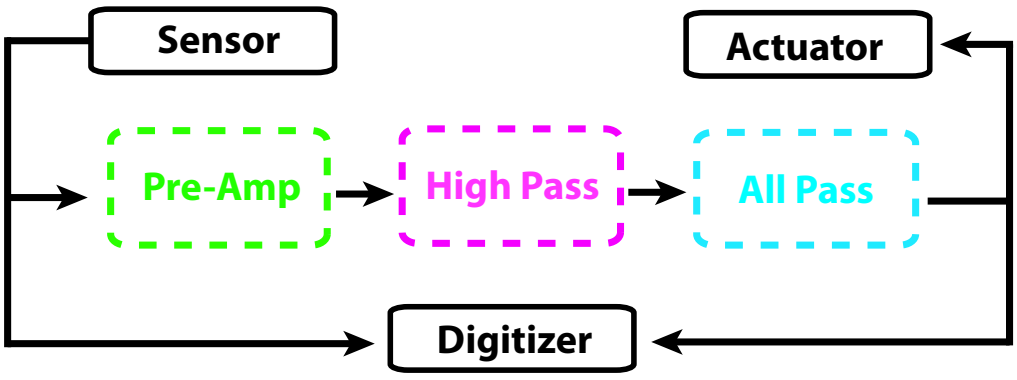

Figure 3.3: The fundamental components for the feedback circuit.

3.2.2 Pre-Amplifier/Buffer

Starting with the first part of the circuit, the high input impedance of the non-inverting buffer/amplifier prevents the feedback circuit from effecting the recorded sensor signal. This is crucial for measurement of the applied phase shift and modification of the turbulent spectrum with feedback. A circuit diagram is shown in Figure 3.4.

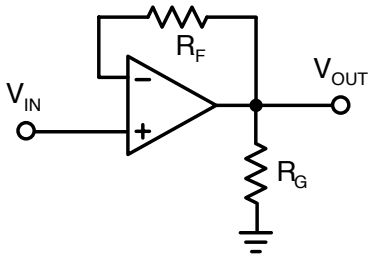

Figure 3.4: Buffer element. Gain is set through choice of the gain and feedback resistors.

We can make a unity gain buffer by setting R_F to zero and allowing R_G to go to infinity. As the signal from the floating probe is resistively divided for digitization, modest amplification was imposed by choosing $R_F = 32.8$ kΩ and $R_G = 10.0$ kΩ, which corresponds to a gain of 4.28, as given by:

$$G = 1 + \frac{R_F}{R_G} \tag{3.1}$$

This gain was used for the majority of the experiments described in this thesis as the maximum gain applicable within the limitations of the later stage four-quadrant amplifier. Chapter 4.4 describes varying the gain of the feedback system, where these resistor values are modified to reduce the overall gain.

3.2.3 High-Pass Filter

The turbulent dynamics we are studying are in the range of 500 Hz - 15 kHz, so we design a filter to neglect frequencies sufficiently lower than 500 Hz. The simplest high-pass filter is a passive circuit composed of resistor and capacitor, but improved performance is obtained with active elements. The general transfer function for high-pass filter is given as:

$$H(s) = \frac{H_\infty}{\Pi(1 + \frac{c_{1i}}{s} + \frac{c_{2i}}{s^2})} \tag{3.2}$$

where the c_i are coefficients of the partial filters. Choice of these coefficients is what determines our filter characteristics and are tabulated in various sources [55].

The second-order Sallen-Key topology was sufficient and is shown in Figure 3.5.

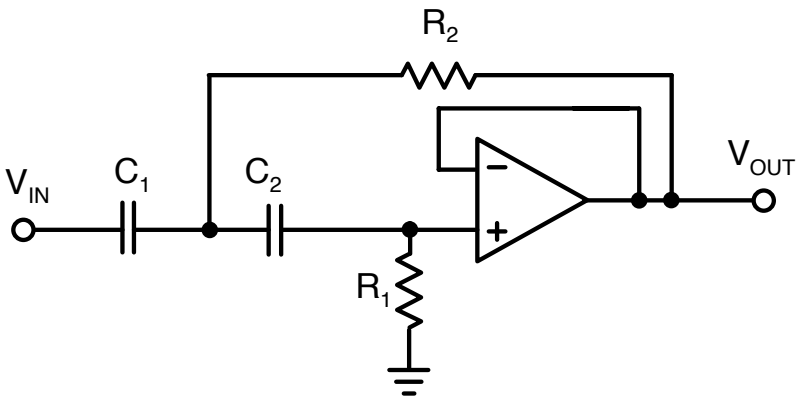

Figure 3.5: Second-order Sallen-Key high-pass filter.

For simplicity, we choose $C_1 = C_2 = C$, and apply no gain with this portion of the circuit. With these choices, the transfer function is given as:

$$H(s) = \frac{1}{1 + \frac{2}{\omega_c R_1 C}\frac{1}{s} + \frac{1}{\omega_c^2 R_1 R_2 C^2}\frac{1}{s^2}} \tag{3.3}$$

where ω_c is a normalization for the coefficients based on the filter's corner frequency.

By choosing a reasonable value for C, we can solve for R_1 and R_2 with the coefficients:

$$c_1 = \frac{2}{\omega_c R_1 C} \qquad c_2 = \frac{1}{\omega_c^2 R_1 R_2 C^2} \tag{3.4}$$

which, solving for resistance yields,

$$R_1 = \frac{1}{c_1 \pi f_c C} \qquad R_2 = \frac{c_1}{4 c_2 \pi f_c C} \tag{3.5}$$

With all the necessary values for this component, we choose elements with values close to these (rule of thumb, capacitors within 10%, resistors 5%). The final values were $C = 0.1\,\mu$F, $R_1 = 10.0\,\text{k}\Omega$, $R_2 = 21.8\,\text{k}\Omega$ for a corner frequency of 120 Hz. The Spice generated amplitude and phase response for this component are plotted in Figure 3.6.

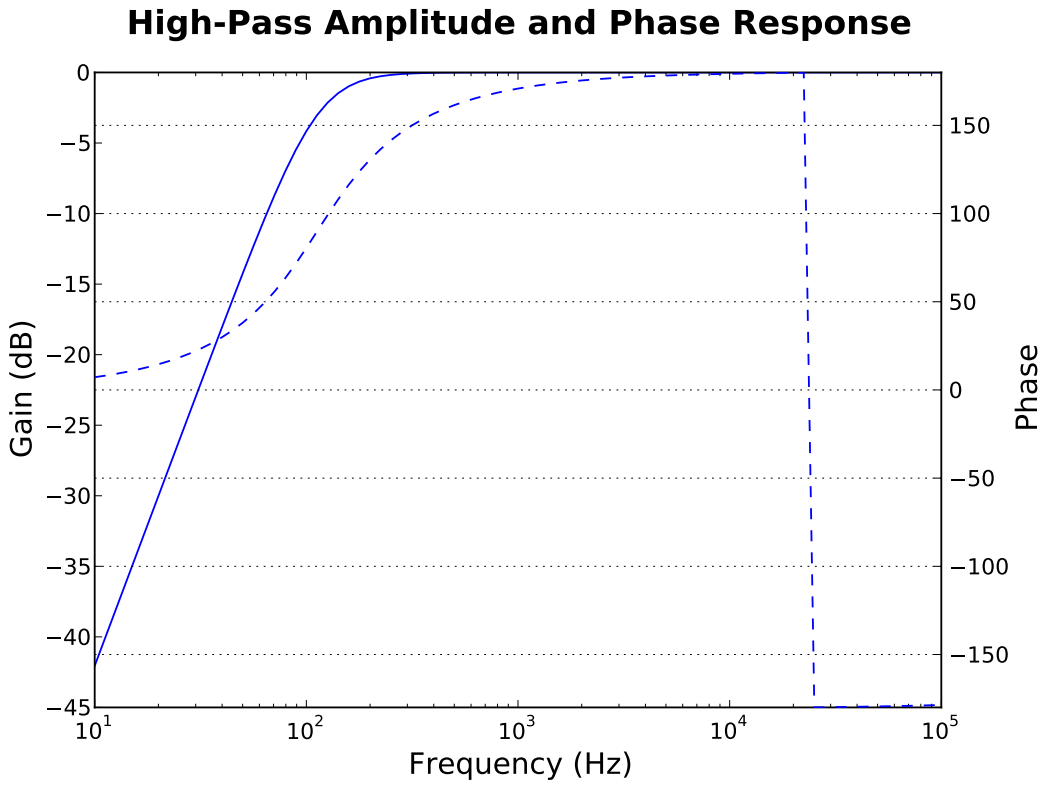

Figure 3.6: Amplitude and phase response of the high-pass filter.

3.2.4 All-Pass Filter (Phase Shifter)

We next require the ability to apply adjustable phase shifts to the input signal from $0° \rightarrow 360°$. Phase shifts are achieved through a filter with unity frequency response, which is designed to impose a linear phase shift with frequency for the pass-band of interest. This is realized through cascading two all-pass filters, each capable of applying nearly 180° shifts.

The transfer function for an all-pass filter can be found by taking the transfer function of the low pass filter and setting H_0 equal to the complex conjugate of the denominator:

$$H(s) = \frac{H_0}{\Pi(1 + c_{1i}s + c_{2i}s^2)} \qquad \rightarrow \qquad H(s) = \frac{\Pi(1 - c_{1i}s + c_{2i}s^2)}{\Pi(1 + c_{1i}s + c_{2i}s^2)} \tag{3.6}$$

This gives a phase shift of ϕ, where the group delay is defined as $t = -\frac{d\phi}{d\omega}$. To minimize phase distortion we need constant group delay across the frequency band. We define the corner frequency of an all pass filter as the frequency at which the group delay drops by $1/\sqrt{2}$, and as such can normalize the group delay as $T = tf_c$. This normalized group delay allows us to quantify the "sharpness" of the constant group delay.

For our purposes we chose to use a first-order all-pass filter (Figure 3.7). This topology requires only one resistor be changed to alter the applied phase shift, making shot-to-shot adjustment simple.

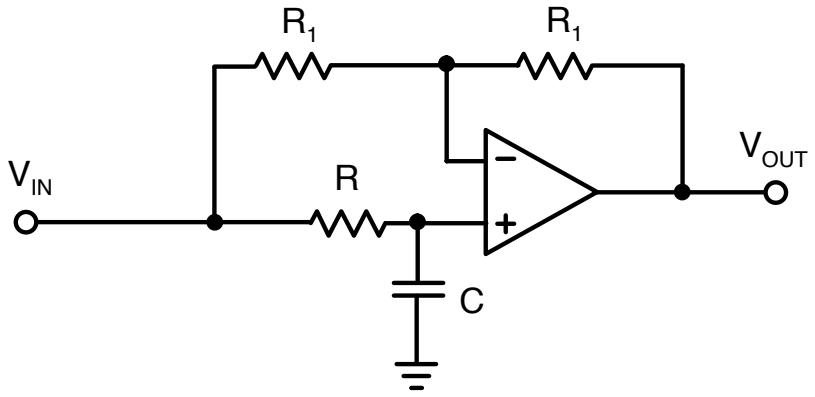

Figure 3.7: Circuit diagram for first-order all-pass filter.

Interchange of the capacitor C and the resistor R simply results in a 180° phase shift. Choosing

our corner frequency to be 20 kHz, $R_1 = 10\,\text{k}\Omega$, and C to be $0.1\mu F$, we find our resistor values from:

$$R = \frac{a_i}{2\pi f_c C} \tag{3.7}$$

which has a phase response as given in Figure 3.8.

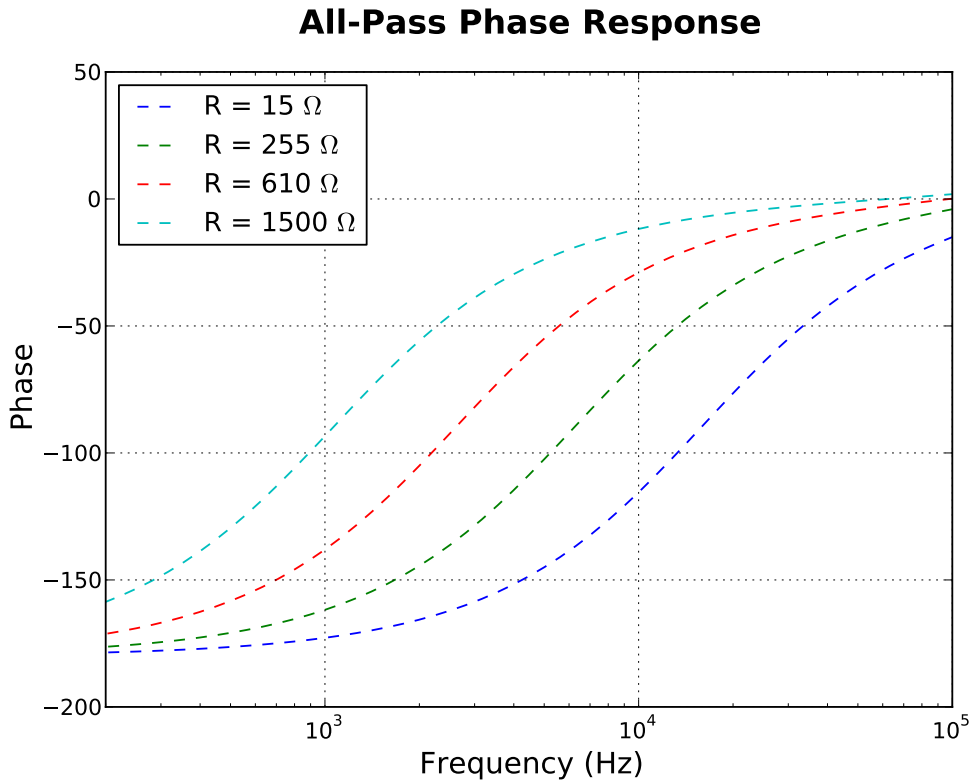

Figure 3.8: Phase response of first order all pass filter for various resistor settings.

We make this an adjustable phase shifter by making R a variable resistor. To get nearly a $0^\circ \rightarrow 180^\circ$ phase shift, we need to resistances in the range from 0-10 kΩ. Most of the change in phase takes place between 0-1 kΩ, so by installing two potentiometers in series, one 10 kΩ and other 1 kΩ, we can obtained range and resolution.

3.2.5 Measured Performance of Circuit

By combining the above components, we build the complete circuit for our feedback system, as shown in Figure 3.9. The signal from the sensor is recorded and passed through a pre-amplifier. This stage both isolates the recorded sensor signal from the feedback circuit and allows the application of gain by varying the "R_F" resistor. The signal is next high-pass filtered with a corner frequency of 120 Hz to remove DC and low frequency equilibrium dynamics. Next, a phase shift is applied by two cascaded all-pass filters, where the applied phase shift is varied by tuning the resistors labeled "R" in the all-pass filters shown in Figure 3.9. This is then input to an HP 6827A four-quadrant voltage controlled amplifier (fixed 20x gain, inverting) and AC coupled to the electrode with a series 12 μF bipolar capacitor.

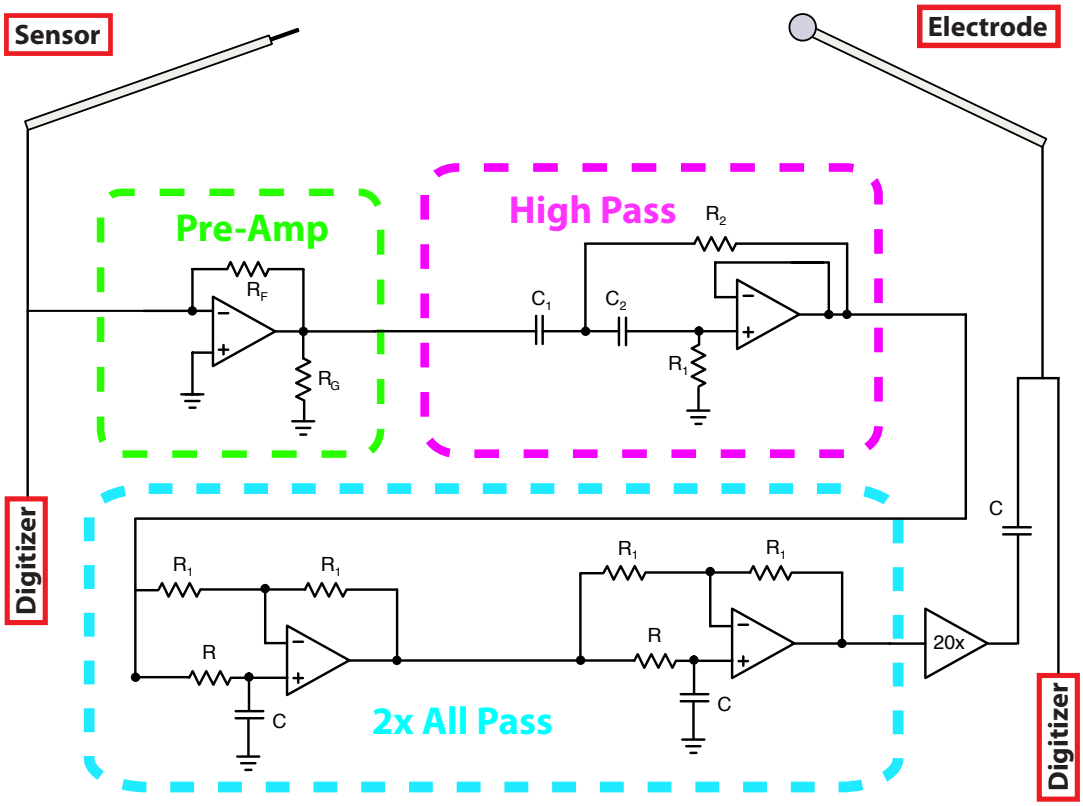

Figure 3.9: Complete feedback circuit. The signal from the sensor is passed through a pre-amplifier, high-pass filtered, then phase shifted. This is then input to a four-quadrant amplifier and AC coupled to the electrode with a series 12 μF bipolar capacitor. The phase is varied by adjusting "R" in the all-pass filters, and gain is determined by the "R_F" resistor in the pre-amplifier.

Both the current driven into the electrode and the bias are recorded after the coupling capacitor. By measuring the voltage before and after the feedback circuit, we can determine the transfer function of the feedback system. Figure 3.10 (a) shows this phase response for various resistor settings in circles for the experimentally measured values (in plasma) and in triangles for the SPICE simulation. We observe that these values diverge from the predicted values at increasing frequency. Figure 3.10 (b) compares the phase response of the circuit at the tuning frequency of 3 kHz (in vacuum), we see a constant offset in phase of $\sim 5^{\circ}$.

By measuring the phase response at each setting, we can observe the plasma's response to feedback for a given transfer function. We will use this in the next chapter to better quantify the change in the turbulent spectrum with feedback.

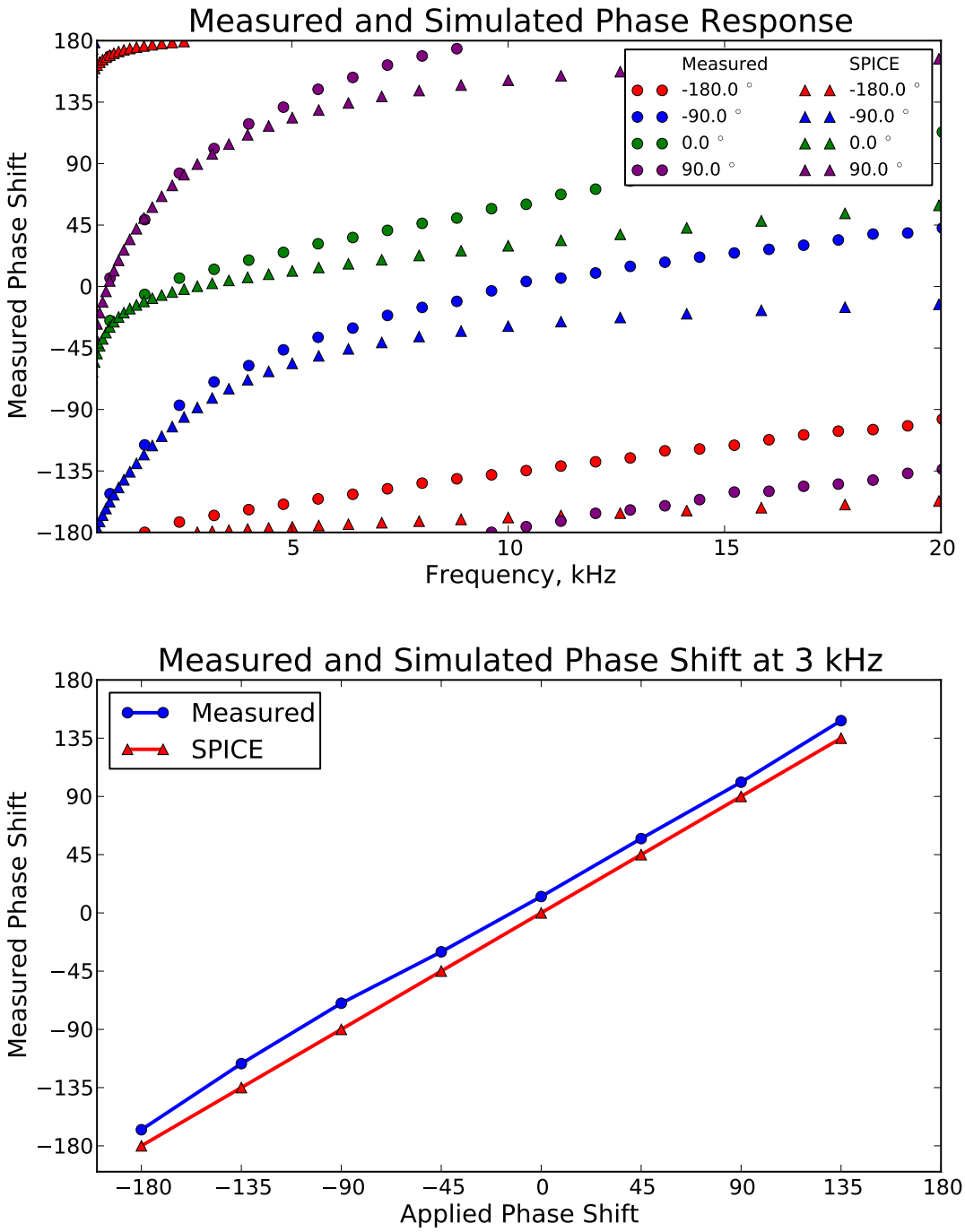

Figure 3.10: Comparison of the measured and SPICE simulated phase response of the feedback circuit. Top, the circles show the measured phase response with applied feedback at the indicated phase setting (at 3 kHz) as determined from the cross phase between the sensor and electrode voltage measurements. The triangles show the spice calculated phase response at the same resistor settings. Bottom, the measured and calculated phase shifts at the tuning frequency of 3 kHz. There is an approximately constant shift of $\sim 5°$.

3.3 Feedback Configuration in the CTX Device

The sensor and electrode described in the previous section can be positioned in the CTX vacuum chamber in a variety of configurations. While radial adjustment was studied, we focus on the azimuthal positioning of the sensor and electrode relative to one another and the direction of mode rotation. Figure 3.11 shows two possible locations for the sensor and electrode which vary the separation.

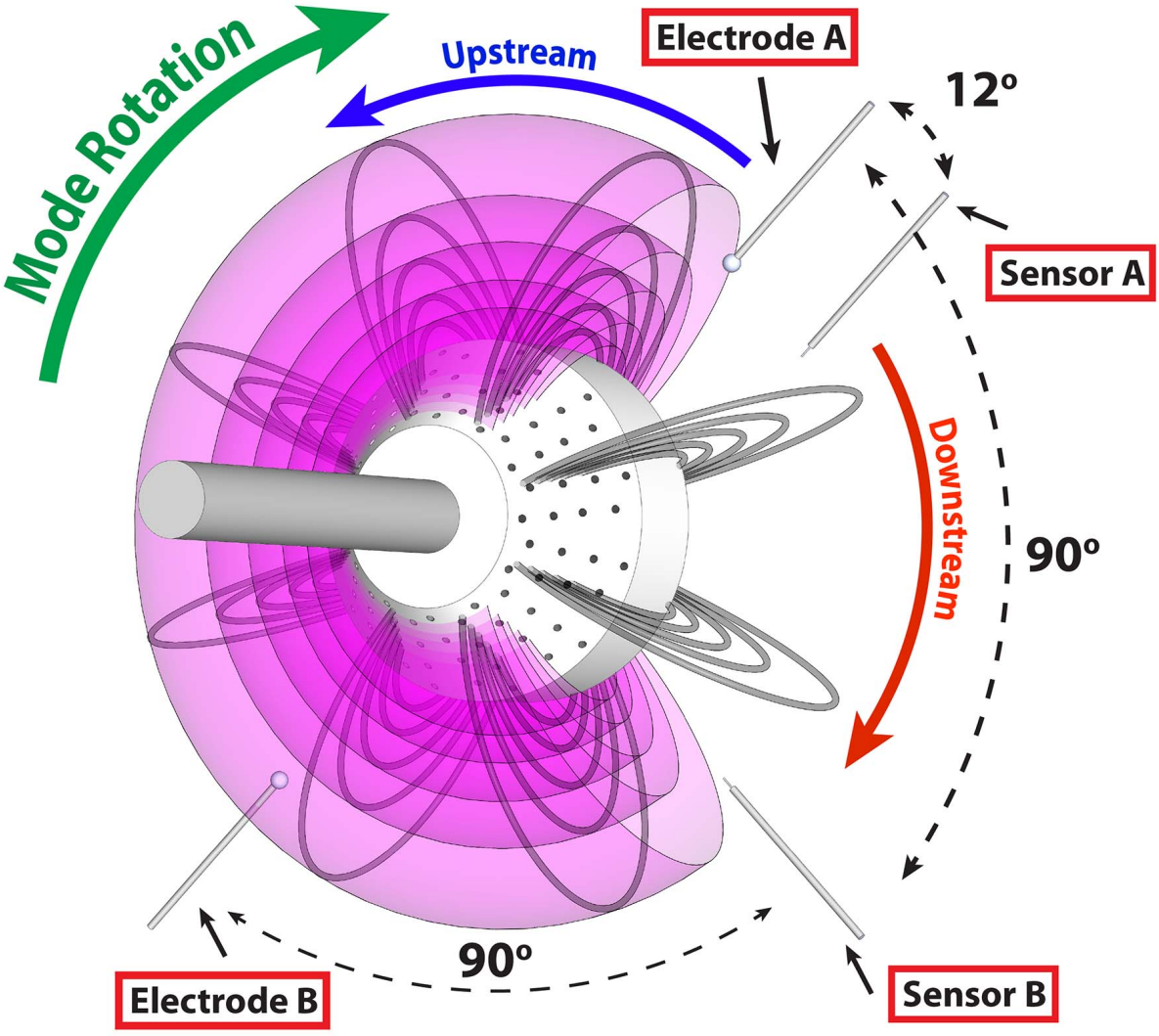

Figure 3.11: The possible sensor and electrode positions in the CTX vacuum chamber. The indicated mode rotation direction, determines a convention. Red is a "downstream" region of the plasma (relative to Electrode A), blue is an "upstream" region.

As will be shown in the next chapter, the direction of mode rotation changes the effective separation between the sensor and electrode. We reverse the rotation by reversing the magnetic field polarity, which give us further adjustment of the separation. We will using the direction of mode rotation and the position of the electrode to define a convention used throughout the rest of this dissertation; regions of the plasma past the electrode in the direction of mode rotation (as indicated in red in Figure 3.11) will be referred to as "downstream", and regions before the electrode (blue) are "upstream".

It should be noted that both sensors and electrodes were located off the mid-plane to be less perturbative. As the field aligned dynamics are effectively zero ($k_{\|} \approx 0$), the dynamics measured at the higher polar angles maps to the entire field line. The radial location of all sensors and electrodes were set such that they sit on field lines that trace to an equatorial radius of L = 45 cm. This was found to maximize the influence of the feedback from performed radial scans.

Chapter 4

Plasma Response to Feedback

This chapter describes the application of the feedback system described in the previous chapter to the CTX plasmas. The plasma created with and without feedback are compared showing clear modification of the fluctuation amplitude and spectrum. These comparisons were made between plasmas with the feedback on continuously, and plasmas where the feedback is triggered on and off during the shot. The spectrum is observed to respond strongly to both the phase and gain of the applied feedback, with the influence of the feedback attenuating with increasing separation from the electrode. The locations of the sensor and electrode were varied azimuthally and it was found that the relative separation in the direction of mode rotation plays a significant role effectiveness of the feedback system.

4.1 Testing the Open-loop Response: Feedforward

Before applying feedback, we first test the open-loop response of the system by driving the electrode with a known signal and observing the plasma response. A 4 kHz sine wave was input to the HP amplifier, producing a ±40 V signal on the capacitively coupled electrode. This is illustrated in Figure 4.1, where the electrode (labeled "Driver") is the output of this feedforward system. The direction of mode rotation is illustrated by the green arrow.

In this configuration we measure the power spectrum of the floating potential probe located 12°

downstream from the electrode. A coherent wave at the driven frequency is observed, as is shown in the upper plot of Figure 4.2 by the red curve. If we look at the response measured by an identical probe located 90° downstream, we observe the same wave, but reduced in intensity, as shown by the green curve. Looking now 90° upstream, the blue curve shows a significantly reduced peak at 4 kHz, indicating little response to the driven current.

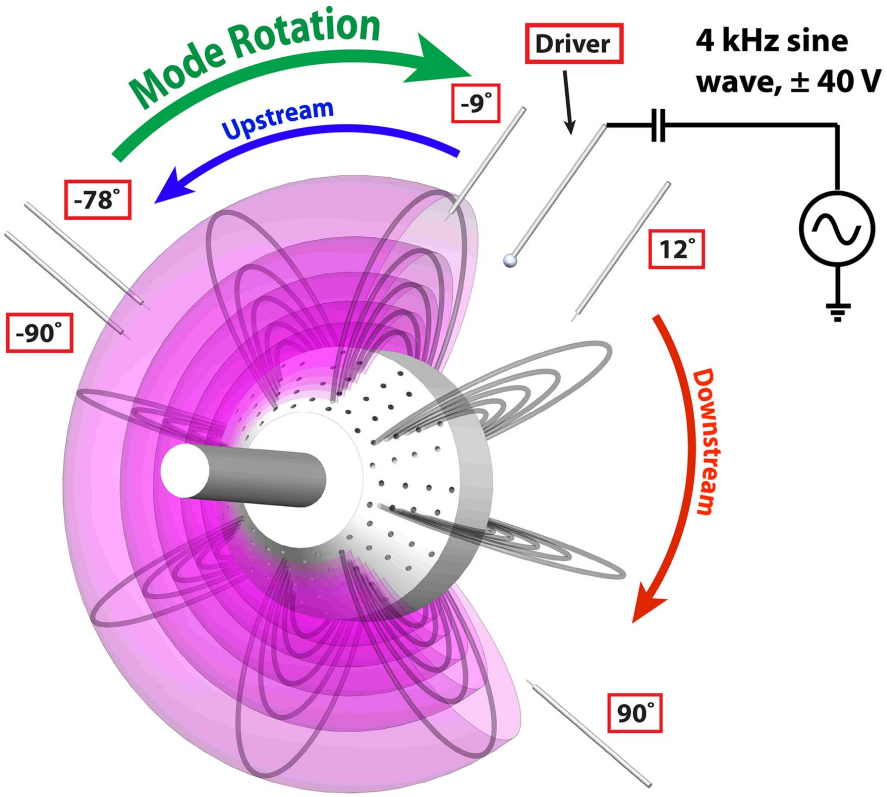

Figure 4.1: Experimental configuration for open-loop tests. An electrode is driven at 4 kHz, 80 V peak-to-peak. The azimuthally positioned floating probes are used to measure the attenuating influence in the direction of mode rotation.

The lower plot of Figure 4.2 shows the relative change in spectral power at 4 kHz as measured by all five of the floating potential probes. The probes are positioned azimuthally relative to the electrode indicated by the dashed line. With respect to the direction of mode rotation, we observe a significantly reduced upstream influence of the driven current relative to the downstream effects. We determine that the influence of current injection is localized and shifted in the direction of the electron magnetic drift, (same as mode rotation).

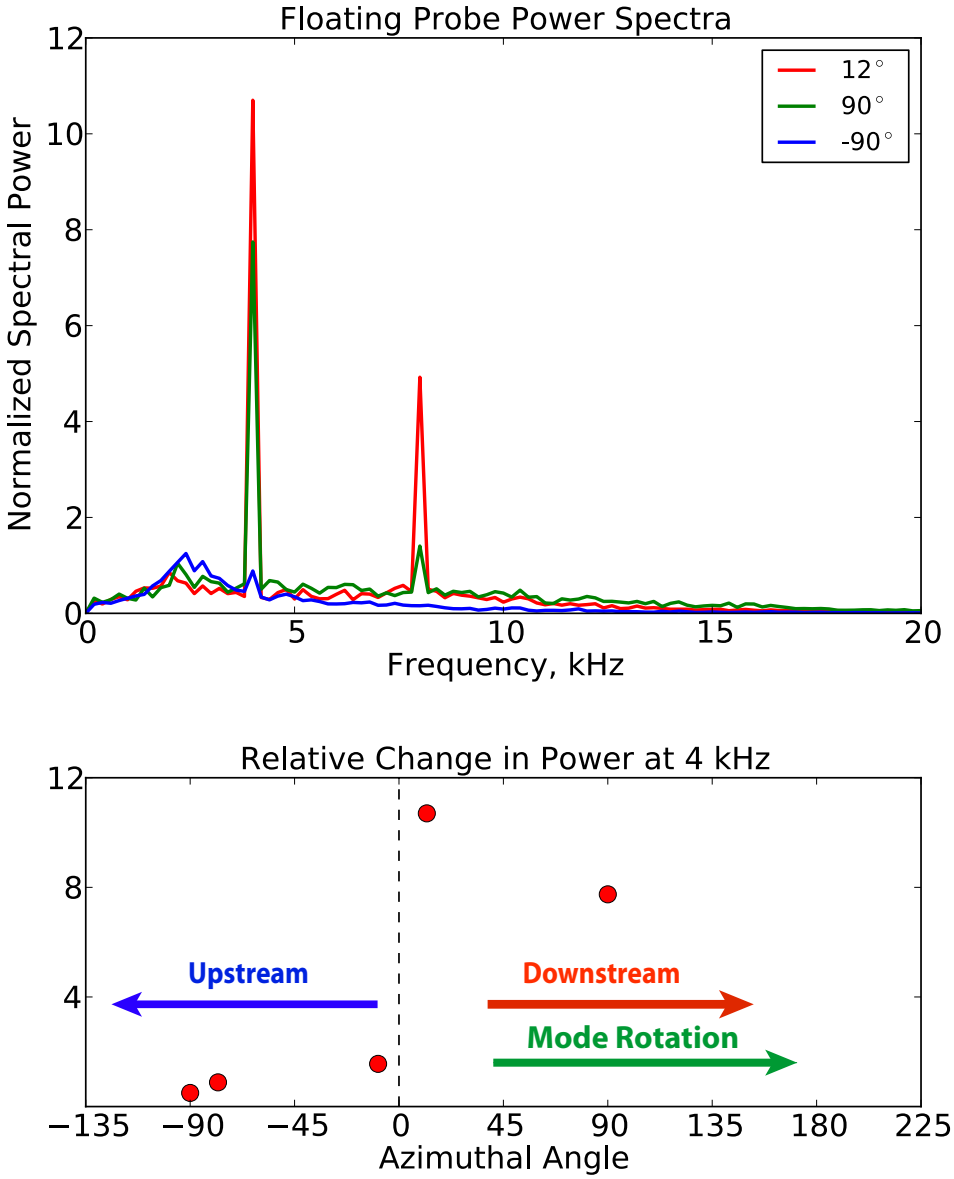

Figure 4.2: Top, power spectra of three floating potential probes while driving a 4 kHz signal on the electrode. Bottom, the relative change in spectral power at the driven frequency as measured on all five floating probe. The amplitude decreases with separation and the oscillations appear to be carried only in the direction of mode rotation.

Figure 4.3 plots the current (red) and bias (blue) on the electrode as measured when driving the 4 kHz signal. We find that the driven current is in phase with the bias. Thus, the power driven by the electrode into the sheath is always positive, which will be important in our power flow analysis later in this chapter. The current is asymmetric about zero due to the mobility of electrons and the limit of ion saturation current. Note that due to the capacitive coupling, the current in time must sum to zero. The capacitive coupling also allows the probe to float to the DC floating potential, which is near -40 V in this plot.

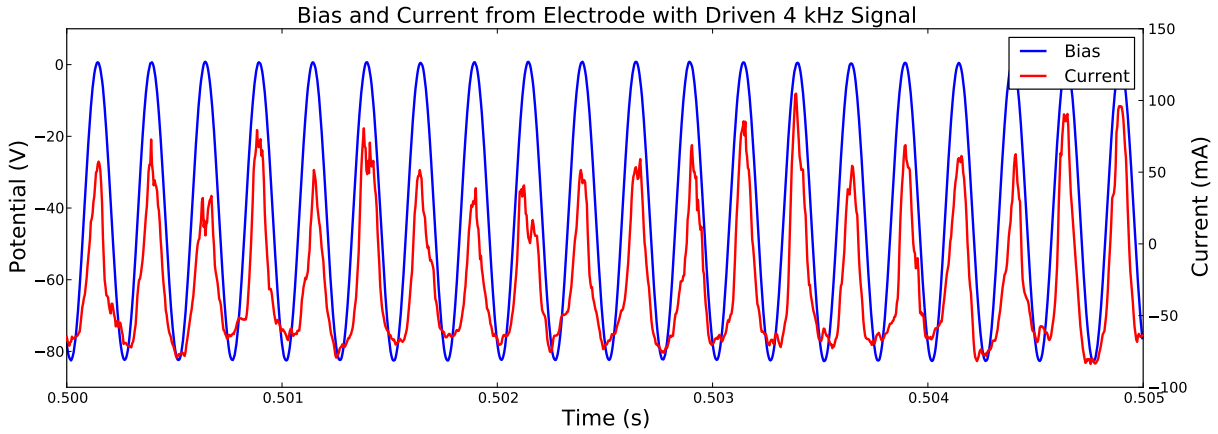

Figure 4.3: Current (red) and bias (blue) of the electrode when driving the 4 kHz signal. Note the limit of ion saturation current and the DC floating potential.

The IV trace from this signal is shown in the upper plot of Figure 4.4. In the lower plot, analysis investigates hysteresis in this voltage sweep by differentiating between the increasing (blue dots) and decreasing (green dots) portions of the trace. The red and cyan curves show the averages of these separate portions. As the increasing and decreasing portions of the characteristic show effectively no hysteresis, we find the sheath of the electrode to behaves resistively (very little inductive or capacitive behavior). The resistance near floating potential is approximated as 400 Ω from a linear fit, though is significantly less at more positive voltages. We will use these assumptions in the eigensystem discussed in Chapter 5.

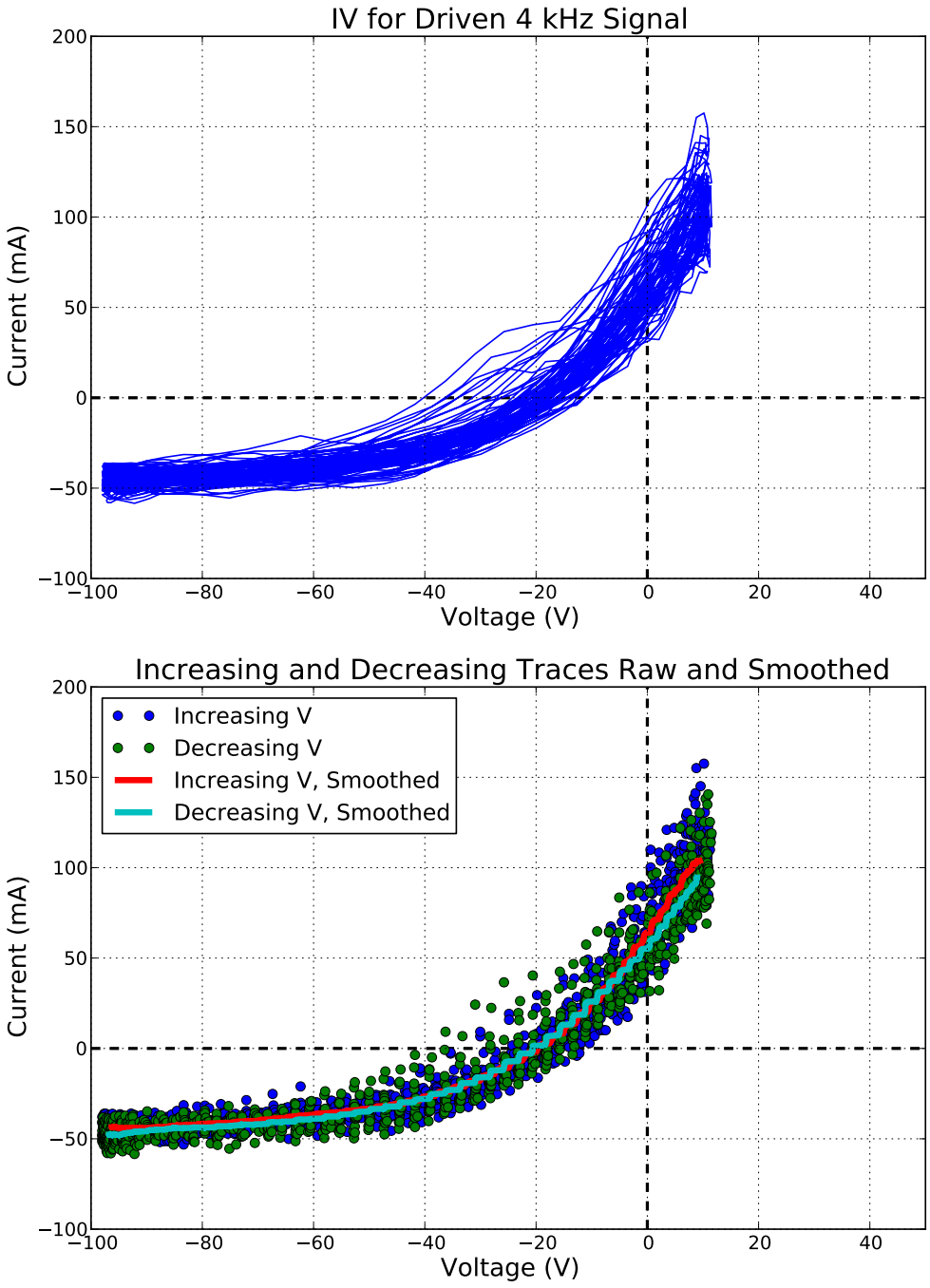

Figure 4.4: Top, IV trace from the 4 kHz driven signal. Bottom, analysis of the IV sweep indicates resistive sheath behavior with a resistance of 400 Ω near floating potential.

4.2 Closing the Loop: Feedback

By replacing the driving input signal of the feedforward experiments with a measure of the plasma fluctuations, we create our feedback system. As described in the previous chapter, a measure of floating potential is used as input. In doing so, we find we can excite or suppress the natural oscillations of the plasma. Figure 4.5 shows the configuration of the feedback system of Chapter 3, where the sensor is located 12° downstream from the electrode.

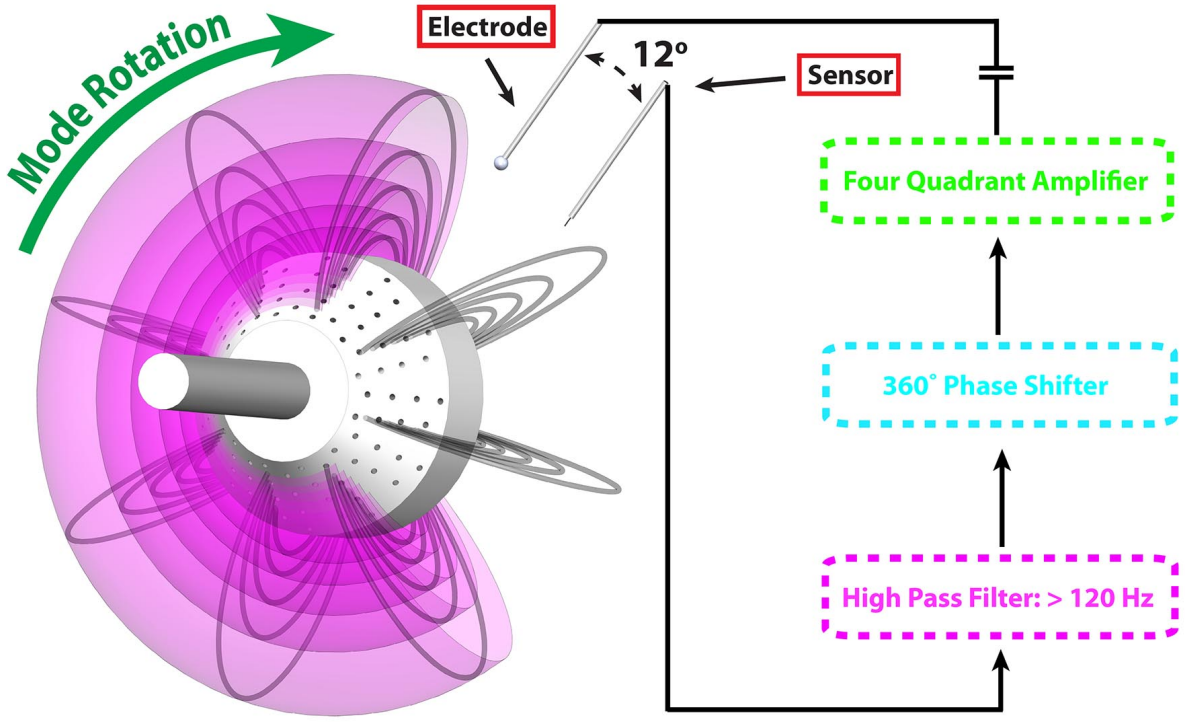

Figure 4.5: Experimental configuration for feedback. Notice here the sensor is a floating potential probe located 12° upstream from the electrode.

Figure 4.6 displays an example of the measured fluctuations from the sensor and electrode when we apply feedback which is in phase with the sensor measurements (red) or 180° out of phase (blue). Comparing the sensor voltage (a) to the electrode voltage (b), we see the imposed amplification of a factor of four, and the inversion of the blue curve. Looking at the electrode current for these cases (c), we see that the current is generally in phase with the electrode voltage. This would indicate positive power driven by the electrode which will be discussed later. The IV characteristic of the electrode for the two cases is shown in (d) and (e).

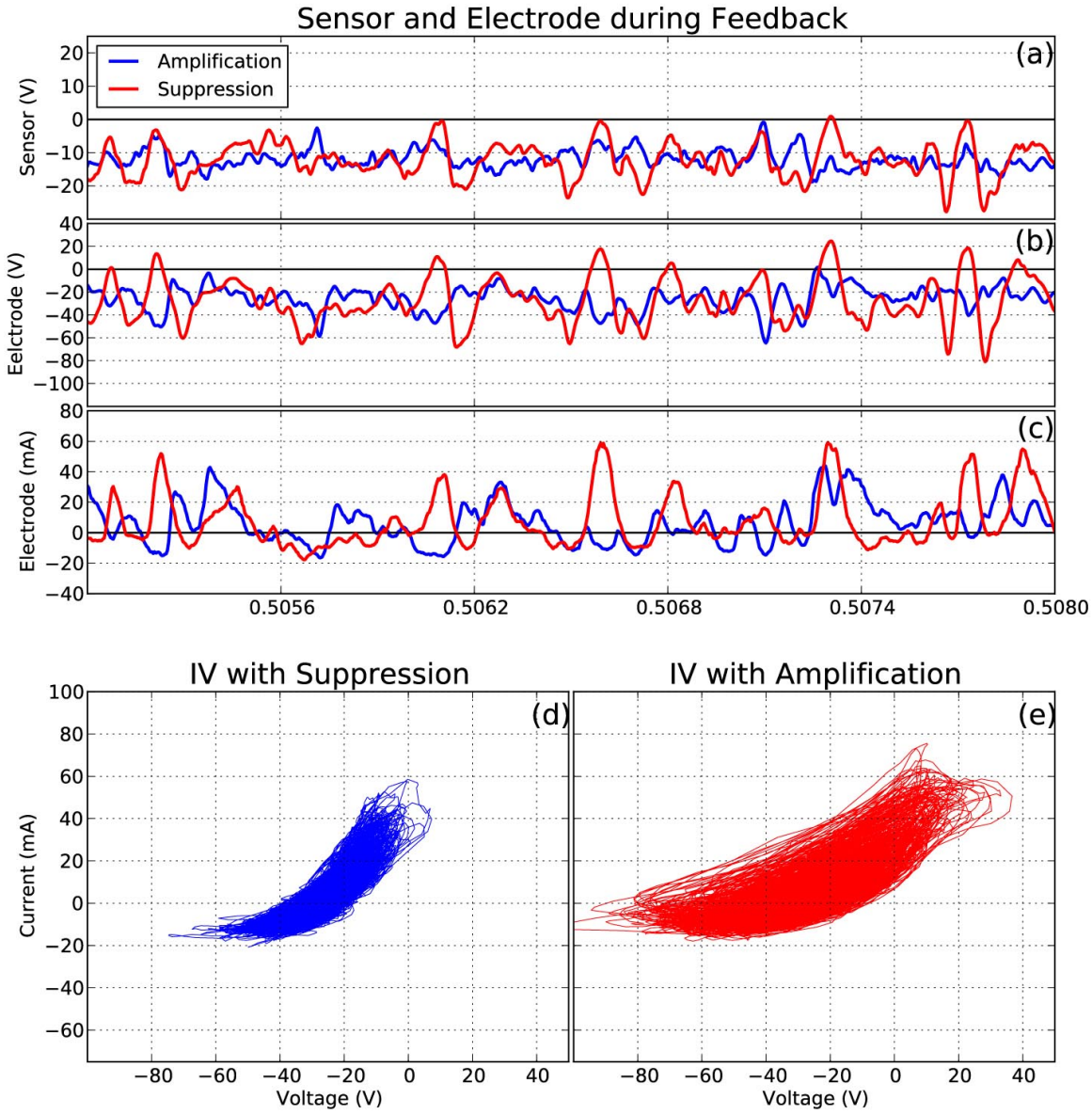

Figure 4.6: The sensor voltage (a), electrode voltage (b) and current (c) during feedback which is in phase with the measured fluctuations (red) and 180° out of phase (blue). The lower plots are of the IV characteristics during negative (d) and positive feedback (e). Note that the data shown in the IV plots are from a much longer time period than shown in the three above plots.

From these measurements we make several interesting observations; first, the excursions during positive feedback (in phase) are larger than during negative feedback (180° out of phase). The feedback is amplifying large oscillations in potential. Second, the negative current for both of the cases is limited to the ion saturation current, ~ -15 mA for this large diameter probe. The positive current is larger for the amplifying feedback as the voltage swing more positively, drawing more electrons. Third, for both cases, the IV traces are dominantly in the first and third quadrant, indicating that the power driven by the electrode is on average positive. These first three topics will be explored more in a later section. Finally, the slope of the characteristic, while admittedly broad, does appear to change between positive and negative feedback. This will not be explored in this thesis.

By implementing a triggering circuit, the signal to the electrode could be rapidly (20 μs) turned on and off. This circuit is described in Appendix G. This allowed for same-shot comparison of the turbulent fluctuations with and without feedback. Figure 4.7(a) shows the RMS fluctuations of the sensor signal with amplifying (red) and suppressing (blue) feedback triggered on and off multiple times for 18 ms intervals. (b) shows 18 of these triggering events averaged at 50% transparency, with a smoothed signal indicating a 30% reduction or amplification in the measured fluctuation level. (c) shows the same data in (b) for the time near the "off" trigger, and we observe the plasma to respond as fast or faster than the trigger switching time. These shots were taken using the 12° configuration depicted in Figure 4.5.

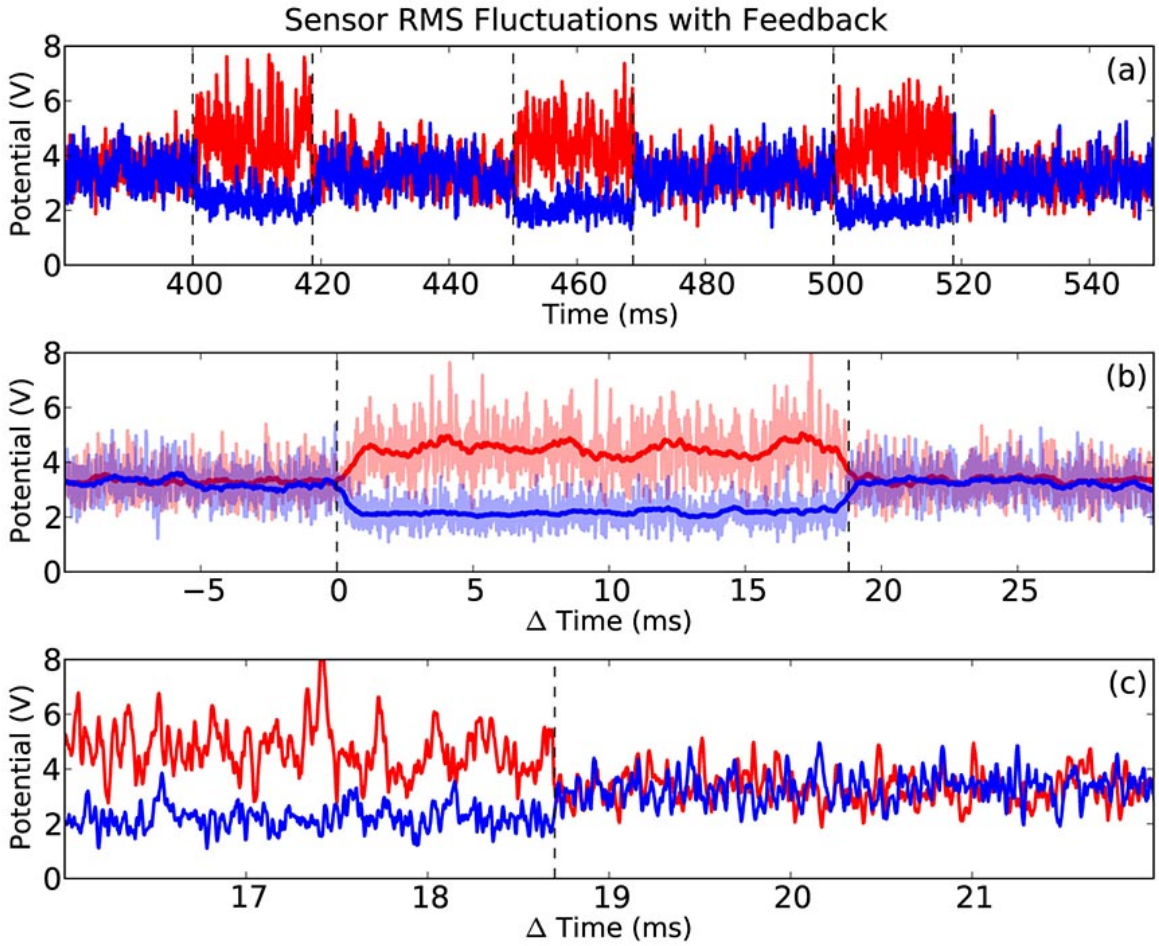

Figure 4.7: Triggering events as measured by the sensor. a) RMS, raw. b) Averaged over 18 triggering events. c) Zoom in of the trigger off time.

4.3 Phase Scan

In the previous section we observed changes in fluctuation amplitude during positive and negative feedback. These observations were made in the time domain, but we can also look in the frequency domain to study how feedback changes the turbulent spectrum. Figure 4.8 displays the changes in spectral intensity [58] as measured by the sensor when feedback is applied. The black curve is the "natural" spectrum measured without feedback, red is the spectrum with positive feedback and blue is with negative feedback.

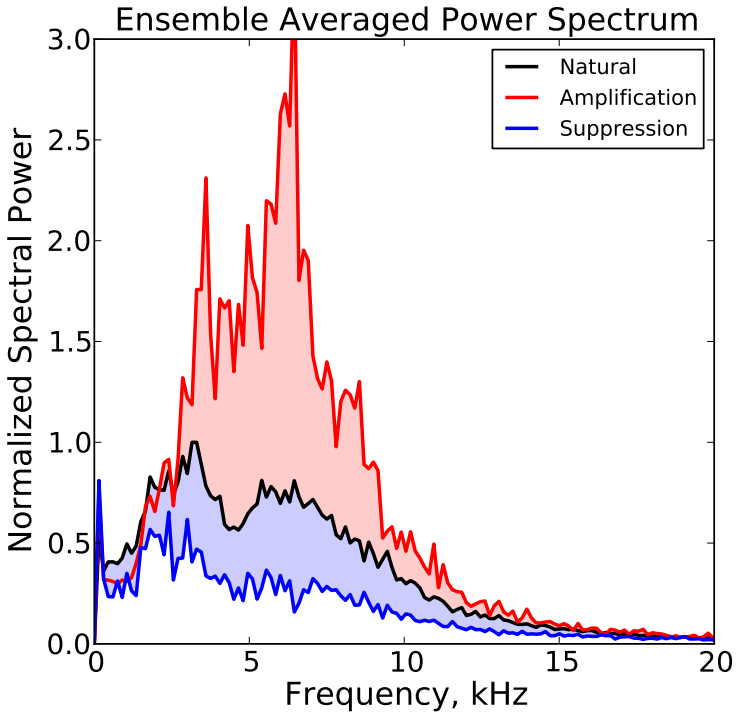

Figure 4.8: Spectra measured by the sensor without feedback (black), with positive feedback (red) and negative feedback (blue). Feedback results in significant changes to the turbulent spectrum.

The spectra in this thesis are calculated in a ensemble, or Welch [59], manner. Here, a signal is broken into many realizations each several correlation times long. The power spectrum of these realizations are averaged to reveal the stationary spectrum of the turbulent fluctuations [58]. All spectra reported here are composed of 60-80 realizations of a signal. The "natural" spectra are additionally ensemble averaged over several shots, therefore generally contain more than 300

realizations of plasma turbulence. This averaging allow us to determine the influence of feedback in a statistically meaningful manner. We can consider the variation of the ensemble spectrum by looking at the standard deviation with frequency from shots taken without feedback. Figure 4.9 (top) shows the same data plotted in Figure 4.8, with the standard deviation with frequency plotted over the natural spectrum. We see the effects of feedback are significant over this variation.

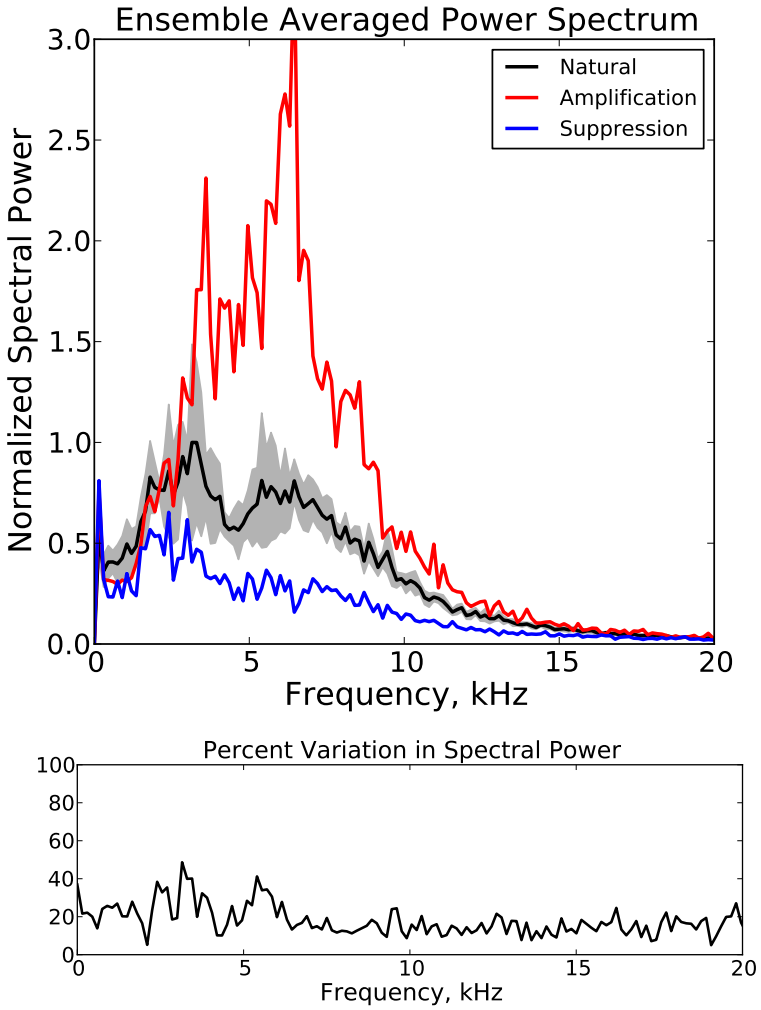

Figure 4.9: Top, standard deviation with frequency plotted about the natural spectrum to display the variation in spectral content on a shot to shot basis. Bottom, percent variation in the spectrum. An average variation of 18% is assumed for all spectra in this document.

From this we find the percent variation in spectrum with frequency as the standard derivation divided by the average spectrum. This is plotted in the lower portion of Figure 4.9, and yields an average variation of 18%. This will be assumed for the rest of the spectra shown in this thesis.

The two cases of feedback reported above (red and blue) are two particular phase settings which were found to result in peak amplification and peak suppression of the turbulent spectrum. These phases are set by varying the resistor settings in the feedback circuit describe in Chapter 3, which varies the applied phase shift. By performing scans of phase over multiple shots, we observe the effect of feedback at a given phase by comparing the spectrum with feedback to the natural spectrum.

Figure 4.10 shows in blue the sensor spectrum from shots taken using the 12° configuration (shown in Figure 4.5) as the phase is varied. In black is the natural spectrum. It should be noted that the resistor settings were chosen in increments of 45° for a 3 kHz signal, but the true phase shift varies with frequency, as is shown by the cross-phase of the sensor and electrode plotted in the lower portion of Figure 4.10 in green.

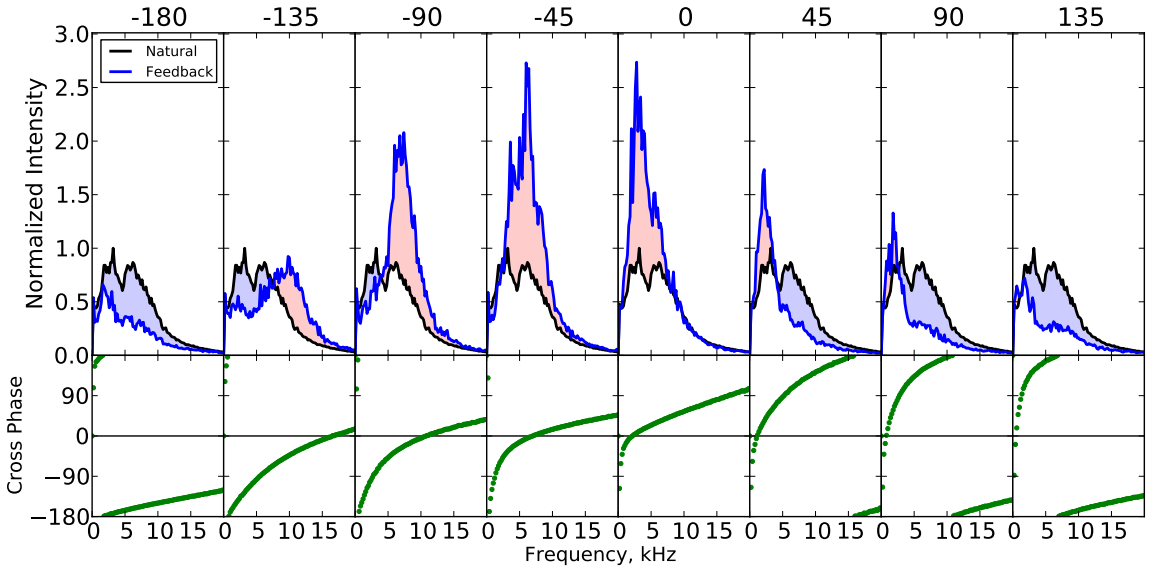

Figure 4.10: Phase scan using the 12° separation configuration.

We observe that for some phase shifts there is suppression of the turbulent spectrum, while other phases result in amplification. Notice that the spectrum is suppressed for frequencies where the phase approaches 180°, and is amplified for phases closer to 0°. This results in a shifting of the amplified frequencies as the phase is adjusted, dominantly between 1-10 kHz.

We summarize the results of this phase scan in two ways. First, by band integrating the spectra

with feedback (P_{FB}), and normalizing by the same integral of the natural spectrum (P),

$$I = \frac{\int_1^{10} P_{FB}(\omega)d\omega}{\int_1^{10} P(\omega)d\omega} \tag{4.1}$$

we find the frequency integrated intensity I. Figure 4.11 (a) plots this quantity with phase, and we see a maximum in amplification near 0° and a minimum near 180°. Similarly, we can find the frequency weighted frequency averaged quantity F,

$$F = \frac{\int_1^{10} \omega P_{FB}(\omega)d\omega}{\int_1^{10} \omega P(\omega)d\omega} \tag{4.2}$$

which is plotted in Figure 4.11 (b). We observe that the dominant mode frequency changes as we apply feedback, increased for some phase shifts and reduced for others. Error is computed as the standard deviation of these integrated quantities from shots taken without feedback.

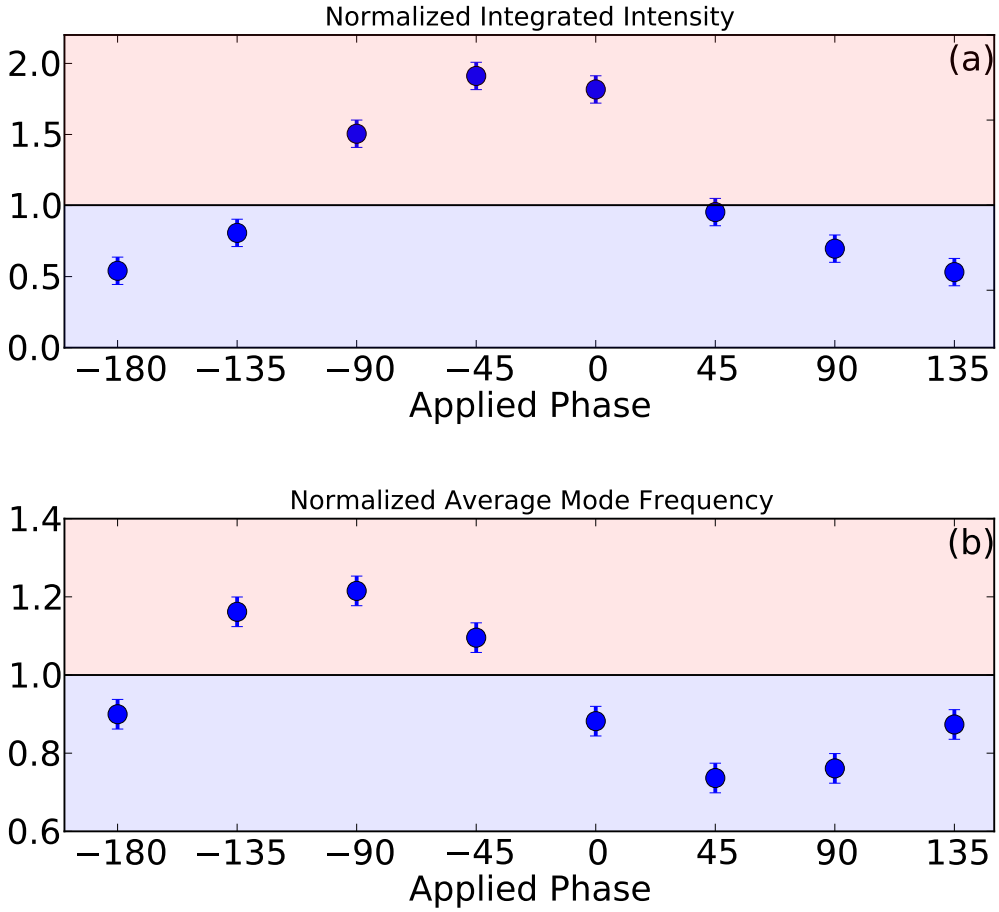

Figure 4.11: Frequency integrated intensity (a) and frequency integrated, frequency weighted intensity (b) with applied phase.

4.4 Gain Scan

Gain scans were performed initially to find the operational limits of the feedback circuit, but also demonstrated the effect of reducing the bias and current applied to the plasma. We begin by discussing the technical limitation imposed by the amplifiers used.

The power amplifier used (HP 6827A) has a range of $\pm 100V$ and 500 mA, which bounded the gain we could apply. Looking at the cross-coherence between the sensor and electrode voltage signals indicated how accurately the output followed the input. Figure 4.12 shows the cross-coherence (upper plots) and cross-phase (lower plots) as the gain is varied from $-6 \rightarrow 6$. Positive and negative gains are achieved by setting the phases to peak amplification and peak suppression. In blue are the cross-coherence and cross-phase between the sensor voltage and the electrode voltage, and green between the sensor voltage and electrode current.

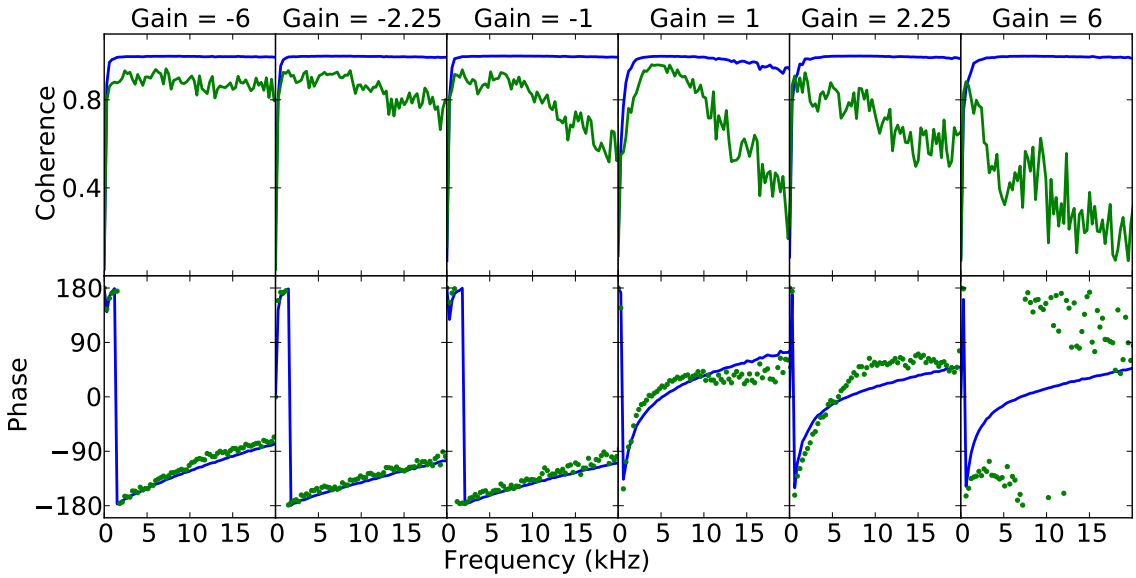

Figure 4.12: Coherence and cross phase between sensor voltage and electrode voltage (blue), and sensor voltage and electrode current (green) with increasing gain. As the gain is increased too high with amplifying feedback, the power supply limits begin to have an effect.

While the output voltage remained coherent to the input for all gain setting, we found that with gain larger than 4 the coherence of the driven current is significantly reduced. To maintain a coherent output current, a gain of 4 was used for all of the experiments reported here (excluding the

gain scan about to be discussed). Notice that the large negative gains remained coherent. Likely, the power supply limits were being exceeded during amplifying feedback.

With the limits of the feedback established, we performed scans in the operational range of the system to observe how feedback is effected by gain. Figure 4.13(a) shows the sensor spectrum as the gain is adjusted from $-4 \rightarrow 4$ in blue, with the natural spectrum in black. For amplifying feedback we see that a significant amount of gain is needed (~ 3) to start seeing changes in the spectrum, while suppressing feedback requires less. Increasing the gain in both cases resulted in a stronger ability to effect the turbulent spectrum. Using Equation 4.1, Figure 4.13(b) plots the frequency integrated intensity from this gain scan. With increased positive gain we see increased intensity, and negative gain results in reduced intensity.

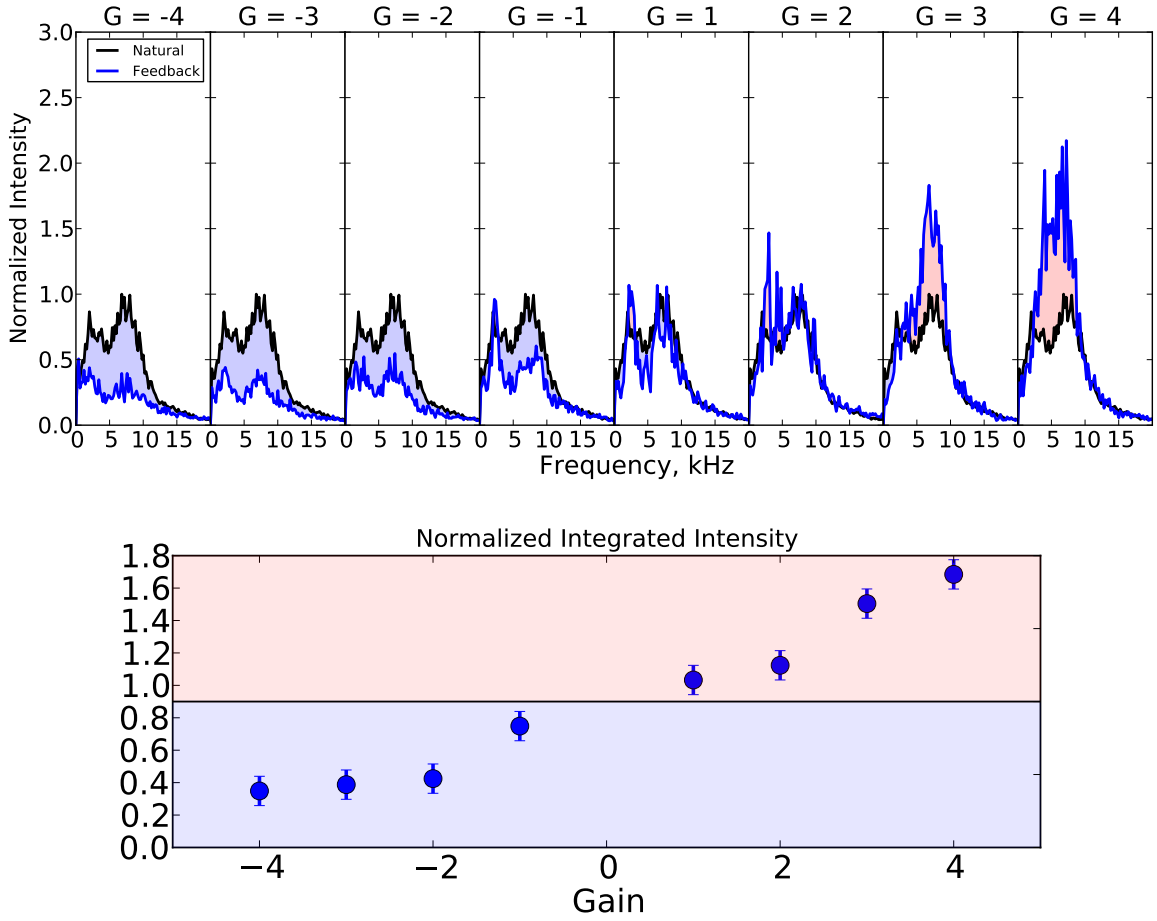

Figure 4.13: Top, measured spectrum as gain is increased from -4 to 4. Bottom, the frequency integrated intensity. Positive gain amplifies the spectrum while negative gain suppresses it.

4.5 Power Flow

We have shown that feedback can be used to amplify and suppress the fluctuations in the plasma. This suggests that the feedback system is adding energy to the fluctuations with positive feedback and removing energy during negative feedback. Hence, the sign of the power flowing into the plasma should change as we vary the applied phase. In Section 4.2 we showed that the electrode bias and current are generally in phase, which would mean the power delivered by the electrode is always positive. How can we reconcile this? The missing component here is the sheath! Figure 4.14 illustrates the circuit we will use as a model:

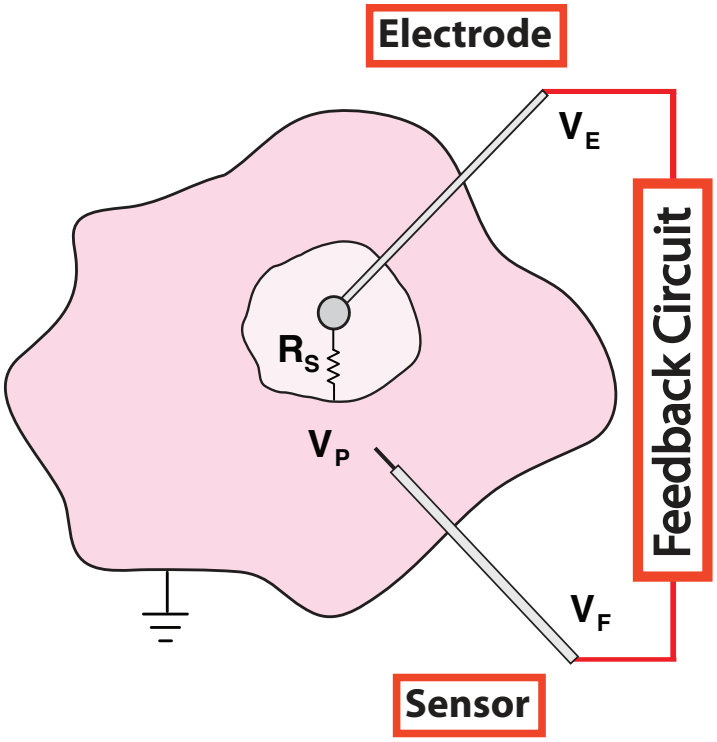

Figure 4.14: Illustration of the circuit model used to describe power flow. The electrode is biased by the fluctuations in floating potential (measured by the sensor) multiplied by a complex gain. A current is driven across the resistive sheath (not to scale) in proportion to the voltage difference $V_E - V_P$.

Figure 4.14, with a greatly exaggerated sheath, displays that there are three voltages to consider. The plasma has a fluctuating potential relative to ground, V_P, and the sensor measures this as the floating potential V_F. This floating potential is then filtered, amplified and applied to the electrode.

This electrode then either injects or collects current across the sheath depending on the bias relative to the plasma potential.

This is a very complicated process, so we simplify things with a few assumptions; first, as the signal measured by the sensor is high-pass filtered, the sensor signal is only the fluctuating part of the floating potential. We will approximate this as the fluctuations in the plasma potential, so $\tilde{V}_F \approx \tilde{V}_P$ and the bias to the electrode is given as $\tilde{V}_E = |G|e^{i\theta}\tilde{V}_P$. As the electrode is capacitively coupled to the plasma, we assume that it "floats" to the DC floating potential. This means the feedback is applied to the plasma about the floating potential of the electrode. Next, the difference between the electrode bias and the plasma drives a current across the sheath. As mentioned above, this current is in phase with the electrode bias, but not necessarily the plasma potential. From the feedforward tests performed in Section 4.1, we found that the sheath was resistive, with $R_s \sim 400\ \Omega$ near floating potential. Limiting our analysis to small deviations from V_F, we take the fluctuating current across the sheath as,

$$\tilde{I} = \frac{\tilde{V}_E - \tilde{V}_P}{R_S} = \frac{|G|e^{i\theta}\tilde{V}_P - \tilde{V}_P}{R_S} = (|G|e^{i\theta} - 1)\frac{\tilde{V}_P}{R_S} \tag{4.3}$$

With these definitions we can consider the power of the system. We know the total power injected into the system is the power measured by the electrode, $P_E = I_E V_E$. As mentioned, this power is on average positive, but where is the power going? It takes power to enhance the fluctuations in the plasma, but it also requires power to drive current across the resistive sheath. This means that regardless of the direction of current flow, energy will be dissipated in the sheath, a positive offset in net power. We say the total power is given as:

$$P_{tot} = P_E = P_S + P_P \tag{4.4}$$

where P_S is the power into the sheath and P_P is the power into the plasma fluctuations. The power into the plasma is found as the product of the sensor voltage and the electrode current, $P_P = I_E V_P$, which as mentioned before, can be negative. The power into the sheath is therefore the

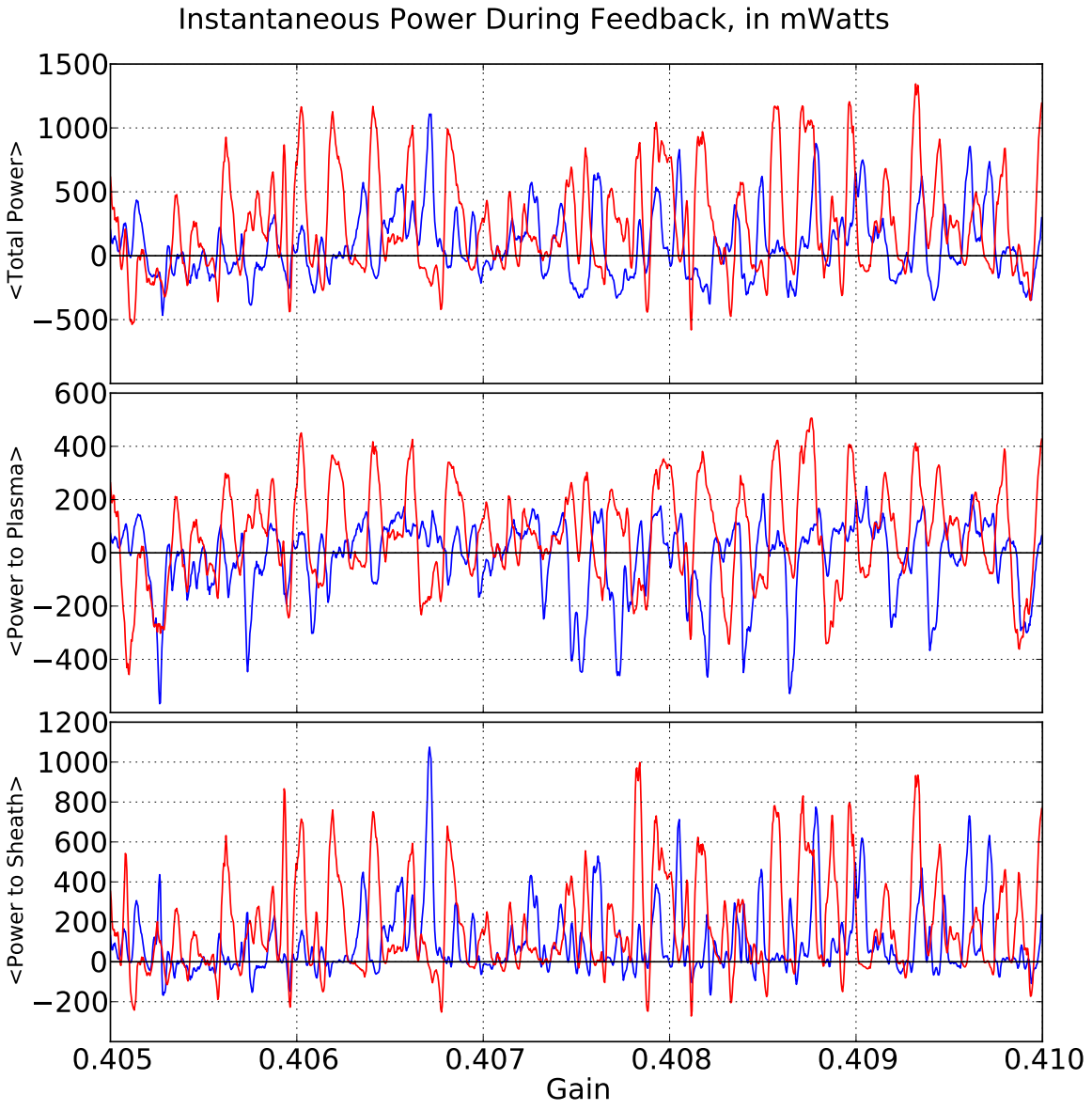

Figure 4.15: An example of the instantaneous power of the electrode, into the plasma and into the sheath.

difference between the total power and the power into the plasma, $P_S = P_E - P_P$. Figure 4.15 plots these three powers for a window of time during positive (red) and negative (blue) feedback. From the traces, we can see that the power into the sheath is on average positive for both cases, while the power into the plasma changes sign as the phase is changed. Figure 4.16 plots the time averages of these three powers with positive (G = 4) and negative (G = -4) feedback. We see that the total power and the power into the sheath are positive for both cases, while the power into the plasma reverses sign during negative feedback. This indicates that the plasma is putting power into the sheath, and this energy is coming from the fluctuations. During positive feedback the plasma is acting like a load, and during negative feedback the plasma acts like a generator. Figure 4.17 illustrates these two cases, where the voltage power supplies on the left hand side represent the plasma.

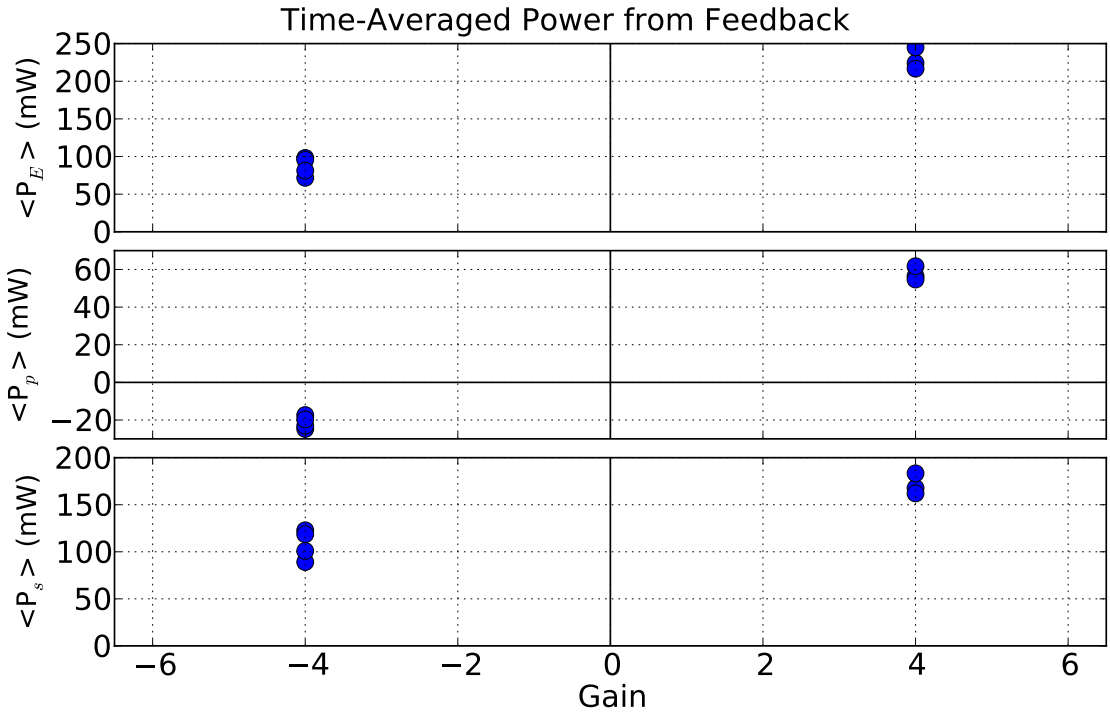

Figure 4.16: Time averaged power for positive feedback (Gain = 4) and negative feedback (Gain = -4). The total power and power into the sheath are positive for both cases. The reversal of the sign of power into the plasma indicates the plasma acting as a load during positive feedback and a generator during negative feedback.

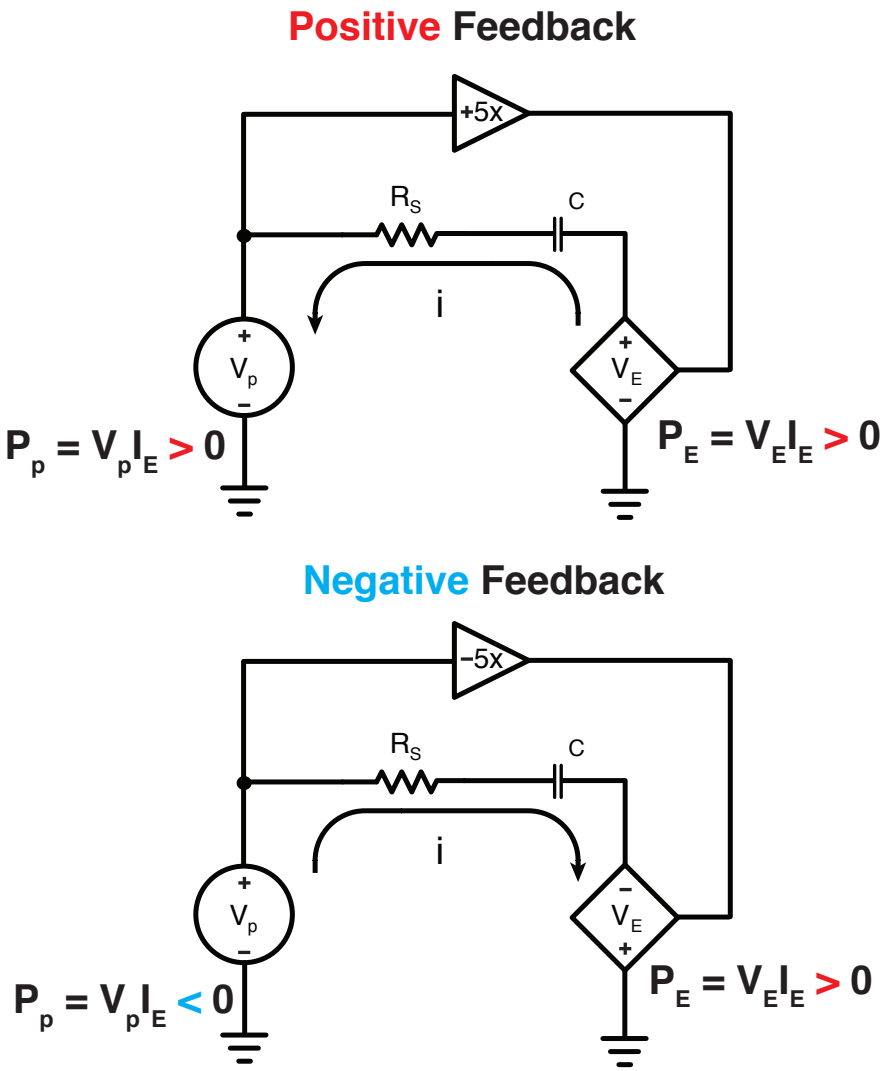

Figure 4.17: A cartoon of the simplified circuit diagram representing the coupled plasma-feedback system during positive and negative feedback. The plasma is represented as a voltage source which can act as a load or a generator, depending on the phase of the feedback.

Using this definition of power into the plasma, we can view the alteration of the feedback circuit gain as an adjustment in the admittance of the circuit. Due to the frequency dependence of the circuit, we define this admittance in the frequency domain as,

$$Y(\omega) = \frac{V_P^*(\omega) I(\omega)}{|V_P(\omega)|^2} \tag{4.5}$$

where $V_P(\omega)$ is the Fourier transform of the sensor signal and $I(\omega)$ is the Fourier transform of the current measured to the electrode. The real part of this admittance is the conductance in the frequency domain. Figure 4.18 (a) shows the spectral intensity from the gain scan of Section 4.4, and (b) shows the associated conductance with frequency. We observe that when the conductance is negative, the turbulence is suppressed, and when the conductance is positive, there is amplification of the fluctuations.

Figure 4.18 (c) summarizes changes to the intensity (blue) and conductance (red), frequency integrated in the band from 1→10 kHz (Equation 4.1). The increased turbulence intensity is clearly related to the conductance of the circuit controlling current collection. The average power injected into or extracted from the turbulence is equal to the product of the turbulent fluctuations ($\langle |V_P|^2 \rangle$) and the conductance, about 72 mW and 12 mW, respectively. This is in good agreement with the values plotted in Figure 4.16.

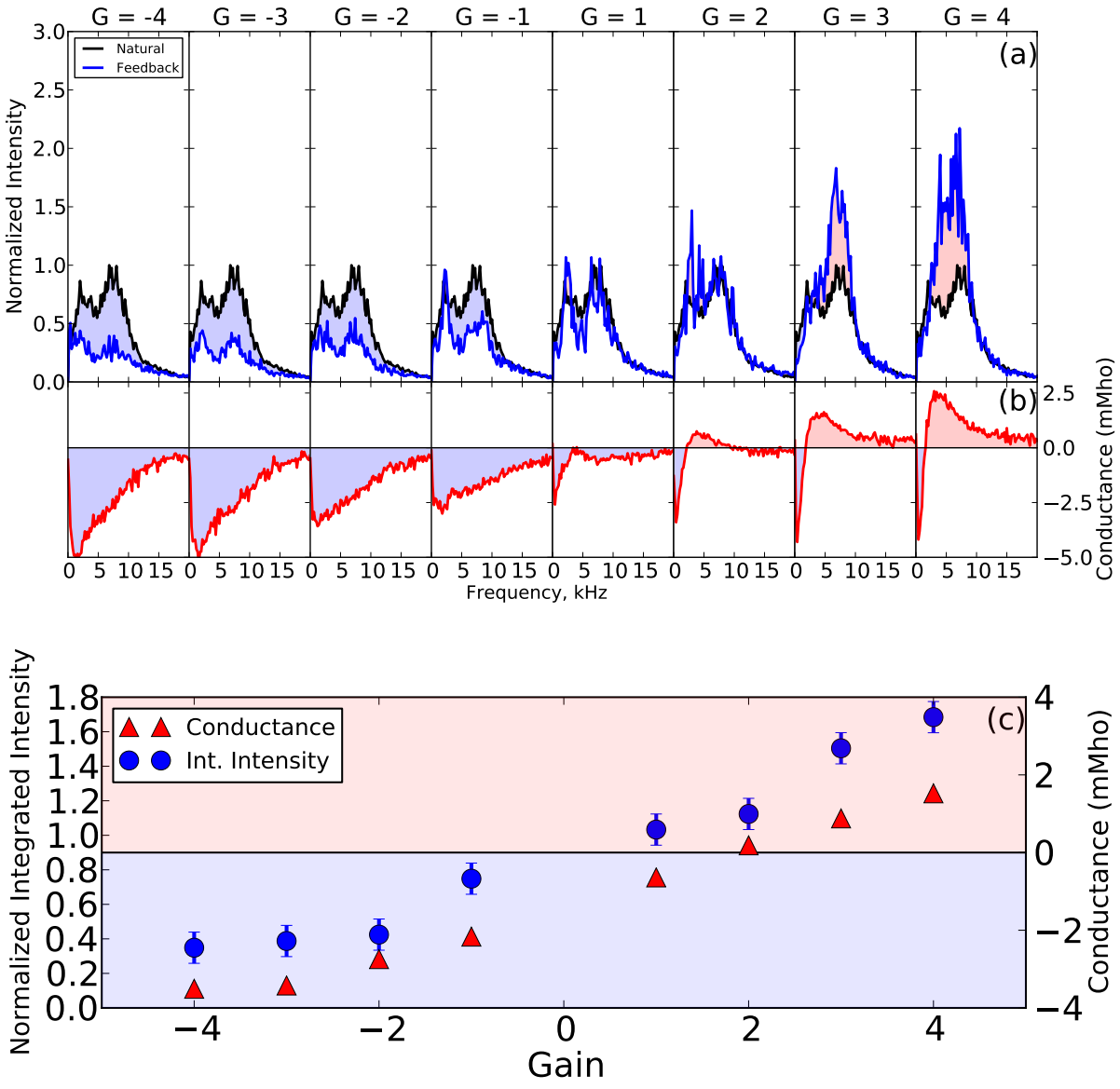

Figure 4.18: Intensity (a) and conductance (b) with frequency, and the band integration of the two (c) indicate that positive conductance leads to amplification of the fluctuations, while negative results in suppression.

4.6 Observations of Feedback with Azimuthal Angle

As we observed in the open-loop tests, the influence of an input signal in the plasma is limited in range azimuthally as the oscillations decorrelate. A similar range of influence is observed with the application of feedback. The changes in RMS fluctuation, correlation and spectral content are measured at various azimuthal separations from the electrode as feedback is applied. Figure 4.19 shows the experimental configuration with the relevant floating potential probes and polar imager azimuthal array highlighted.

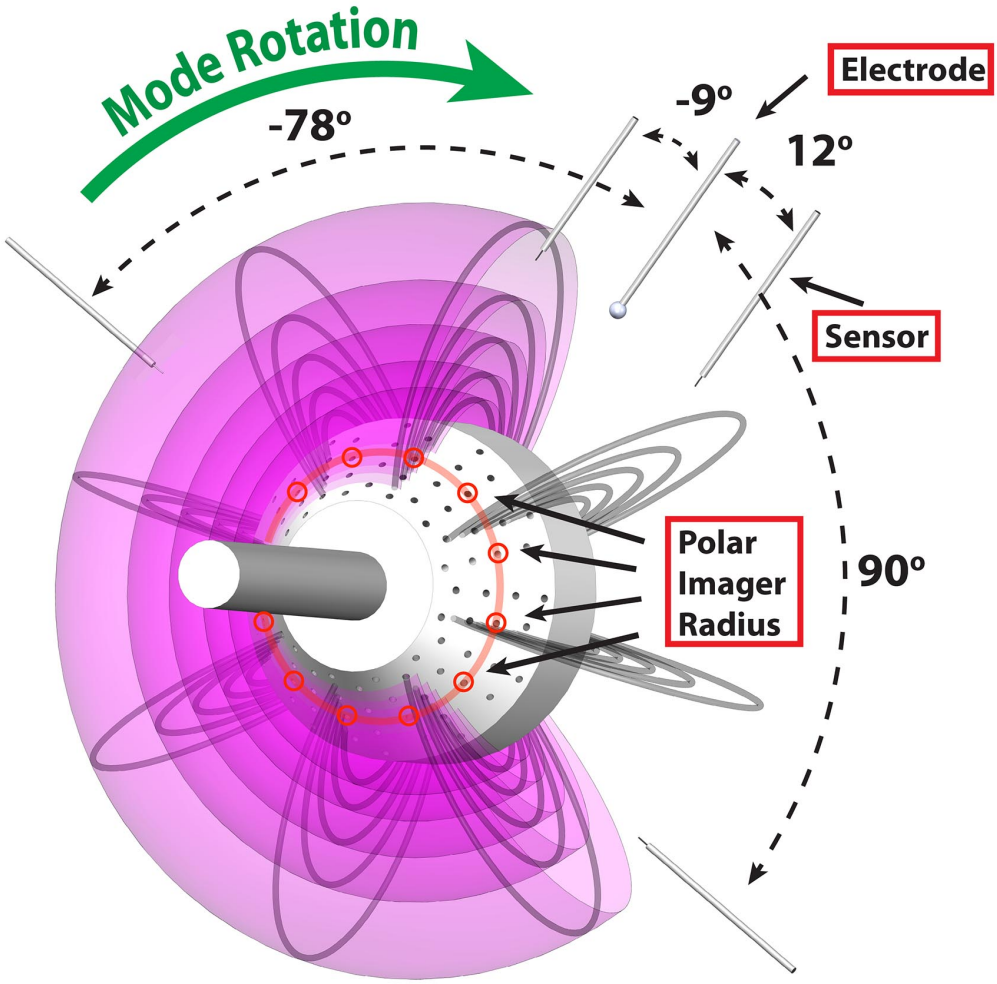

Figure 4.19: Experimental configuration for measuring influence of feedback with azimuth. Notice here the sensor is a floating potential probe located 12° downstream from the electrode. The other diagnostics discussed in the analysis are also displayed including the azimuthally separated floating potential probes and polar imager detectors.

Figure 4.20 shows the change in RMS fluctuations as feedback is triggered on and off (similar to Figure 4.7(b)) for the floating potential probes shown in Figure 4.19. We observe the influence of feedback only on probes downstream from the electrode in the direction of mode rotation. The probe upstream from the electrode by 9° shows no noticeable change during triggering events, even though it is closer than the sensor at 12°.

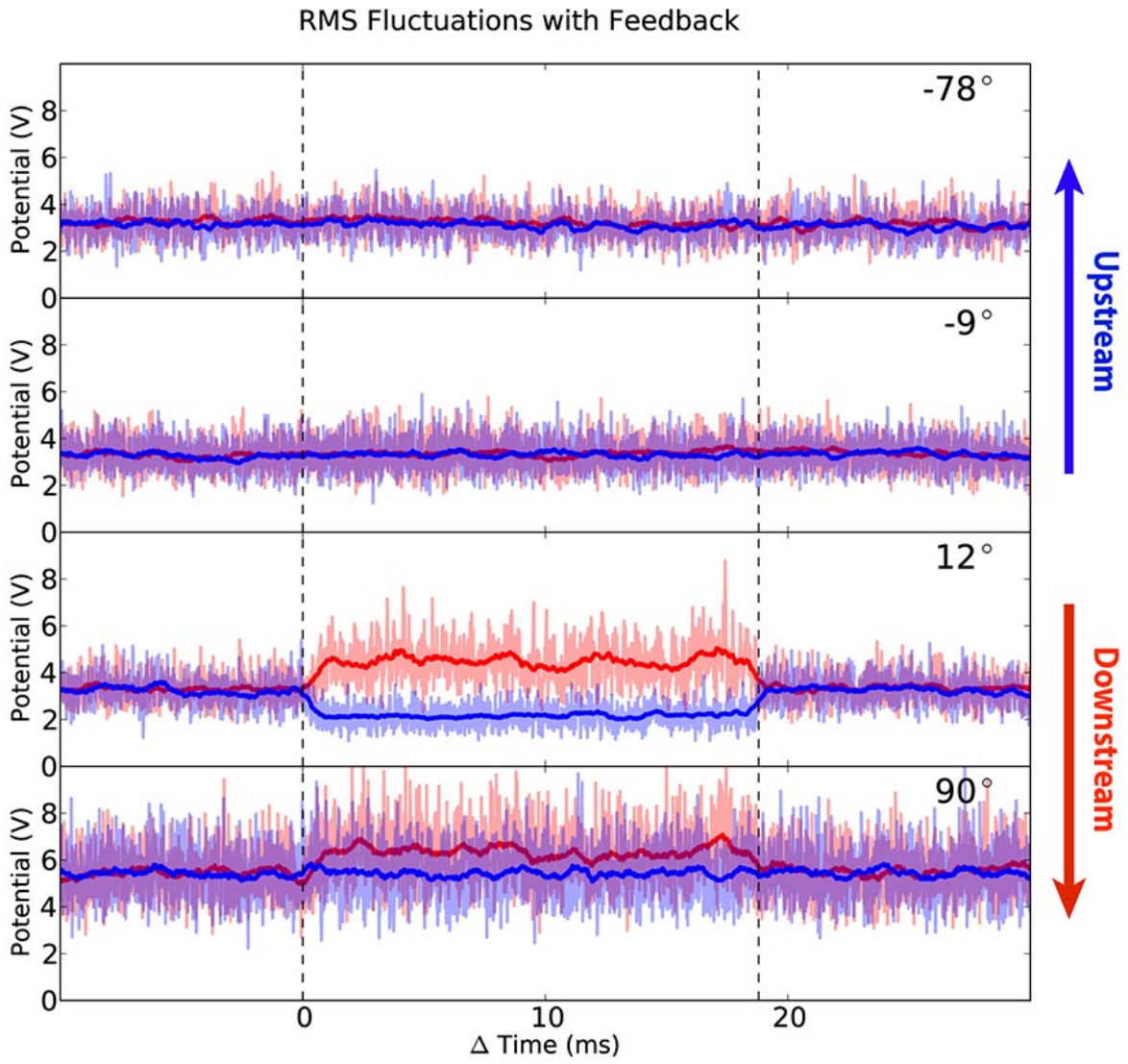

Figure 4.20: Response to triggered feedback measured by floating potential probes at various azimuthal separations from the electrode. The influence of feedback is strongest closer to the electrode in the downstream direction and attenuates with increased separation.

We improve our azimuthal resolution with measurements from the polar imager. Using the detectors at the highlighted radius in Figure 4.19, we observe the change in fluctuations with azimuth when feedback is applied. Figure 4.21 shows the RMS fluctuations normalized to the average levels without feedback (circles) and the same measurement from the floating probes (triangles). The error bars are determined by the variation in the averaged quantity shown in Figure 4.20. In red we show these values for amplifying feedback, in blue for suppressing. We see a 30% increase or reduction in these values near the sensor, attenuating with increasing azimuthal separation from the electrode. Greater than 90° separation, the influence is no longer observable. Upstream from the electrode we see no influence from the feedback.

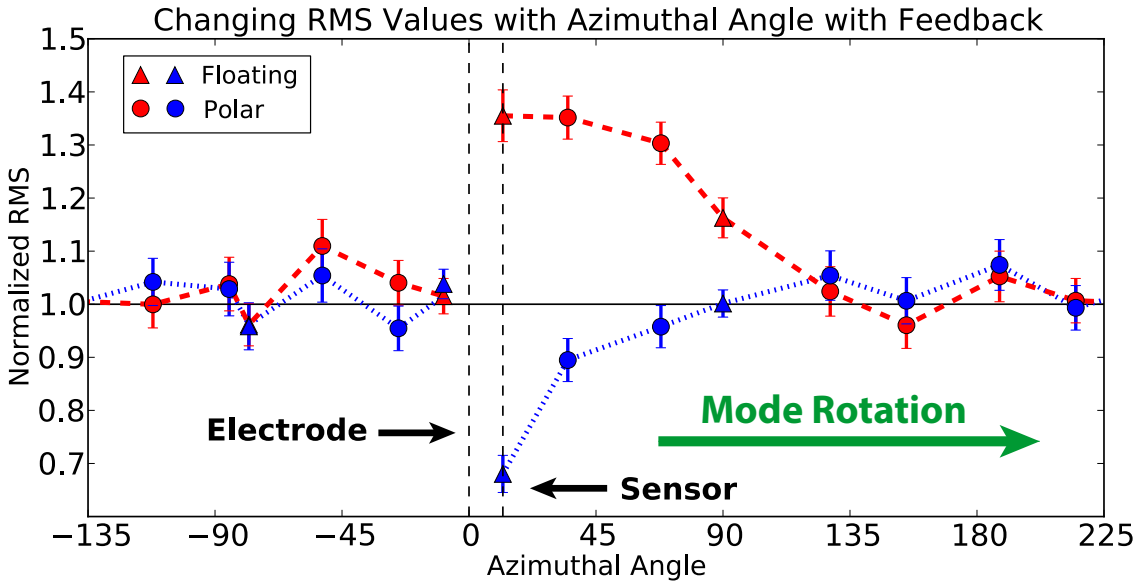

Figure 4.21: The normalized RMS levels from the polar imager detectors (circles) and the floating probes (triangles) for positive (red) and negative (blue) feedback. Each measurement is normalized to its multishot averaged RMS level without feedback. We observe a 30% reduction in RMS levels with suppressing feedback, and a 30% increase with amplifying feedback. This only occurs downstream in the direction of mode rotation, sharply defined after the electrode.

We find that the correlation of the plasma also changes with applied feedback. Cross-correlation [58] between two separated diagnostics gives a measure of the lead/lag time and the decorrelation, which is a measure of organization, or lack thereof, in the plasma. By measuring the cross-correlation of the sensor signal with the various polar imager detectors, we observe the influence of feedback

on the turbulence in the plasma. Figure 4.22 shows the peak correlation between the sensor and a radius of polar imager detectors when positive (red) and negative (blue) feedback is applied compared to the correlation without feedback (black). We see that the downstream correlation is increased for amplifying feedback and reduced for suppressing feedback, a similar trend to that seen in RMS. Positive feedback is creating large amplitude, coherent structures in the plasma, and negative feedback is removing them.

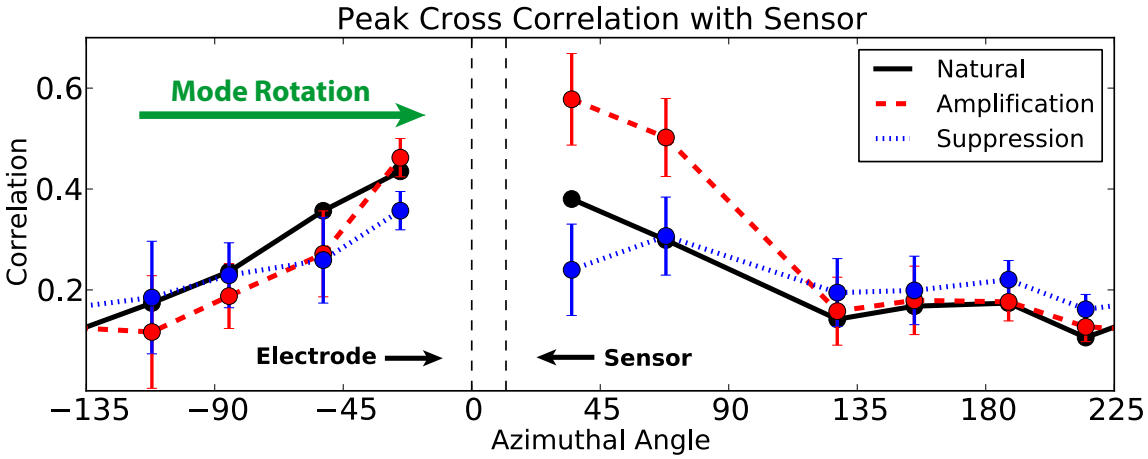

Figure 4.22: The peak coherence between the sensor and various polar imager detectors for amplifying (red), suppressing (blue) feedback, and without feedback (black). Again, the influence of the feedback on coherence is downstream from the electrode.

From both of these azimuthally resolved measurements, there is strong indication that the feedback can only influence the plasma in a range of roughly 90° downstream from the electrode. Comparing this to the correlation length measured in CTX of roughly 50° at this radius [13], the fluctuations driven by the electrode are significantly decorrelated after reaching the more separated diagnostics.

We also observe changes of the spectra measured by the polar imager detectors. In Figure 4.23, the spectrum for each detector on a radius (L = 5, r = 39 cm) is plotted for shots with no feedback (black) and amplifying and suppressing feedback (red and blue, respectively), positioned in the figure relative to their azimuthal location. The polar imager is illustrated in the center and the L = 5 radius is highlighted. The location of the sensor and electrode are indicated pictorially and the

detector's separation from the electrode is labeled in each plot. We see the effects of amplifying and suppressing feedback immediately downstream from the electrode, and the discernible influence attenuates with increased separation.

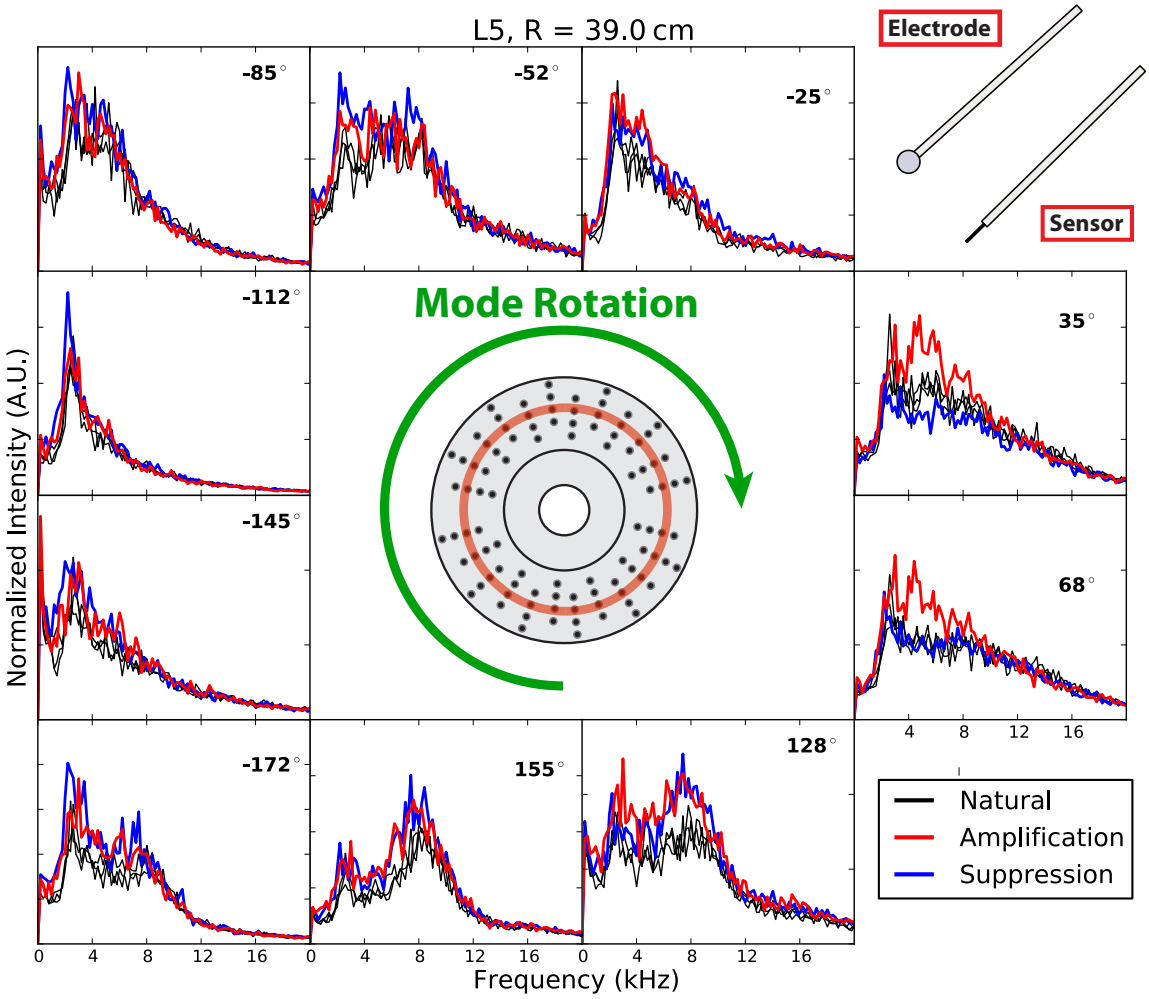

Figure 4.23: The spectrum as measured by the various polar imaging detectors on the L = 5 radius. Black is without feedback, red is amplifying and blue is suppressing feedback. The plots are positioned according to the detector azimuth in the plasma. The influence is observed to attenuate with increased separation.

4.7 Varying the Azimuthal Separation

Observing the influence of increasing azimuthal separation on the effectiveness of feedback, we next explore the effects of sensor-electrode separation. Using the two positions for the sensor and electrode illustrated in Figure 3.11, we perform four phase scans with various azimuthally separated configurations.

Figure 4.24 (a) shows the configuration discussed in the previous sections where the sensor is positioned 12° downstream from the electrode. 4.24 (d) shows the phase scan performed with this configuration. As previously pointed out, the maximum amplification in this configuration occurs near 0° applied phase shift, and peak suppression is obtained closer to 180°.

We perform the same phase scan using the configuration illustrated in 4.24 (b), where the sensor is now 90° downstream from the electrode. Figure 4.24 (e) displays a similar trend to 4.24 (d), but the phases of peak amplification and suppression are shifted by approximately 90°. In addition, the relative amount of amplification and suppression are reduced. The azimuthal separation affects the phasing of the feedback while decorrelation of the signal in transit reduces the effectiveness.

By reversing the magnetic field direction, we reverse the direction of mode rotation. This increases the effective separation between the azimuthally fixed sensor and electrode used in 4.24 (e) from 90° to 270° (4.24 (c)). In 4.24(f), the red curves show the results from a phase scan performed using this 270° configuration. We observe almost no change in the spectrum measured by the sensor. If we use an electrode 90° upstream in this reversed field configuration (blue electrode in 4.24 (c)), a phase scan yields the result shown in blue, where a trend similar to that seen in the 90° configuration of 4.24 (e) is seen.

The trend with phase is clearly related to the sensor-electrode separation. If we assume only an m = 1 mode structure in these plasmas, the phase of maximum amplification is such that it compensates for the phase shift produced by the azimuthal separation of a mode rotating between the sensor and electrode. If the separation is too large, the effects of the feedback are attenuated significantly and so spatially imposed phase shifts larger than 90° are not observed.

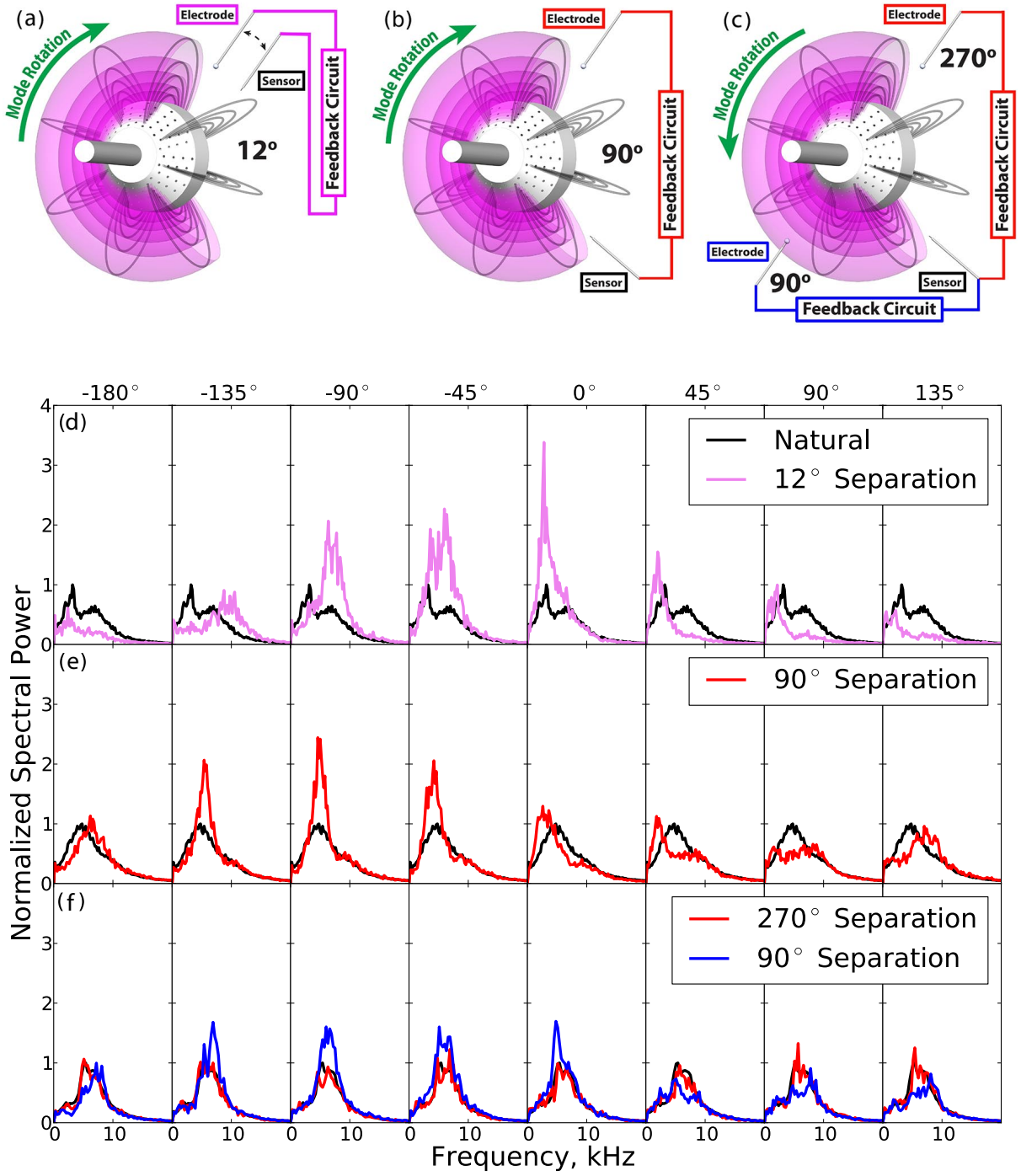

Figure 4.24: (a-c) show various sensor-electrode configurations with the direction of mode rotation and azimuthal separation indicated. (d-f) show a comparison of phase scans performed with the various configurations. The trend shifts with the azimuthal separation as long as the separation is small enough that the effects of feedback are not attenuated significantly.

4.8 Zero Net Injected Current

In the feedback experiments described so far, the circuit has been assumed to complete through the plasma to ground, most likely to the vacuum chamber wall. Alternatively, the circuit could be completed by collecting the injected current on another electrode located elsewhere in the plasma. To study the difference between these two cases, the two configurations illustrated in Figure 4.25 were used to perform phase scans.

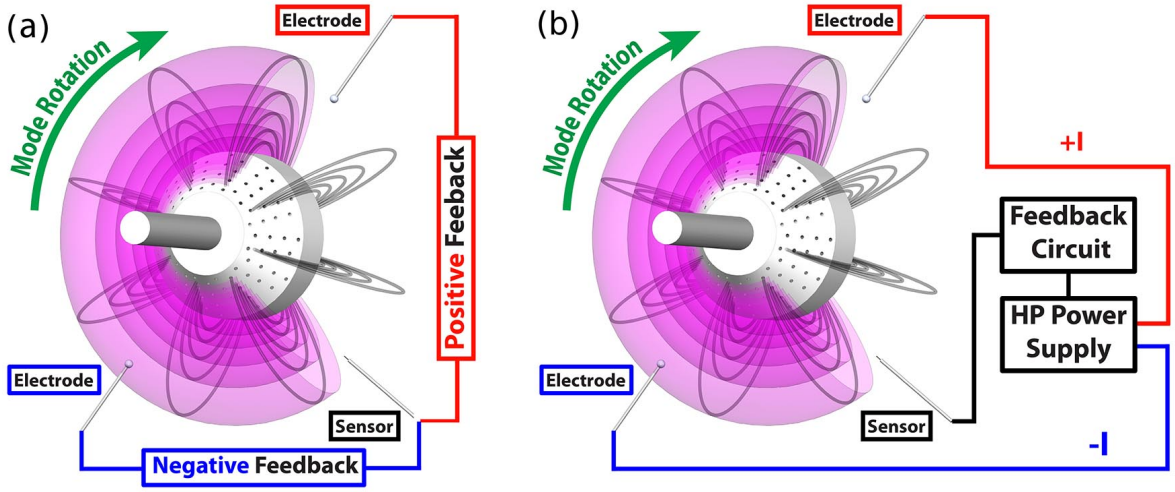

Figure 4.25: a) Two independent feedback systems driven by one sensor apply oppositely phased feedback, pulling nearly opposite currents. b) One system is driven by the sensor and two electrodes are coupled to the outputs of the amplifier. The current through the electrodes is equal and opposite, and the circuit completes through the electrodes.

Figure 4.25 (a) shows a configuration where two independent systems connected to the same sensor apply feedback that is 180° out of phase. Here, two amplifiers are used, and for each, the circuit is completed through ground. The electrodes are separated by 180° azimuthally, with the sensor directly between (90° upstream and downstream). Effectively, whenever one electrode is drawing positive current, the other draws negative current. These circuits complete through the chamber wall, though technically the current injected by one could be collected by the other.

Figure 4.25 (b) shows a configuration where one feedback system is driven by the sensor, but the amplifier is coupled to two electrodes to draw a zero net current from the plasma. So any current that goes into one electrode must be drawn out of the other. In this manner, we force the feedback

system to complete between the electrodes. An isolation transformer was required to decouple the power supplied from ground. Details on this are provided in Appendix G.

Figure 4.26 shows the phase scans performed using these two configurations, the "two system" test on top and the "zero net current" test on the bottom. We observe similar trends in amplification and suppression in each case, suggesting that the "path of completion" isn't a factor in the nature of the feedback. Due to the large separation, it is possible that the circuit in the second case does in fact pass through the wall. A future experiment with a close proximity pairing of two electrode would be an interesting test.

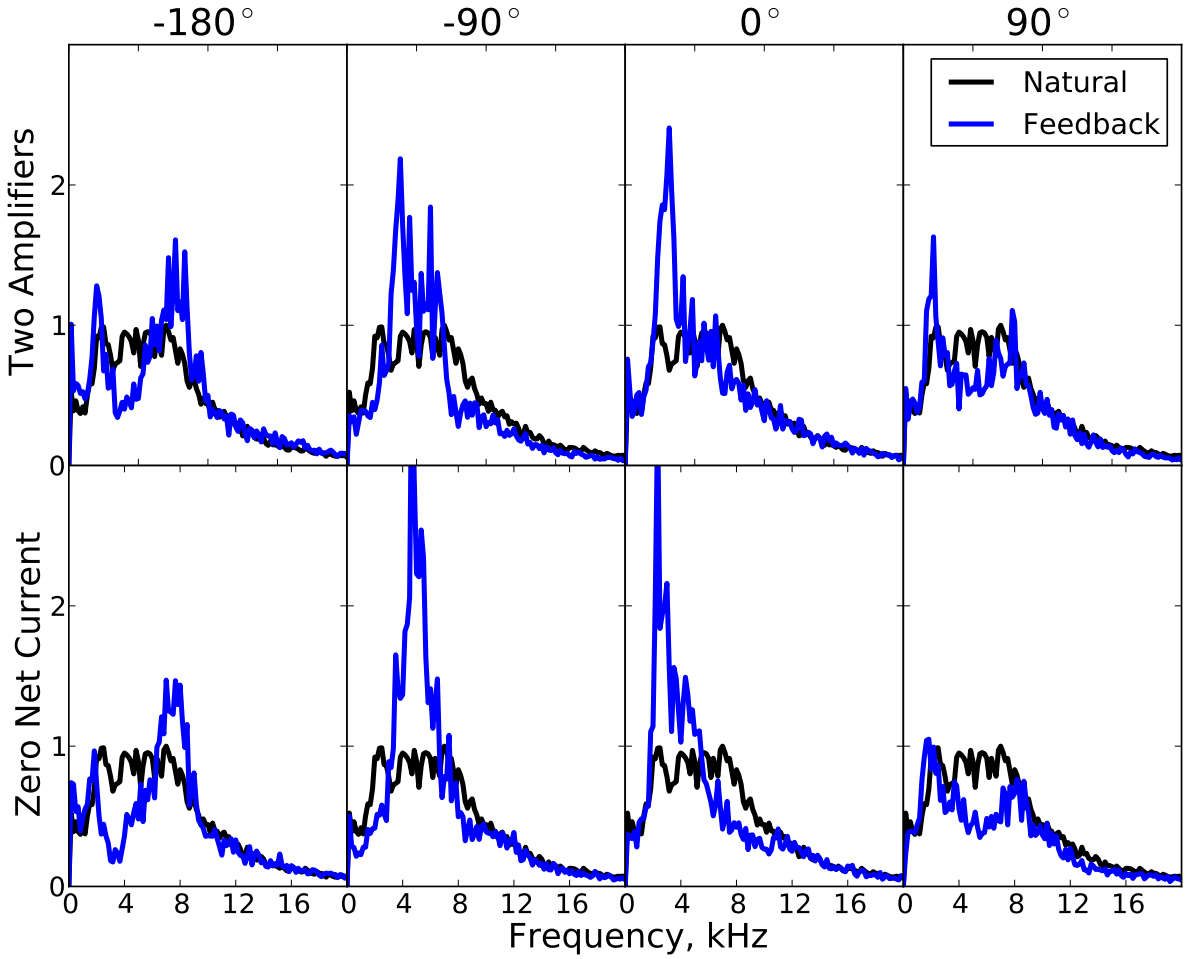

Figure 4.26: Phase scans performed using the two configurations of Figure 4.25. The similar response suggests that whether the circuit completes through the chamber wall or through another electrode does not effect the plasma response to feedback.

4.9 High-Pass Filtered Feedback

Two dimensional turbulence theory predicts a process known as the "Inverse Energy Cascade" [58], where small structures aggregate into larger structures and energy is transferred from small to large scales. This is in contrast to the direction of energy transfer observed in three dimensional turbulent systems. Due to the rapid bounce motion of the electrons, we often discuss dipole plasma dynamics as a two dimensional system. Grierson suggested the presence of this inverse energy cascade in CTX [13], and the work of Worstell involved applying static biases to drive the cascade [53].

If higher frequencies correspond to smaller scale structures, as suggested in [50], then exciting higher frequency modes would inject energy at large k and we could actively drive the inverse energy cascade. We attempt this idea by high-pass filtering the applied feedback. Simply varying the resistor values used in the existing high-pass filter (used to remove < 120 Hz dynamics) we can effectively only apply feedback to the high frequency portion of the spectrum.

Figure 4.27 shows the response to feedback applied with the standard 120 Hz filter (a), a filter with 5 kHz corner frequency, (b), and a 10 kHz corner frequency (c). Note that due to the modified transfer functions, the applied phases weren't exactly the same, but similar to within 20° for the passband of interest. Also note that the increased dynamics at 3 kHz for the high-pass tests was due to differing vacuum conditions, not the adjusted filter (as is seen from the "natural" spectrum in black).

We find that the ability to amplify the spectrum at frequencies below 5 kHz is significantly reduced with filtering, increasingly so for the 10 kHz. We do still see a strong influence of the suppressing feedback above 4 kHz, but as was shown in Section 4.4, less gain is required for suppression than amplification.

From the inverse energy cascade, we would expect that injecting energy at high frequencies would result in increased spectral power at low frequencies. Hence, applying amplifying feedback at 10 kHz and above, we might expect the spectrum to be enhanced at low frequencies as well. From Figure 4.27(b-c), when we apply filtered feedback we see no excitation of the low frequency spectrum. This suggests that the inverse energy cascade, if present, is not excited by feedback.

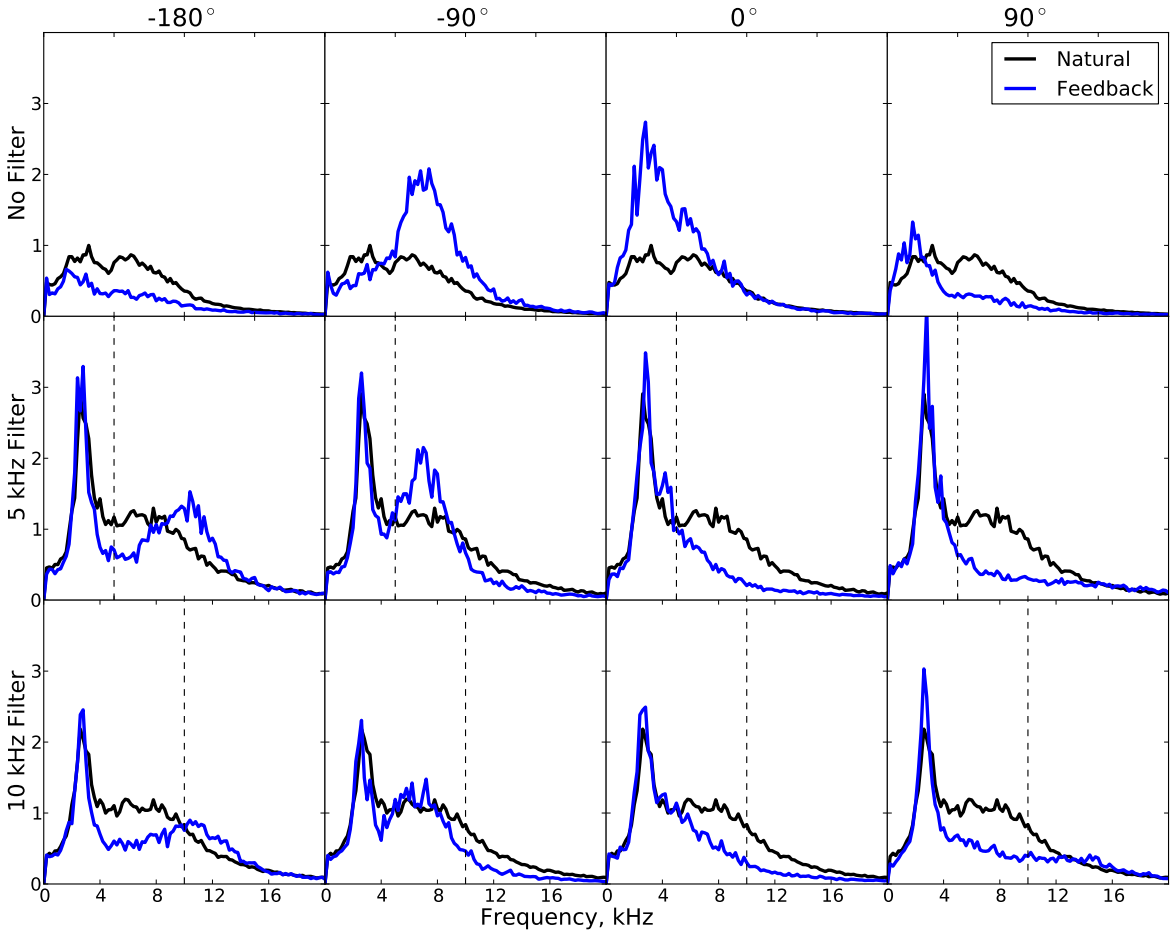

Figure 4.27: Phase scans performed with high-pass filtered feedback. Dashed lines indicate the corner frequencies of the high-pass filters. Excitation of higher frequencies does not appear to drive the inverse energy cascade.

Chapter 5

Gyro-Fluid Model

This section describes the equations used to model the plasma behavior. Previously, both an MHD and two-fluid approach have been used to explain the curvature and centrifugal interchange instabilities [46] in CTX plasmas. A gyro-fluid model is employed to include effects related to entropy modes [60, 61]. The initial equations are first described, then are transformed to flux-tube averaged dipole coordinates. Approximations are made to linearize these equations, then the numerical solve is discussed. Finally, the results are compared to the experimental measurements.

The assumption of $\beta << 1$ allows us to neglect perturbations to the background magnetic field by the relatively small plasma currents. As described in Chapter 2, we use the coordinates of a ideal dipole field described in terms of (ψ, χ, φ),

$$\psi = \frac{M}{r}\sin^2\theta, \qquad \chi = \frac{M}{r^2}\cos\theta, \qquad \vec{B} = \nabla\varphi \times \nabla\psi = \nabla\chi$$

Additionally, when the parallel dynamics are significantly faster than the dynamics of interest, integration over the χ coordinate can be used to reduce the dimensionality of the problem, studying only the cross-field interchange dynamics. We define the flux-tube average of a quantity A as:

$$< A >\equiv \frac{1}{\delta V}\int_{-\infty}^{+\infty}\frac{d\chi A}{B^2} \tag{5.1}$$

A derivation of these coordinates and this integral is provided in Appendix B.

5.1 Building the Model: Gyro-Fluid Equations

We start with the gyro-fluid equations derived by Ricci for a Z-pinch configuration [62]. These equations come from evaluating moments of the gyro-kinetic equations with $\beta << 1$ and assuming Maxwellian equilibrium distribution functions. Additionally, assuming $T_e >> T_i$ and $J_\parallel = 0$, we arrive at the simplified set of equations in a dipole:

$$\text{Force balance:} \quad nM_i\frac{dV}{dt} = -\nabla P_e + J \times B - nM_i\nu_i V \tag{5.2}$$

$$\text{Particle continuity:} \quad \frac{\partial n}{\partial t} + \nabla \cdot nV = 0 \tag{5.3}$$

$$\text{Ohm's law:} \quad E + V_e \times B = -\frac{1}{en}\nabla P_e \tag{5.4}$$

$$\text{Current constraint:} \quad \nabla \cdot J \approx 0 \tag{5.5}$$

$$\text{Pressure dynamics:} \quad \frac{\partial P_e}{\partial t} + \nabla \cdot (P_e V_E) + (\gamma - 1)P_e \nabla \cdot V_E = \gamma\frac{2}{\omega_{ci}}\hat{b} \times \kappa \cdot \nabla(P_e C_s^2) \tag{5.6}$$

Note the velocities in these equations; in the force balance equation, the velocity is that of the bulk fluid plasma, dominantly the $E \times B$ drift. In Ohm's law, V_e describes the electron fluid velocity, which is primarily due to $E \times B$ and diamagnetic drifts. Next, as the pressure felt by the ions is composed of the ion and electron partial pressures, if we approximate that $T_i \approx 0$, the pressure is only from the electron contribution. The second and third terms on the LHS of the pressure equation are related to adiabaticity and the RHS is a collisionless heat flux.

In the following subsections we will transform each of the above equations into flux-tube averaged dipole coordinates in detail.

5.1.1 Particle Continuity

We define the number of particles in a flux-tube as the flux-tube average of the particle density times the differential flux-tube volume:

$$N(\psi, \varphi, t) \equiv < n > \delta V \tag{5.7}$$

where the brackets denote flux-tube averaging.

In the absence of sources and sinks, the particle continuity equation has the form:

$$\frac{\partial n}{\partial t} + \nabla \cdot nV = 0$$

where n is the particle density and V is the particle velocity. Considering the electrons, we can find the velocity from Ohm's law:

$$E + V_e \times E = -\frac{1}{en}\nabla P_e \Rightarrow V = \frac{E \times B}{B^2} - \frac{1}{en}\frac{B \times \nabla P_e}{B^2}$$

where these are the $E \times B$ and diamagnetic drifts, respectively. Expressing these in dipole coordinates,

$$E = -\nabla\Phi = -\frac{\partial\Phi}{\partial u^i}\nabla u^i = -\frac{\partial\Phi}{\partial\psi}\nabla\psi - \frac{\partial\Phi}{\partial\varphi}\nabla\varphi$$
$$P_e = \frac{\partial P_e}{\partial\psi}\nabla\psi + \frac{\partial P_e}{\partial\varphi}\nabla\varphi$$

So our expression for electron velocity becomes:

$$
\begin{aligned}
V_e &= -\frac{\partial\Phi}{\partial\psi}\frac{\nabla\psi\times\nabla\chi}{|\nabla\chi|^2} - \frac{\partial\Phi}{\partial\varphi}\frac{\nabla\varphi\times\nabla\chi}{|\nabla\chi|^2} - \frac{\partial P_e}{\partial\psi}\frac{\nabla\chi\times\nabla\psi}{enB^2} - \frac{\partial P_e}{\partial\phi}\frac{\nabla\chi\times\nabla\phi}{enB^2} \\
&= -\frac{\partial\Phi}{\partial\psi}\frac{\nabla\varphi|\nabla\chi||\nabla\psi|}{|\nabla\chi|^2} + \frac{\partial\Phi}{\partial\varphi}\frac{\nabla\psi|\nabla\chi||\nabla\varphi|}{|\nabla\chi|^2} + \frac{\partial P_e}{\partial\psi}\frac{|\nabla\chi||\nabla\psi|}{en|\nabla\chi|^2}\frac{\nabla\varphi}{|\nabla\varphi|} - \frac{\partial P_e}{\partial\varphi}\frac{|\nabla\chi||\nabla\varphi|}{en|\nabla\chi|^2}\frac{\nabla\psi}{|\nabla\psi|} \\
&= -(\frac{\partial\Phi}{\partial\psi} - \frac{1}{en}\frac{\partial P_e}{\partial\psi})\frac{\nabla\varphi}{|\nabla\varphi|^2} + (\frac{\partial\Phi}{\partial\varphi} - \frac{1}{en}\frac{\partial P_e}{\partial\varphi})\frac{\nabla\psi}{|\nabla\psi|^2}
\end{aligned}
$$

Before returning to the continuity equation, we observe that the divergence of a vector in general coordinates is:

$$
\nabla\cdot\vec{A} = \nabla\cdot(A^i\sqrt{g}\frac{\vec{e}_i}{\sqrt{g}}) = \frac{\vec{e}_i}{\sqrt{g}}\cdot\nabla(A^i\sqrt{g}) = \frac{1}{\sqrt{g}}\frac{\partial(A^i\sqrt{g})}{\partial u^i} \tag{5.8}
$$

where $\nabla\cdot(\frac{\vec{e}_i}{\sqrt{g}}) = 0$ is used between the first and second step, then $\vec{e}_i\cdot\nabla f = \frac{\partial f}{\partial u^i}$. Recalling that $A^i = \vec{A}\cdot\nabla u^i$:

$$
\begin{aligned}
\nabla\cdot(n\vec{v}) =& \frac{1}{\sqrt{g}}\frac{\partial(nv^i\sqrt{g})}{\partial u^i} \\
=& B^2\frac{\partial}{\partial\psi}(\frac{\nabla\psi\cdot nV_e}{B^2}) + B^2\frac{\partial}{\partial\varphi}(\frac{\nabla\varphi\cdot nV_e}{B^2}) \\
=& -B^2\frac{\partial}{\partial\varphi}(\frac{n}{B^2}\frac{\partial\Phi}{\partial\psi} - \frac{1}{en}\frac{\partial P_e}{\partial\psi}) + B^2\frac{\partial}{\partial\psi}(\frac{n}{B^2}\frac{\partial\Phi}{\partial\varphi} - \frac{1}{en}\frac{\partial P_e}{\partial\varphi})
\end{aligned}
$$

Taking a flux tube average, assuming Φ and P_e as constant along field lines,

$$
\begin{aligned}
<\nabla\cdot(n\vec{v})>\delta V =& -\int_{-\infty}^{+\infty} B^2\frac{\partial}{\partial\varphi}(\frac{n}{B^2}\frac{\partial\Phi}{\partial\psi} - \frac{1}{en}\frac{\partial P_e}{\partial\psi})\frac{d\chi}{B^2} \\
&+ \int_{-\infty}^{+\infty} B^2\frac{\partial}{\partial\psi}(\frac{n}{B^2}\frac{\partial\Phi}{\partial\varphi} - \frac{1}{en}\frac{\partial P_e}{\partial\varphi})\frac{d\chi}{B^2} \\
=& -\frac{\partial}{\partial\varphi}(N\frac{\partial\Phi}{\partial\psi} - \frac{\delta V}{e}\frac{\partial P_e}{\partial\psi}) + \frac{\partial}{\partial\psi}(N\frac{\partial\Phi}{\partial\varphi} - \frac{\delta V}{e}\frac{\partial P_e}{\partial\varphi})
\end{aligned}
$$

With this, we find the flux-tube averaged continuity equation as,

$$\frac{\partial N}{\partial t} - \frac{\partial}{\partial \varphi}\Big(N\frac{\partial \Phi}{\partial \psi} - \frac{\delta V}{e}\frac{\partial P_e}{\partial \psi}\Big) + \frac{\partial}{\partial \psi}\Big(N\frac{\partial \Phi}{\partial \varphi} - \frac{\delta V}{e}\frac{\partial P_e}{\partial \varphi}\Big) = 0 \tag{5.9}$$

5.1.2 Current Constraint

By crossing the momentum equation with B, one arrives at an expression for the perpendicular current density,

$$\vec{J} = \frac{\vec{B} \times \nabla P_e}{B^2} + \frac{nM_i}{B^2}\vec{B} \times \Big(\frac{dV_E}{dt} + \nu_i V_E\Big)$$

where V_E is the $E \times B$ velocity. Expressing this in terms of the gradient vectors of dipole coordinates:

$$\vec{J} = \frac{\nabla\chi \times (\frac{\partial P}{\partial \psi}\nabla\psi + \frac{\partial P}{\partial \varphi}\nabla\varphi)}{B^2} + \frac{nM_i}{B^2}\nabla\chi \times \Big(\frac{d}{dt} + \nu_i\Big)\Big(\frac{\nabla\chi \times (\frac{\partial \Phi}{\partial \psi}\nabla\psi + \frac{\partial \Phi}{\partial \varphi}\nabla\varphi)}{B^2}\Big)$$

Next, using:

$$\nabla\varphi \times \nabla\psi = \nabla\chi \qquad \nabla\chi \times \nabla\varphi = \frac{|\nabla\varphi||\nabla\chi|}{|\nabla\psi|}\nabla\psi \qquad \nabla\psi \times \nabla\chi = \frac{|\nabla\psi||\nabla\chi|}{|\nabla\varphi|}\nabla\varphi$$

the expression for J can be rewritten as:

$$\vec{J} = -\frac{\partial P}{\partial \psi}\frac{\nabla\varphi}{|\nabla\varphi|^2} + \frac{\partial P}{\partial \varphi}\frac{\nabla\psi}{|\nabla\psi|^2} - \frac{nM_i}{B^2}\Big(\frac{d}{dt} + \nu_i\Big)\Big(\frac{\partial \Phi}{\partial \psi}\nabla\psi + \frac{\partial \Phi}{\partial \varphi}\nabla\varphi\Big)$$

Plugging this into the expression for divergence free current density,

$$\begin{aligned}\nabla\cdot\vec{J} =& \frac{1}{\sqrt{g}}\frac{\partial(J^i\sqrt{g})}{\partial u^i} = B^2\frac{\partial(\frac{\vec{J}\cdot\nabla u^i}{B^2})}{\partial u^i}\\ =& B^2\frac{\partial}{\partial\psi}\Big(\frac{1}{B^2}\frac{\partial P}{\partial\varphi} - \frac{nM_i}{B^4}\Big(\frac{d}{dt}+\nu_i\Big)\Big(\frac{\partial\Phi}{\partial\psi}|\nabla\psi|^2\Big)\Big)\\ &+ B^2\frac{\partial}{\partial\varphi}\Big(-\frac{1}{B^2}\frac{\partial P}{\partial\psi} - \frac{nM_i}{B^4}\Big(\frac{d}{dt}+\nu_i\Big)\Big(\frac{\partial\Phi}{\partial\varphi}|\nabla\varphi|^2\Big)\Big)\end{aligned}$$

We can take the flux-tube average to find:

$$\begin{aligned}<\nabla\cdot\vec{J}>\delta V =& \frac{\partial}{\partial\psi}\Big(\delta V\frac{\partial P}{\partial\varphi}\Big) - \frac{\partial}{\partial\varphi}\Big(\delta V\frac{\partial P}{\partial\psi}\Big)\\ &- \frac{\partial}{\partial\psi}\Big(\int_{-\infty}^{+\infty}\frac{d\chi}{B^2}\frac{nM_i}{B^2}|\nabla\psi|^2\Big(\frac{d}{dt}+\nu_i\Big)\Big(\frac{\partial\Phi}{\partial\psi}\Big)\Big)\\ &- \frac{\partial}{\partial\varphi}\Big(\int_{-\infty}^{+\infty}\frac{d\chi}{B^2}\frac{nM_i}{B^2}|\nabla\varphi|^2\Big(\frac{d}{dt}+\nu_i\Big)\Big(\frac{\partial\Phi}{\partial\varphi}\Big)\Big) = 0\end{aligned}$$

which can be reorganized as

$$-<\nabla\cdot\vec{J}>\delta V = \Big(\frac{d}{dt}+\nu_i\Big)\Big[\frac{\partial}{\partial\psi}\Big(\epsilon_\psi\frac{\partial\Phi}{\partial\psi}\Big) + \frac{\partial}{\partial\varphi}\epsilon_\varphi\frac{\partial\Phi}{\partial\varphi}\Big] - \frac{\partial}{\partial\psi}\Big(\delta V\frac{\partial P}{\partial\varphi}\Big) + \frac{\partial}{\partial\varphi}\Big(\delta V\frac{\partial P}{\partial\psi}\Big) = 0 \qquad (5.10)$$

where, with $|\nabla\psi|^2 = B^2L^2$ and $|\nabla\varphi|^2 = 1/L^2$,

$$\epsilon_\varphi = \int_{-\infty}^{+\infty}\frac{d\chi}{B^2}\frac{nM_i}{B^2}\frac{1}{L^2}, \qquad \epsilon_\psi = \int_{-\infty}^{+\infty}\frac{d\chi}{B^2}nM_iL^2$$

5.1.3 Pressure Dynamics

The pressure equation is again given as:

$$\frac{\partial P_e}{\partial t} + \nabla \cdot (P_e V_E) + (\gamma - 1) P_e \nabla \cdot V_E = \gamma \frac{2}{\omega_{ci}} \hat{b} \times \kappa \cdot \nabla (P_e C_s^2)$$

where κ is the field line curvature pointing in $-\hat{\psi}$ direction. Taking a closer look at the RHS:

$$\begin{aligned}
\gamma \frac{2}{\omega_{ci}} \hat{b} \times \kappa \cdot \nabla (P_e C_s^2) &= \gamma \frac{2 M_i}{e B^2} \nabla \chi \times (-\kappa_\psi \nabla \psi) \cdot \nabla (P_e C_s^2) \\
&= \gamma \frac{2 M_i}{e B^2} \kappa_\psi \frac{|\nabla \chi| |\nabla \psi|}{|\nabla \varphi|} \nabla \varphi \cdot \nabla \varphi \frac{\partial}{\partial \varphi} (P_e C_s^2) \\
&= \gamma \frac{2}{e} \kappa_\psi \frac{\partial (P_e T_e)}{\partial \varphi}
\end{aligned}$$

Finding the LHS in dipole coordinates,

$$\frac{\partial P_e}{\partial t} + B^2 \frac{\partial}{\partial \varphi}\Big(- \frac{P_e}{B^2} \frac{\partial \Phi}{\partial \psi}\Big) + B^2 \frac{\partial}{\partial \psi}\Big(\frac{P_e}{B^2} \frac{\partial \Phi}{\partial \varphi}\Big) + (\gamma - 1) P \Big[B^2 \frac{\partial}{\partial \varphi}\Big(- \frac{1}{B^2} \frac{\partial \Phi}{\partial \psi}\Big) + B^2 \frac{\partial}{\partial \psi}\Big(\frac{1}{B^2} \frac{\partial \Phi}{\partial \varphi}\Big)\Big]$$

and taking a flux-tube average,

$$\frac{\partial P_e}{\partial t} - \frac{\partial}{\partial \varphi}\Big(P_e \frac{\partial \Phi}{\partial \psi}\Big) + \frac{1}{\delta V} \frac{\partial}{\partial \psi}\Big(P_e \delta V \frac{\partial \Phi}{\partial \varphi}\Big) + (\gamma - 1) \frac{P}{\delta V} \frac{\partial \delta V}{\partial \psi} \frac{\partial \Phi}{\partial \varphi}$$

where the last two terms can be combined by multiplying/dividing by δV^γ. Canceling terms, the expression for the flux-tube averaged pressure equation is,

$$\frac{\partial P_e}{\partial t} - \frac{\partial P_e}{\partial \varphi} \frac{\partial \Phi}{\partial \psi} + \frac{1}{\delta V^\gamma} \frac{\partial (P_e \delta V^\gamma)}{\partial \psi} \frac{\partial \Phi}{\partial \varphi} = \gamma \frac{2}{e} \langle \kappa_\psi \rangle T_e \Big(2 \frac{\partial P_e}{\partial \varphi} - \frac{T_e}{\delta V} \frac{\partial N}{\partial \varphi}\Big) \tag{5.11}$$

where we have used $C_s^2 = T_e / M_i$, $P_e = \langle n \rangle T_e$, $\langle n \rangle = N \delta V$, and $\langle \kappa_\psi \rangle$ is the flux-tube averaged curvature. This pressure equation describes the adiabatic response of electron (LHS) modified by perturbations to the diamagnetic drift resulting in a collisionless heat flux (RHS).

5.1.4 Linearized Equations

In order to find a linear set of equations from the above nonlinear set, several assumptions are made. First we require that there is no equilibrium potential ($\Phi_0 = 0$), and that the equilibrium density and pressure profiles are axisymmetric ($\partial(N_0, P_0)/\partial\varphi = 0$). Starting with the continuity equation, by dropping higher order terms we find the linear expression,

$$\frac{\partial \tilde{N}}{\partial t} + \frac{\partial N_0}{\partial \psi}\frac{\partial \tilde{\Phi}}{\partial \varphi} - \frac{1}{e}\frac{\partial \delta V}{\partial \psi}\frac{\partial \tilde{P}_e}{\partial \varphi} \approx 0 \tag{5.12}$$

Similarly we find the linearized pressure equation,

$$\frac{\partial \tilde{P}_e}{\partial t} + \frac{1}{\delta V^\gamma}\frac{\partial}{\partial \psi}(P_0 \delta V^\gamma)\frac{\partial \tilde{\Phi}}{\partial \varphi} - \frac{2}{e}\gamma\langle\kappa_\psi\rangle T_e\Big(2\frac{\partial \tilde{P}_e}{\partial \varphi} - \frac{T_e}{\delta V}\frac{\partial \tilde{N}}{\partial \varphi}\Big) = 0 \tag{5.13}$$

where we have taken $T_e = P_e/\langle N\rangle$.

Next, the current constraint equation is linearized by neglecting the nonlinear convective derivative, $d/dt \approx \partial/\partial t$:

$$\Big(\frac{\partial}{\partial t} + \nu_i\Big)\Big(\frac{\partial}{\partial \psi}\epsilon_\psi\big(\frac{\partial \tilde{\Phi}}{\partial \psi}\big) + \frac{\partial}{\partial \varphi}\epsilon_\varphi\big(\frac{\partial \tilde{\Phi}}{\partial \varphi}\big)\Big) - \frac{\partial \delta V}{\partial \psi}\frac{\partial \tilde{P}}{\partial \varphi} = 0 \tag{5.14}$$

This expression indicates that the diamagnetic current of the electrons is balanced by the polarization current (and collision current) of the ions. Equations 5.12, 5.13, and 5.14 form the linearized representation of the gyro-fluid model for the plasma. This is the system we will use to understand our experimental results. Note that we will be making a comparison of a linear system to a highly nonlinear experiment, but it is a starting point that gives us intuition toward the more complicated system.

5.1.5 Normalized Equations

By normalizing these equations, we clarify the problem to be solved and allow for a simple comparison of similar systems at different scales. The resulting normalized problem is simply parameterized by one value and two equilibrium profiles. We normalize by values found at the equatorial radius, L_0. Here the magnetic flux is ψ_0, and the ion cyclotron frequency is $\omega_{ci,0} = eB_0/M_i$. We define the normalized flux coordinate, $y = \psi/\psi_0$, where at L_0, $y = 1$. The normalized sonic gyroradius is defined to be $\rho* = C_s/\omega_{ci}L_0$, allowing us to normalize time as $\tau = t/t_0$, where $t_0 = (\omega_{ci}\rho*^2)^{-1}$. From here on equilibrium quantities will be denoted with a 0 subscript, and quantities evaluated at L_0 with a (ψ_0). Note that T_e represents the equilibrium temperature profile.

In these normalized coordinates the flux-tube volume and its radial derivative become,

$$\delta V \to \frac{\delta V(\psi_0)}{y^4}, \qquad \frac{\partial \delta V}{\partial \psi} \to -\frac{4}{\psi_0}\frac{\delta V(\psi_0)}{y^5} \tag{5.15}$$

The equilibrium profiles are also normalized to their values at $y = 1$,

$$N_0 \to \frac{N_0(\psi)}{N_0(\psi_0)} = h_n(y), \qquad G_0 = P_0\delta V^\gamma \to \frac{G_0(\psi)}{G_0(\psi_0)} = h_g(y) \tag{5.16}$$

For the particle continuity equation, we normalize ψ with $y\psi_0$ and t with τt_0. So multiplying through by $t_0/N_0(\psi_0)$,

$$\frac{\partial}{\partial\tau}\frac{\tilde{N}}{N_0(\psi_0)} + \frac{t_0}{\psi_0}\frac{\partial h_n}{\partial y}\frac{\partial\tilde{\Phi}}{\partial\varphi} + \frac{4t_0}{e\psi_0 N_0(\psi_0)}\frac{\delta V(\psi_0)}{y^5}\frac{\partial\tilde{P}_e}{\partial\varphi} \approx 0$$

where one can show easily with $P_e\delta V = NT_e$ that

$$\frac{t_0}{\psi_0} = \frac{e}{T_e(\psi_0)} = \frac{e}{M_iC_s^2}, \qquad \frac{t_0\delta V(\psi_0)}{e\psi_0 N_0(\psi_0)} = \frac{1}{\langle n_0\rangle(\psi_0)T_e(\psi_0)} = \frac{1}{P_0(\psi_0)},$$

where the above left is our normalization for potential, and right is the normalization for pressure.

With these, the normalized continuity equation is

$$\frac{\partial \tilde{N}}{\partial t} + h_n' \frac{\partial \tilde{\Phi}}{\partial \varphi} + \frac{4}{y^5} \frac{\partial \tilde{P}_e}{\partial \varphi} \approx 0 \tag{5.17}$$

where $\tilde{N}, \tilde{\Phi}, \tilde{P}_e, t$ are now taken to be the normalized quantities.

In normalized coordinates $\langle \kappa_\psi \rangle = -4\delta V(\psi_0)/(2\delta V \psi_0 y^5)$. Utilizing this and multiplying the pressure equation by $t_0/P_0(\psi_0)$:

$$\frac{\partial}{\partial \tau} \frac{\tilde{P}_e}{P_0(\psi_0)} + y^{4\gamma} h_g' \frac{e}{T_e(\psi_0)} \frac{\partial \tilde{\Phi}}{\partial \varphi} + \gamma \frac{4}{y^5} \frac{t_0}{\psi_0} \frac{T_e \delta V(\psi_0)}{e \delta V} \Big(2 \frac{\partial}{\partial \varphi} \frac{\tilde{P}_e}{P_0(\psi_0)} - y^4 \frac{T_e}{T_e(\psi_0)} \frac{\partial}{\partial \varphi} \frac{\tilde{N}}{N_0(\psi_0)} \Big) = 0$$

Allowing the normalized quantities to be represented by the original variables, and observing that $y^4 T_e/T_e(\psi_0) = y^{4\gamma} h_g/h_n$, this expression reduces to:

$$\frac{\partial \tilde{P}_e}{\partial t} + y^{4\gamma} h_g' \frac{\partial \tilde{\Phi}}{\partial \varphi} + \gamma \frac{4}{y^5} (y^{4\gamma} \frac{h_g}{h_n}) \Big[2 \frac{\partial \tilde{P}_e}{\partial \varphi} - (y^{4\gamma} \frac{h_g}{h_n}) \frac{\partial \tilde{N}}{\partial \varphi} \Big] = 0 \tag{5.18}$$

Finally, we normalize the current constraint,

$$\Big(\frac{1}{t_0} \frac{\partial}{\partial \tau} + \nu_i \Big) \Big[\frac{1}{\psi_0} \frac{\partial}{\partial y} \epsilon_\psi \frac{1}{\psi_0} \frac{\partial \tilde{\Phi}}{\partial y} + \frac{\partial}{\partial \varphi} \epsilon_\varphi \frac{\partial \tilde{\Phi}}{\partial \varphi} \Big] + \frac{4}{y^5} \frac{\delta V(\psi_0)}{\psi_0} \frac{\partial \tilde{P}}{\partial \varphi} = 0$$

where

$$\frac{\partial \delta V(\psi_0)}{\partial \psi_0} = -\frac{1}{\psi_0} \frac{4}{y^5} \delta V(\psi_0)$$

Multiplying and dividing the ϵ terms by $N_0 = \langle n_0 \rangle \delta V$, and multiplying the entire equation by $e B_0^2 L_0^2 t_0/(N(\psi_0) M_i T_e(\psi_0))$,

$$\Big(\frac{\partial}{\partial t}+\nu_i t_0\Big)\frac{e}{N_0T_e}\Big[\frac{\partial}{\partial y}N_0E_y\frac{\partial\tilde{\Phi}}{\partial y}+\frac{\partial}{\partial\varphi}N_0E_\varphi\frac{\partial\tilde{\Phi}}{\partial\varphi}\Big]+\frac{4}{y^5}\frac{eB_0^2L_0^2t_0}{N_0M_iT_e}\frac{\delta V(\psi_0)}{\psi_0}\frac{\partial\tilde{P}}{\partial\varphi}=0$$

where the dimensionless dielectrics are

$$E_\varphi=\frac{1}{\delta V}\int_{-\infty}^{+\infty}\frac{d\chi}{B^2}\frac{n}{\langle n\rangle}\frac{B_0^2}{B^2}\frac{L_0^2}{L^2},\qquad\qquad E_y=\frac{1}{\delta V}\int_{-\infty}^{+\infty}\frac{d\chi}{B^2}\frac{n}{\langle n\rangle}\frac{L^2}{L_0^2}\tag{5.19}$$

Finally, normalizing the potential by $e/T_e(\psi_0)$, the density by $N_0(\psi_0)$ and the pressure by $\langle n_0\rangle(\psi_0)T_e(\psi_0)$, this takes the form

$$\rho_*^2\Big(\frac{\partial}{\partial t}+\nu_i t_0\Big)\Big[\frac{\partial}{\partial y}h_nE_y\frac{\partial\tilde{\Phi}}{\partial y}+\frac{\partial}{\partial\varphi}h_nE_\varphi\frac{\partial\tilde{\Phi}}{\partial\varphi}\Big]+\frac{4}{y^5}\frac{\partial\tilde{P}}{\partial\varphi}=0\tag{5.20}$$

5.1.6 Localized Equations

A dispersion relation is found by assuming the solutions can be Fourier decomposed in the azimuthal coordinate, then considering a subset of solutions at a special radial location. The complete set of modes in the Fourier basis is represented as:

$$\Big\{\tilde{\Phi}(\psi,\varphi,t),\tilde{N}(\psi,\varphi,t),\tilde{P}_e(\psi,\varphi,t)\Big\}=\Sigma\Big\{\Phi(\psi),N(\psi),P_e(\psi)\Big\}e^{-i(\omega_m t-m\varphi)}\tag{5.21}$$

Taking the pressure for example, $P=P_me^{i(m\varphi-\omega t)}$, the normalized derivative terms become:

$$\frac{\partial P}{\partial\varphi}=imP_me^{i(m\varphi-\omega t)},\qquad\qquad\frac{\partial P}{\partial\tau}=t_0\frac{\partial P}{\partial t}=-i\omega t_0P_me^{i(m\varphi-\omega t)}=-i\omega P_me^{i(m\varphi-\omega t)}\tag{5.22}$$

where in the rightmost expression we use ω to represent the normalized frequency ωt_0. All the derivatives of φ and t are expressed in this manner.

Next, localizing our solution to the radial location $y\approx 1$ where $\frac{\partial\Phi}{\partial y}\approx 0$, we see the linearized equations simplify to:

$$\omega\tilde{N} - mh_n'\tilde{\Phi} - 4m\tilde{P}_e \approx 0$$
$$\omega\tilde{P}_e - mh_g'\tilde{\Phi} - 4m\gamma\left[2\tilde{P}_e - \tilde{N}\right] = 0$$
$$\rho_*^2\left(\omega - i\nu_i t_0\right)m_\perp^2 E_\varphi\tilde{\Phi} + 4m\tilde{P}_e = 0$$

where, $m_\perp^2 \equiv m^2 - (E_y/E_\varphi)\tilde{\Phi}_m^{-1}\partial^2\tilde{\Phi}_m/\partial y^2|_{y=1}$ represents the total perpendicular mode number squared. Note that everything is now in terms of $\tilde{N}, \tilde{P}_e, \tilde{\Phi}$ as well as the presence of the h_n' and h_g' factors.

In the case where $h_n', h_g' = 0$, there with be a damped electrostatic convective cell with no density or pressure components as well as two stable modes rotating in the electron drift direction. One of these two modes rotates faster than the electron drift frequency, the other slightly slower. These correspond to the entropy modes driven by azimuthal pressure variations, the faster due to pressure variations from temperature, and the slower due to pressure variations from density.

This marginally stable case is the stability limit from ideal MHD. A critical parameter for stability, η, is related to a comparison of the pressure and density profile steepness as given by,

$$\eta = \frac{d\ln T}{d\ln N} = \frac{\nabla T_e}{\nabla N}\frac{N}{T_e} \tag{5.23}$$

For the MHD stability limit, $\eta = 2/3$. By including the collisionless heat flux in the pressure equation, instability can occur for more gentle pressure gradients [60]. It can also be seen that for steep temperature profiles with $\eta > 2/3$ the modes will rotate more quickly, while for steep density profiles ($\eta < 2/3$) the mode rotation will slow or even reverse direction, as was recently demonstrated on LDX via pellet lithium pellet injection [63]. Simulation indicates these instabilities drive the profiles to the marginally stable, or "invariant", profiles which yield $\eta = 2/3$ [64].

5.1.7 Including the Feedback

Lets now consider how the inclusion of feedback would change this system. Taking the electrode to be simply a source of current at a specific azimuthal and radial location in the plasma, at this location we are effectively saying $\nabla \cdot J \neq 0$. Specifically to describe the current into the plasma, an appropriate expression would be:

$$\delta V \langle \nabla \cdot J_{FB} \rangle = I_{FB} \delta(\psi - \psi_E) \delta(\varphi - \varphi_E) \tag{5.24}$$

where (ψ_E, φ_E) is the location of the electrode in the plasma. Assuming the electrode is in the volume of integration, clearly,

$$\int\int\int dV \nabla \cdot J = \int\int d\psi d\varphi \delta V \langle \nabla \cdot J \rangle = I_{\mathrm{FB}}$$

The current to the electrode is set by the gain and phase of the feedback circuit described in Chapter 3, the plasma potential at the electrode and sensor, and the electrode sheath resistance:

$$I_{\mathrm{FB}}(t) = \frac{1}{R}[- \Phi(\psi_E, \varphi_E, t) + G\Phi(\psi_S, \varphi_S, t)] \tag{5.25}$$

where the sign on the plasma potential is chosen by the convention for positive current flowing out of the electrode and $(\psi_E, S, \varphi_{E,S})$ are the locations of the electrode and sensor in the plasma. Taking the Fourier transform of our expression for the flux-tube integrated divergence of current,

$$\int_{-\infty}^{\infty} e^{im\varphi} \delta V \langle \nabla \cdot J \rangle d\varphi = \frac{e^{-i\omega t}}{R}[- \Phi(\psi_E) + G\Phi(\psi_S) e^{im(\varphi_S - \varphi_E)}] \delta(\psi - \psi_E)$$

Next, normalizing by the same factors applied to the current constraint in previous sections,

$$\delta V\langle \nabla \cdot J\rangle = \frac{t_0}{eN_0(\psi_0)}\frac{T_e}{e}\frac{e^{-i\omega t_0\tau}}{R\psi_0}\Big[-\frac{e\Phi(y_E)}{T_e}+G\frac{e\Phi(y_S)}{T_e}e^{im(\varphi_S-\varphi_E)}\Big]\delta(y-y_E)$$

where here we are normalizing the potential as usual, and the coefficient is dimensionless:

$$\frac{t_0}{eN_0(\psi_0)}\frac{T_e}{e}\frac{1}{R\psi_0}=\frac{1}{e\langle n_0\rangle(R\psi_0)\delta V(\psi_0)}\sim\frac{Bm^2}{e}\frac{1}{\Omega}=\Omega\frac{1}{\Omega}$$

The linearized, normalized current constraint equation with current injection feedback is now given as:

$$\rho_*^2\Big(\frac{\partial}{\partial t}+\nu_i t_0\Big)\Big[\frac{\partial}{\partial y}h_n E_y\frac{\partial\tilde{\Phi}}{\partial y}+\frac{\partial}{\partial\varphi}h_n E_\varphi\frac{\partial\tilde{\Phi}}{\partial\varphi}\Big]+\frac{4}{y^5}\frac{\partial\tilde{P}}{\partial\varphi}=$$
$$\Big[-\frac{e\Phi(y_E)}{T_e}+G\frac{e\Phi(y_S)}{T_e}e^{im(\varphi_S-\varphi_E)}\Big]\delta(y-y_E)e^{-i\omega t_0\tau}$$

5.2 Solving the Global Eigenvalue Problem

The linear equations 5.17, 5.18, 5.20 define a global eigensystem with eigenmodes of density, pressure and potential and corresponding eigenvalues. These eigenmodes are determined by radial gradients of the flux-tube integrated equilibrium profiles for density and pressure. We form a linear set of equations to be solved by using a second-order finite difference approximation for the radial derivatives and using a Fourier decomposition for the azimuthal derivatives. Provided here is a detailed description of the numerical global solve.

5.2.1 Equations to be Solved

Again, the normalized system of linear equations to be solved is given as:

$$\frac{\partial \tilde{N}}{\partial t} + h_n' \frac{\partial \tilde{\Phi}}{\partial \varphi} + \frac{4}{y^5}\frac{\partial \tilde{P}_e}{\partial \varphi} = 0$$
$$\frac{\partial \tilde{P}_e}{\partial t} + y^{4\gamma} h_g' \frac{\partial \tilde{\Phi}}{\partial \varphi} + \gamma \frac{4}{y^5}(y^{4\gamma}\frac{h_g}{h_n})\Big[2\frac{\partial \tilde{P}_e}{\partial \varphi} - (y^{4\gamma}\frac{h_g}{h_n})\frac{\partial \tilde{N}}{\partial \varphi}\Big] = 0$$
$$\rho_*^2\Big(\frac{\partial}{\partial t} + \nu_i t_0\Big)\Big[\frac{\partial}{\partial y} h_n E_y \frac{\partial \tilde{\Phi}}{\partial y} + \frac{\partial}{\partial \varphi} h_n E_\varphi \frac{\partial \tilde{\Phi}}{\partial \varphi}\Big] + \frac{4}{y^5}\frac{\partial \tilde{P}}{\partial \varphi} = 0$$

Note these are three coupled equations for the rate of change of potential, pressure and density. The h_n and h_g terms are the equilibrium radial profiles for density and entropy (pressure).

We can pose this problem as an eigensystem with minimal manipulation. Here the related eigenvectors for this system are composed of three distinct components:

$$\vec{x}_m \equiv \{\Phi_m, N_m, P_m\} \tag{5.26}$$

The linear eigensystem must be composed of an operator acting on an eigenvector resulting an equations of the form:

$$A \cdot \vec{x} = \omega \vec{x} \tag{5.27}$$

To put the above equations in this form, we use a finite difference approximation for the radial derivatives and a Fourier decomposition in the periodic (azimuthal) direction. Arranging terms properly, we get a system of the form:

$$\omega \mathcal{M} \cdot \vec{x} = \mathcal{N} \cdot \vec{x} \tag{5.28}$$

where the structure of $\mathcal{M}$ and $\mathcal{N}$ properly relate to the corresponding structure of $\vec{x}$, while the ω terms come from terms with time derivatives. As $\mathcal{M}$ is invertible (with given boundary conditions), we can rewrite this in the form of an eigensystem:

$$A \cdot \vec{x} = \mathcal{M}^{-1} \cdot \mathcal{N} \cdot \vec{x} = \omega \vec{x} \tag{5.29}$$

As such, the solve is an inversion of the matrix $\mathcal{M}$. In a later subsection we will go through the composition of the matrices in this system.

5.2.2 Equilibrium Profiles

The entire solve depends on only three parameters. These are the normalized sonic gyro radius, ρ^*, and the two normalized equilibrium profiles for density and entropy, h_n and h_g. ρ^* is a scaling which depends only on the electron temperature and the magnetic field strength, which relates to the relative importance of the ion inertial term. As such, this term is set by our estimates of the electron temperature in CTX and the known magnetic field.

The actual profiles are known with significantly less accuracy, and so here we make some assumptions. The equation which defines the density and pressure profiles is described in [16] and is trifurcated:

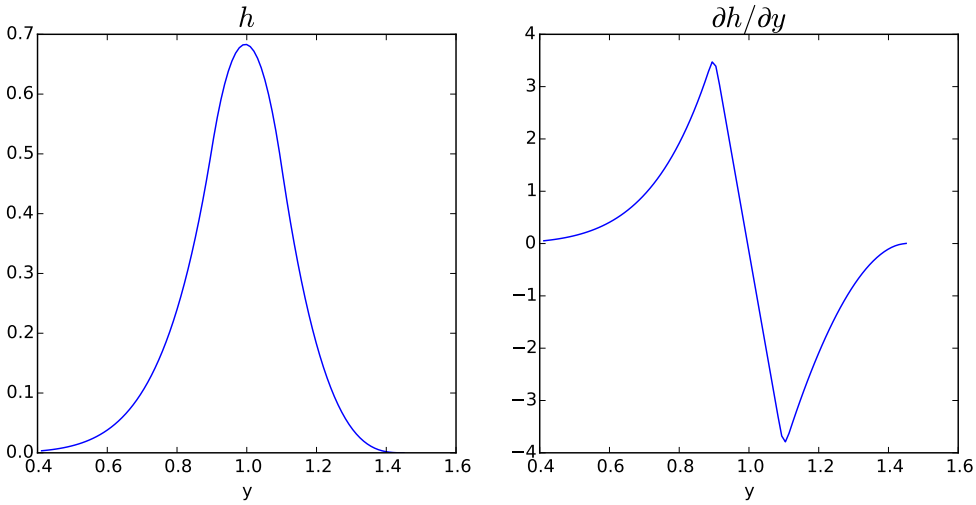

Figure 5.1: The profile function h and its derivative. Notice the change in sign of the derivative term at $y = 1$.

$$h(y) = \begin{cases} \left(\frac{y-y_{\max}}{1-y_{\max}}\right)^{\alpha} & y > 1 + \delta y \\ Ay^2 + By + C & 1 + \delta y > y > 1 - \delta y \\ y^{4c} & y > 1 + \delta y \end{cases} \tag{5.30}$$

where $\alpha = 4c(|y| - 1)$ and A, B, C are chosen such that h and its derivative are continuous, as shown in Figure 5.1. This piece-wise continuous function is used as the base profile for both the density and the entropy. These are given as,

$$h_N(y, c, h_0, y_{\max}) = (1 - h_0)\frac{1}{y^4}h(y, c, y_{\max}) + h_0$$
$$h_G(y, c, h_0, y_{\max}) = (1 - h_0)\frac{1}{y^{20/3}}h(y, c, y_{\max}) + h_0$$

Adjusting the steepness and peak of these profiles allows us to find reasonable conditions where the eigenmodes resemble the structure, growth rates and rotation frequency of the modes we experimentally observe. For a central density of 7.5×10^{10} cm^{-3}, peak electron temperature ($T_e = P_e/n$) of 50 eV, $c_N = .9$, $c_G = 1.97$, we find the profiles in Figure 5.2. From Equations 5.17, 5.18, 5.20, we see that these terms and their derivatives determine the nature of the eigensystem.

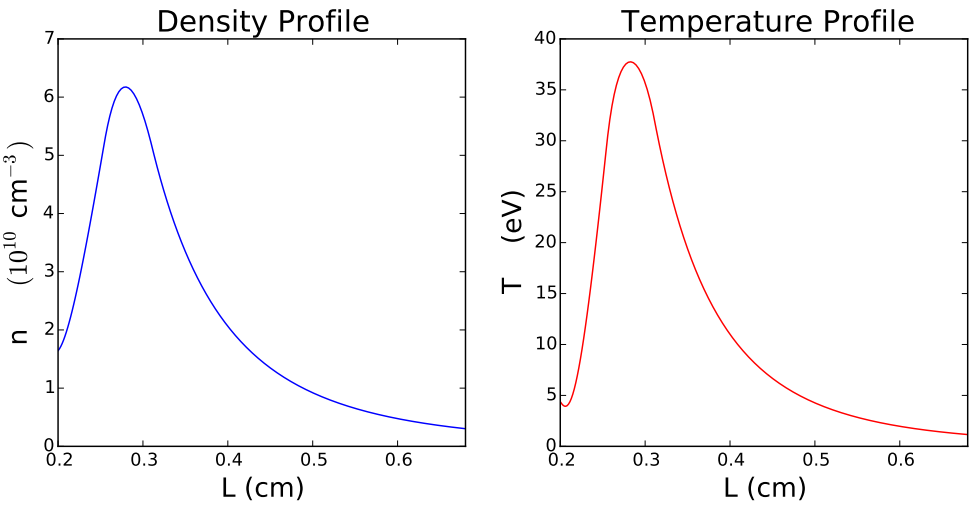

Figure 5.2: Density and temperature profiles used for the calculations.

5.2.3 Matrix Structure

The problem will be solved on an $n \times n$ domain. Given the three equations, this means that the matrices that need to be solved will be $3n \times 3n$, as at each grid point there is a potential, density and pressure. These matrices are clearly sparse, and the structure of each determined by the approximations to the operators and the coupling between the terms.

Equation 5.28 is composed of two matrices, $\mathcal{M}$ and $\mathcal{N}$. First, the structure of these matrices is fundamentally determined by the organization of our eigenvector (the unknowns we are solving for). This is chosen to be arranged as:

$$\vec{x}_m = \Big(\Phi[1], \Phi[2], ..., \Phi[n-1], N[1], N[2], ..., N[n-1], P[1], P[2], ..., P[n-1]\Big) \tag{5.31}$$

where the [0] and [n] terms are known (boundary conditions) and are not solved for. As such, the system effectively looks like:

$$A\vec{x}_m = A \begin{pmatrix} \Phi \\ N \\ P \end{pmatrix} \tag{5.32}$$

With this structure, we can think of the matrices as composed of 9 sections. The top rows of these matrices (three sections) describe the Possion equation contribution to the system. The middle rows are due to the continuity equations and the bottom rows from pressure dynamics. The columns of these matrices represent the components of each equation that are related to a particular quantity. The left columns contain terms with potential, the middle with density and the right columns are pressure terms. Figure 5.3 illustrates this description for clarity.

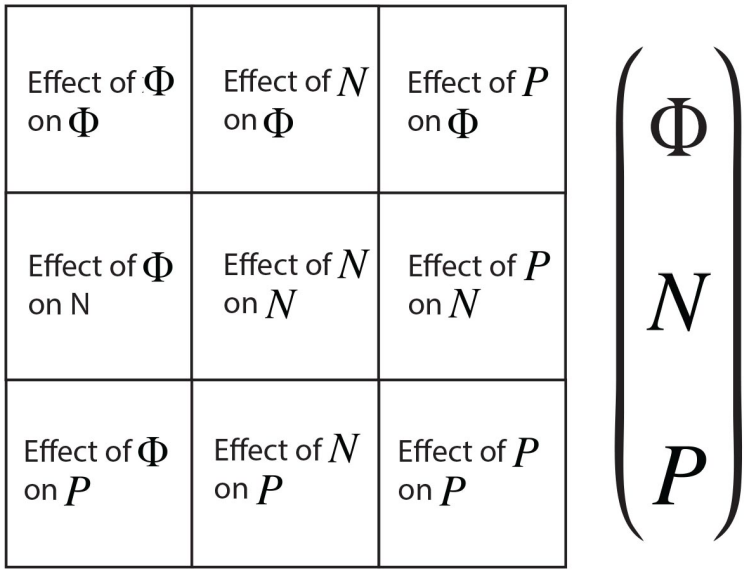

Figure 5.3: Structure of matrices and vectors in terms of the potential, density and pressure components. The matrix representation on the left displays the organization of the coupling.

Using this representation, we describe the matrices of Equations 5.28, where the M matrices involve time derivatives (ω), and the N matrices describe the coupling. Notice that the M matrices for the density and pressure equations simply have 1's on the diagonal, while for the current constraint, the matrix is tridiagonal as this equation involves a second derivative in space. These contributions are illustrated for a small case (n = 10) in Figure 5.4. Note that the total M matrix is

the sum of these contributions.

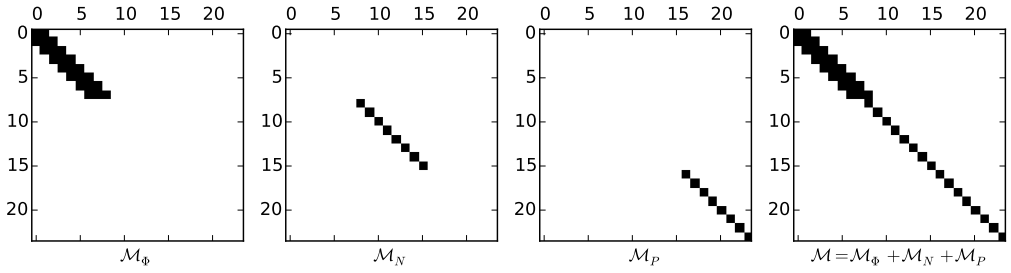

Figure 5.4: Structure of the $\mathcal{M}$ matrix. The potential involves off-diagonal terms due to the radial derivatives.

Similar to the $\mathcal{M}$ matrix, the $\mathcal{N}$ matrix is composed of sub-matrices representing the terms without time derivatives. Figure 5.5 displays an example of these matrices. Note that the "Φ" rows are missing contributions related to the density (N) as the current constraint is not directly dependent on density. The structure of the matrix describes the coupling taking place.

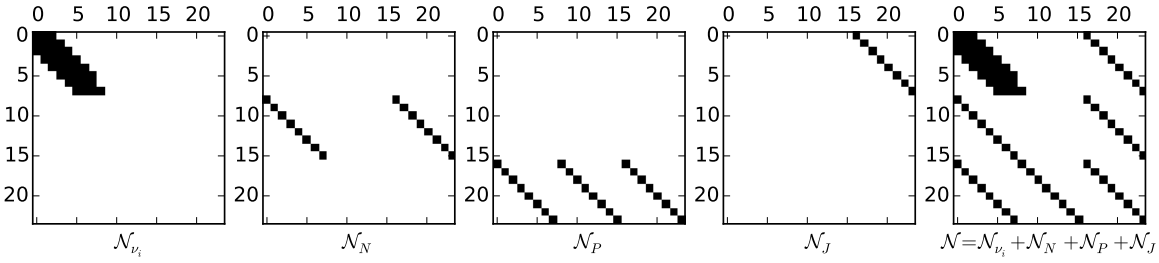

Figure 5.5: Structure of the $\mathcal{N}$ matrix. The coupling of the potential, density and pressure from the three equations can be observed from the non-zero elements (black).

5.2.4 Eigensystem

The entire eigensystem is now described in the form $\omega\mathcal{M}\cdot\vec{x}=\mathcal{N}\cdot\vec{x}$. We find the eigenvalues and eigenmodes by multiplying each side of the system by the inverse of $\mathcal{M}$,

$$\mathcal{M}^{-1}\mathcal{N}\cdot\vec{x}=\omega\mathcal{M}^{-1}\mathcal{M}\cdot\vec{x}=\omega\vec{x}$$

where ω, are the complex eigenvalues related to the growth rate and rotation frequency of the eigenmodes, $\vec{x}$. The first $n-2$ values of the eigenmode describe the potential structure, the next $n-2$ describe the density mode, and the remaining describe the pressure. Given that we are solving an $n \times n$ system, we will get n eigenvectors each composed of three components. We solve this for a system with n = 100 and the profiles of Figure 5.2. The eigenvalues for these modes are plotted in Figure 5.6 on the complex plane. Growth rates below zero are damped modes, above zero are unstable modes. From these eigenvalues we find the mode with the highest growth rate and assume this mode is dominant. In Figure 5.6, the rotation rate of the dominant mode is roughly 5 kHz.

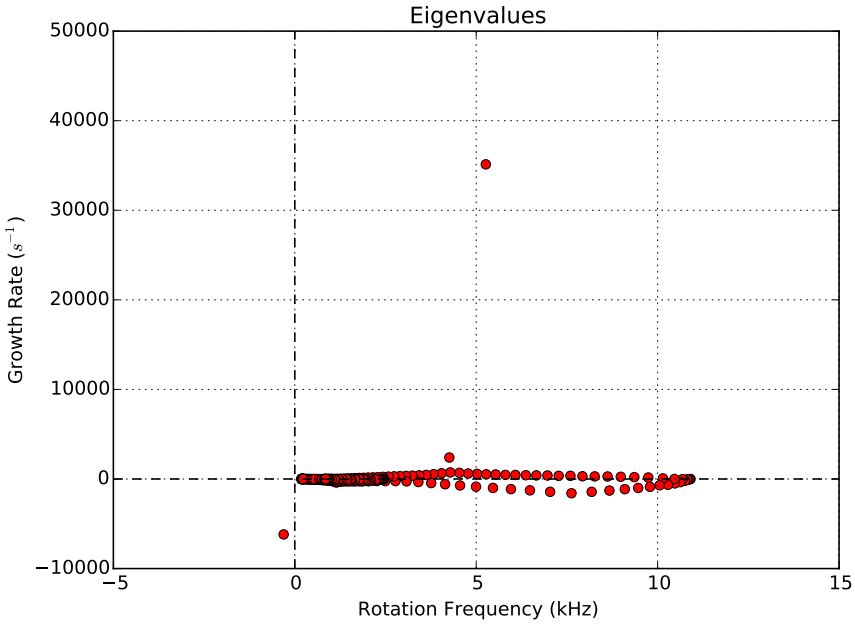

Figure 5.6: The 100 eigenvalues from the solve. The real part (rotation rate) is on the x-axis, and the imaginary part (growth rate) is on the y-axis. The dominant mode is taken to be the mode with the largest growth rate, here roughly 3.5×10^4 s^{-1}

Looking at the eigenvector corresponding to the dominant mode, Figure 5.7 plots the real (blue) and imaginary (red) parts of the radial profile for the three components. The broad radial structure of the potential is characteristic of modes observed in dipole-confined plasmas [11, 13].

The azimuthal phasing of the potential, density and pressure is revealed by the real and imaginary components of the modes. Figure 5.8 shows the azimuthal structure of these modes and the phase

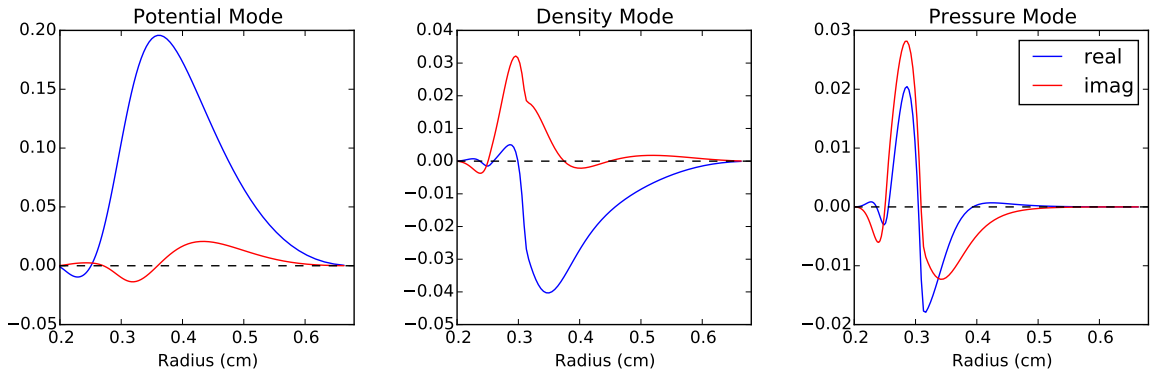

Figure 5.7: The real and imaginary parts of the potential, density, and pressure components of the dominant mode.

shifts between them.

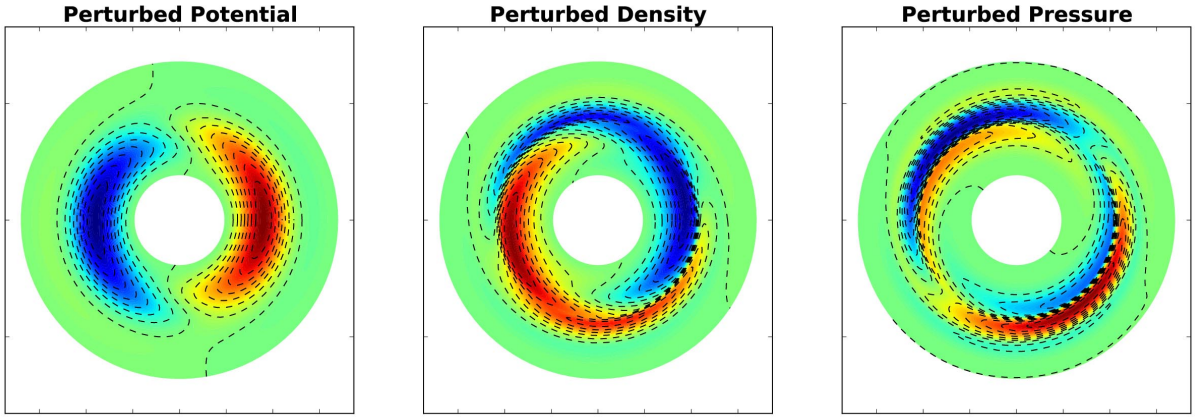

Figure 5.8: The two dimensional structure of the dominant eigenmode in potential, density and pressure.

5.2.5 The Addition of Current Injection

We include the effects of the current injection term described earlier in this Chapter by adding a matrix to N with only two elements, one representing the potential at the sensor location, the other at the electrode location. These are given by the expression:

$$M_{\mathrm{FB}} = \frac{1}{R}\Big(- \Phi[i_E, j_E]e^{i\varphi_E} + |G|\Phi[i_S, j_E]e^{i(\varphi_S + \Delta\phi}\Big) \tag{5.33}$$

where R is the sheath resistance of the electrode is taken to be 200 Ω. The indices i_S and i_E represent the radial location of the sensor and electrode, respectively. The case most representative of the experimental configuration is shown in Figure 5.9, with the sensor at 45 cm and the electrode at 44 cm.

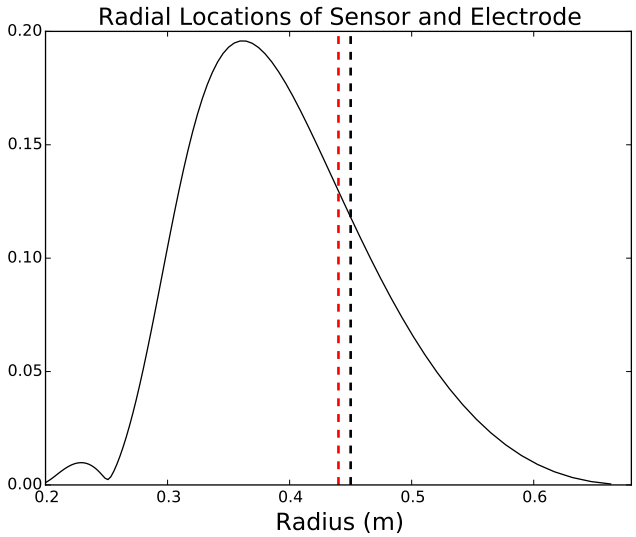

Figure 5.9: The radial locations of the sensor and electrode elements superimposed on the dominant potential eigenmode.

Notice the index of the terms is chosen to only effect the location of the electrode as determined by the potential at the sensor. Using the gain, $|G|$, and phase setting, $\Delta\phi$, we can simulate phase and gain scans similar to those performed experimentally.

Note that we are making the assumption that the probe acts only as a source of current, not a source or sink of particles. CTX plasmas in this turbulent state are maintained in an equilibrium between the source of plasma from the ECRH and the losses of plasma to the walls and magnet. This model make no attempt to represent this. Similarly, particles lost to the electrode surface are not modeled. From probe theory we can assume for relatively small variations about the floating

potential that the ion current to the probe is constant, while we vary the amount of collected electrons. Modeling this would require a steady loss of ions with a fluctuating electron sink term. We choose to only represent the current injected by the electrode as a simplified model of the feedback influence on the plasma.

5.2.6 Quantifying the Effects of Current Injection

In the plasma, the sensor (a floating potential probe) doesn't measure the amplitude of one mode, but all modes. Similarly, the response to feedback isn't the effect on an individual mode, but the collective effect on all the modes composing the turbulent spectrum. To compare the model described in this section to the feedback performed experimentally, we must use an analogous treatment.

In observing the effect of the above current source on the eigenmode amplitude, we can measure the mode amplitude at the "sensor" location on the grid. Each of the 100 eigenvectors will have a mode amplitude at this location for potential, density and pressure. How these mode amplitudes change with applied feedback phase and gain is what we wish to compare.

As mentioned above, we take the dominant mode to have the largest growth rate. Therefore, we say the subdominant modes proceed in decreasing growth rate. The response of all the eigenmodes to the current injection term is taken to be the response of the "plasma" to feedback. Taking the squared amplitude of each mode at the sensor location, we sum these mode amplitudes weighted by the growth rate of each eigenmode. This is normalized by the same value calculated without the current injection. This summed normalized amplitude is explicitly given as:

$$\frac{\Sigma\gamma_m|\Phi_m[i_S][\varphi_S]|^2}{\Sigma\gamma_{m0}|\Phi_{m0}[i_S][\varphi_S]|^2} \tag{5.34}$$

where the potential Φ_m is evaluated at the sensor location, both radially and azimuthally for each eigenmode, and the 0 in the denominator represents the values without current injection.

In addition to the change in mode amplitude, there is also an associated change in mode rotation

frequency when current injection is applied. We can account for this with an approach similar to the change in mode amplitude. We still weight the dominant modes by their growth rates, but also weight them by their rotation frequency, normalized in an appropriate manner:

$$\frac{\Sigma\gamma_m\omega_m|\Phi_m[i_S][\varphi_S]|^2}{\Sigma\gamma_{m0}\omega_{m0}|\Phi_{m0}[i_S][\varphi_S]|^2} \tag{5.35}$$

with ω_m the mode rotation frequency of each eigenmode.

5.2.7 Phase and Gain Scans

Using the current injection described above, we can simulate the gain and phase scans performed experimentally. By varying $|G|$ and $\Delta\phi$ in Equation 5.33, we can adjust the effective gain and applied phase, respectively. The response of the eigenmodes in amplitude and rotation rate is quantified using Equations 5.34 and 5.35. For the eigensystem solved in Figure 5.6, we simulate a phase scan with the gain set to 4 (similar to experimental settings) with the sensor-electrode separation equal to 12°. The left plot of Figure 5.10 shows the relative change in summed mode amplitude at the sensor, while the right plot shows the change is mode rotation rate. We see that the summed mode amplitude is amplified by roughly 40% near 0°, and suppressed by more than 40% near 150°. The frequency also displays a changing rotation rate that is shifted from the trend in amplitude by 90°. This is typical of many feedback systems [54].

By varying the magnitude of the gain G we also perform scans of gain. Similar to the experimental gain scans, by setting the feedback for peak amplification and suppression, with $|G| = 4$, we perform scans from $G = \pm 4$. The summed mode amplitude and change in frequency for this scan is plotted in Figure 5.11. We observe amplification and suppression of mode amplitude up to ±40%. A trend in changing frequency is also observed with varied gain.

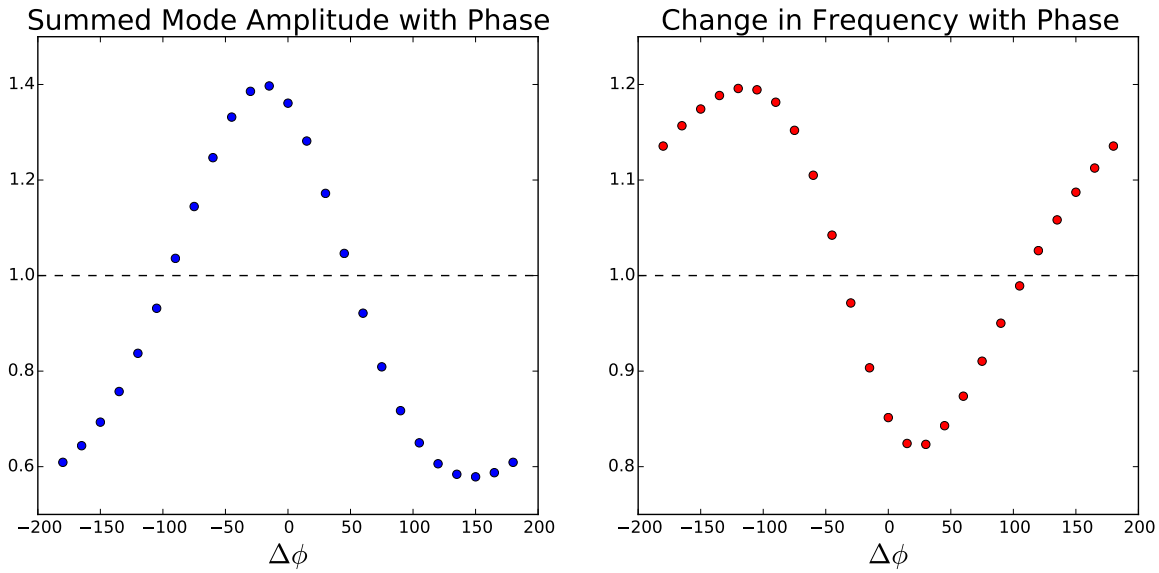

Figure 5.10: Phase scan performed with current injection term included in model. Left, Equation 5.34 with applied phase. Right, Equation 5.35 with applied phase.

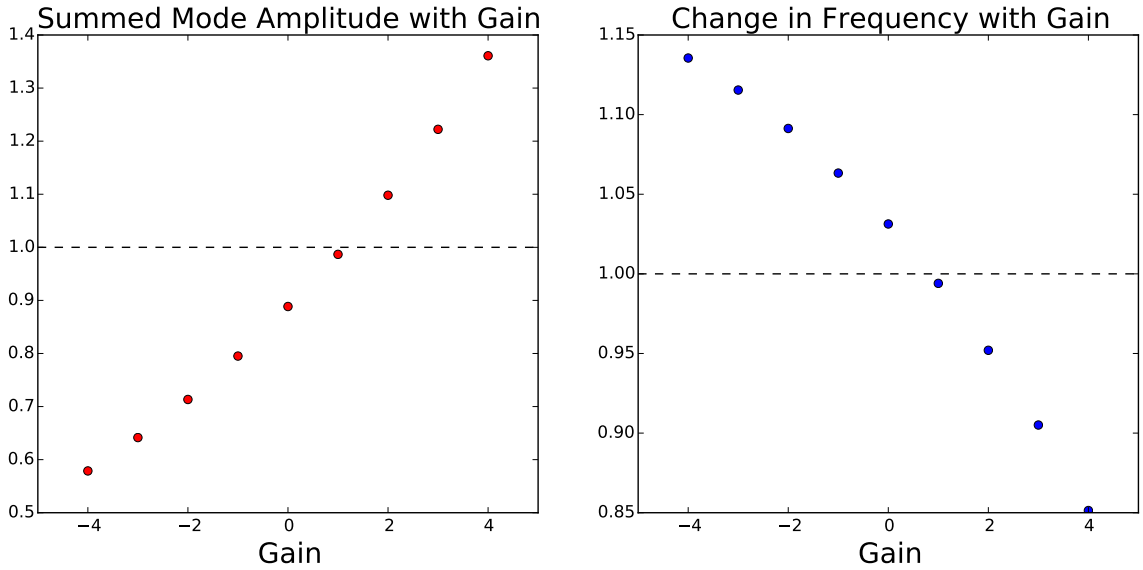

Figure 5.11: Gain scan performed with current injection. Left, Equation 5.34 with gain. Right, Equation 5.35 with gain.

5.3 Comparing the Model to the Experiment

We summarized the results of the experimentally perform gain and phase scans by integrating over the modified spectra and normalizing by the integral of the "natural" spectrum (Equations 4.2 and 4.1). In doing this we looked at the summed response to feedback over all the modes in the frequency band of integration. This is similar to the summing over the eigenmodes of Equations 5.34 and 5.35. We directly compare the experimental feedback results to the calculated eigenmode response with current injection in this manner. Figure 5.12 plots an overlay of the experimental results from Figure 4.11 with the calculated results of Figure 5.10, with the modification to the summed amplitudes on top and the change in frequency in the lower plot.

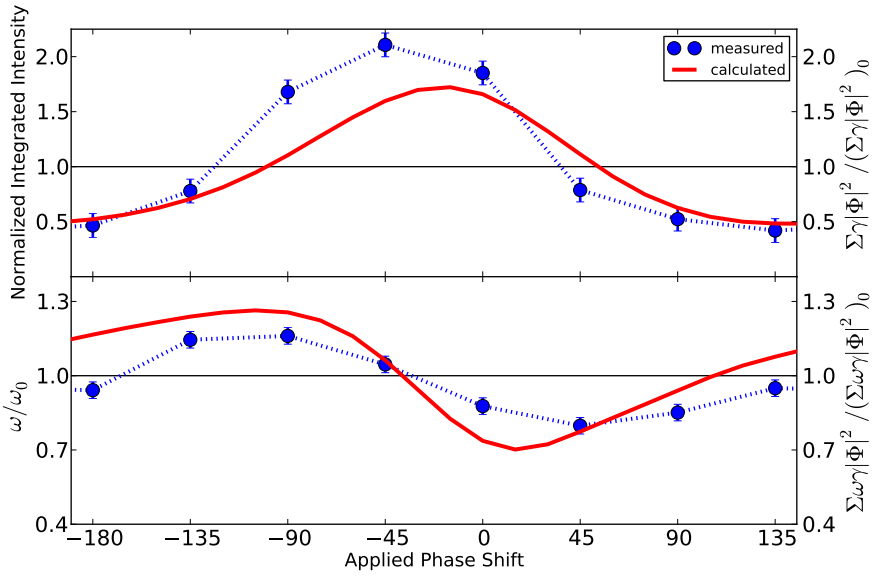

Figure 5.12: Comparison of the experimental phase scan results (blue) to the current injection scans of the eigensystem (red). Top is the relative change in intensity/mode amplitude, and on bottom is the relative change in dominant mode frequency.

While the general trends appear similar, we observe some important differences between the response of the eigensystem and the response of the plasma. Considering the modification to the intensity (amplitude), we see that we can obtain comparable levels of suppression, but we are not able to achieve the same amplification as measured experimentally (for similar gain and resistance). Additionally, there is roughly a 30° phase shift between the trends. Considering the lower plot of

Figure 5.12, we obtain similar shifts in the frequency of the dominant modes, but there is again a slight phase shift between the trends.

We compare the gain scans in the same manner. Figure 5.13 displays the experimental gain scan results of Figure 4.13 (blue) with the calculated results of Figure 5.11. The summed mode amplitude follows a similar trend to what we observe experimentally, with amplification occuring after a gain of 1, and suppression for gain less than 1, which is in accord with the form of Equation 4.3. We again observe that while the levels of suppression are comparable, the predicted amplification is less than what is measured. Additionally, the trend predicted in frequency is not observed.

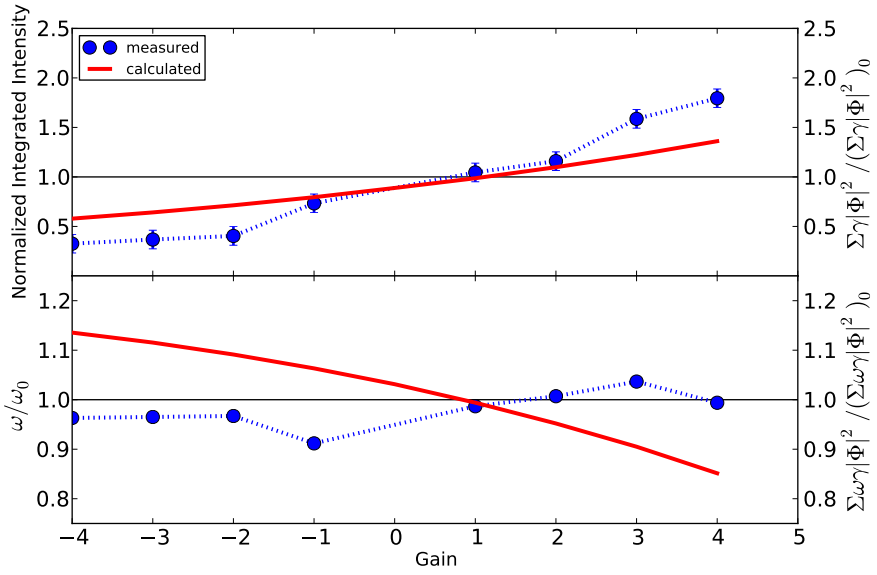

Figure 5.13: Comparison of the experimental gain scan results (blue) to the current injection scans of the eigensystem (red). Top is the relative change in intensity/mode amplitude, and on bottom is the relative change in dominant mode frequency.

Considering we are comparing the eigenmodes from a linearized model to the response of a turbulent plasma, there is substantial agreement between these results. Clearly a nonlinear model is required to fully understand what is taking place in these highly nonlinear plasmas. Additionally, modeling of the particle sources and sinks may be important in understanding the dynamics of the turbulent collisional plasmas in CTX. Appendix H describes an existing nonlinear simulation which has been used to explain the dynamics of previous experimental studies on CTX [17, 10, 50].

Chapter 6

Conclusion

Plasma confined by a magnetic dipole is subject to interchange instabilities for sufficiently steep density and temperature profiles. In the laboratory, these profiles are driven unstable by microwave heating of the electrons at a resonance layer. With sufficient collisionality, these plasmas exhibit hallmarks of a turbulent system including complex dynamics and short spatial coherence. The magnetosphere, while generally not turbulent, undergoes similar interchange motions driven by the solar wind. These motions are regulated (to a degree) by field aligned currents which couple the magnetosphere and ionosphere, resistively damping the plasma convection. The experiments described in this work were performed on the CTX device, which has no field aligned currents due to an insulating casing on the magnet. The effects of these currents were "added" by inserting a biasing electrode to regulate the turbulent interchange motions. This thesis reports the first use of local current-collection feedback to modify, amplify, and suppress interchange fluctuations in a dipole confined plasma. Various experiments were performed to test the nature of this feedback mechanism and the response of the plasma. A gyro-fluid model was also developed and included a representation of the feedback system. The related global linear eigensystem displayed a response to current injection feedback with some agreement with experimental observations.

6.1 Discussion of Results

A feedback system is composed of a sensor, electrode (actuator) and feedback circuit (control law). For all experiments reported here, the sensor was a radially adjustable floating potential probe and the electrode was a large diameter biasing probe. A feedback circuit was designed and fabricated consisting of a pre-amplifier/buffer, high-pass filter, phase shifting elements and a four-quadrant power amplifier. With this feedback system a variety of experiments were performed:

- **Feedforward**. Open-loop tests of the plasma response to current injection were performed. The electrode was driven with a known signal and the spectrum of the fluctuations was measured at various points in the plasma. The system launched a wave at the driven frequency which decayed with increased azimuthal separation.

- **Triggered Feedback**. Feedback (closed-loop) was triggered on and off with the circuit phased for peak amplification or peak suppression. The RMS fluctuations of the plasma were observed to be amplified or suppressed by ±30%. Fluctuations returned to the levels without feedback in under 20 μs when the feedback was switched off.

- **Phase Scans**. By performing feedback with varied applied phase shift, dramatic modification to the turbulent spectrum was measured. Significant amplification was observed for phase shifts close to 0°, while broadband suppression occurred closer to 180°. The dominant mode frequency also varied with applied phase.

- **Gain Scans**. Gain scans were performed by tuning the feedback circuit for peak amplification and suppression while adjusting the gain, effectively varying the gain from $-4 \rightarrow 4$. It was observed that for increasing positive gain we saw increasing amplification, while more negative gain resulted in suppression. This was described in terms of a "power flow" model where changing the phase and gain of the feedback circuit effectively changes the sign and magnitude of the system's conductance. *During positive feedback the plasma acts as a load, while with negative feedback the plasma acts as a generator*.

- **Turbulent Decorrelation of Feedback**. By observing the effects of feedback globally, we observe the influence to be limited to roughly two turbulent correlation lengths from the electrode in the electron drift direction. This was observed with multiple identical floating potential probes at various azimuthal positions as well as with the Polar Imager array. This effect of separation was seen in the changing RMS levels with feedback, as well as the modified correlation of the plasma. *We find that the feedback is a localized effect, and that positive feedback increases the local correlation, while negative feedback reduces it.* Additionally, the relative position and orientation of the sensor and electrode were varied. Increased separation reduces the influence of the feedback and again the effect is only observed in the direction of mode rotation.

- $J = 0$ **Feedback**. A comparison was made between the response to a feedback system where the circuit completed through the walls of the vacuum chamber or the circuit completed through an electrode 180° degrees away such that the net current injected into the plasma was zero. The response to both circuits was similar, indicating the feedback mechanisms were the same.

- **High-Pass Filtered Feedback**. By increasing the corner frequency of the high-pass filter, we could effectively apply feedback only to the higher frequency (smaller scale) spectrum of the turbulence. In doing so we could inject energy at smaller scales and attempted to observe an active driving of the inverse energy cascade. Though the feedback did drive only higher frequencies, no change to the low frequency portion of the spectrum (aggregate) was observed.

- **Gyro-Fluid Model**. A gyro-fluid model for the plasma and feedback system was conceived and the related global linear eigenvalue problem was solved. The eigenmodes produced by this model were similar to the experimentally observed modes in dipole-confined plasma. For a reasonable set of parameters, modes were found with growth rates and rotation frequencies similar to those measured in CTX. By performing scans of gain and phase of the current

injection terms, the response to feedback could also be compared to the experiment. While there was some agreement between the model and measurement, not all features were accurately captured. A nonlinear model is required for a complete understanding of the effects of current injection feedback on these turbulent plasmas.

6.2 Questions and Opportunities for Continued Research

While many facets of current injection feedback in dipole confined plasmas were explored in this thesis, there are even more experiments the author, if given infinite time and funding, would enjoy exploring. Here are listed a few areas where more study would help develop a more complete understanding of this method of controlling turbulence:

- **Additional Testing with the Sensor/Electrode Parameters**. While the sensor and electrode positions were varied significantly during these experiments, there are many possibilities left untested. A few example are; a sensor that measured density instead of potential could have an stronger effect on the density fluctuations. An electrode that was a "hot wire" which could actually act as a source of electrons (instead of simply a sink). Using the equatorial biasing array as a sensor or actuator (or both) would allow for feedback at the inner plasma boundary. The tips of the newly installed Rake array could be used for further $J = 0$ experimentation with nearby injecting/collecting electrodes. The effects of radial separation between the sensor and electrode could be explored in detail by radially adjusting the probes.

- **Multi-Point Feedback for Global Suppression**. As mentioned, the influence of feedback is localized. By installing additional sensors and electrodes, the effects of this localized feedback could be used to globally suppress turbulence in the system. These feedback systems could be independent (multiple versions of the current system), or could be connected by an FPGA controller for coordinated multi-point feedback (MIMO).

- **Current-Injection Feedback in a Nonlinear Gyro-Fluid Simulation**. Turbulent systems are highly nonlinear, and the comparison to a linear model, while a good initial step, is missing crucial physics of the system. An existing nonlinear simulation of these plasmas has been used to investigate interchange dynamics in dipole-confined plasmas. The integration of a representation of the current-collection feedback into this model could be an interesting and useful simulation study. Appendix H is an overview of this simulation for the interested reader.

- **Feedback in a Closed Field Line Configuration**. CTX, as a mechanically supported dipole, has open field lines which result in significant parallel losses of particles due to pitch-angle scattering. LDX, which is a levitated coil, allows particles to pass through the dipole drastically reducing losses. In LDX, the effects of feedback on the dominant loss mechanism of radial transport could be studied. By suppressing the turbulent fluctuations at the edge, would transport be reduced? Would confinement improve, resulting in higher plasma density? This could be explored by applying this nature of feedback to LDX plasmas.

Bibliography

[1] L Spitzer. The stellarator concept. *Physics of Fluids*, 1958.

[2] B Rose, A E Taylor, and E Wood. Measurement of the Neutron Spectrum from Zeta. *Nature*, 181(4624):1630–1632, June 1958.

[3] G Paschmann. Auroral Plasma Physics. 2003.

[4] Y S Yang, R A Wolf, R W Spiro, T W Hill, and A J Dessler. Numerical simulation of torus-driven plasma transport in the Jovian magnetosphere. *Journal of Geophysical Research: Space Physics (1978–2012)*, 99(A5):8755–8770, May 1994.

[5] Frank Toffoletto, Stanislav Sazykin, Robert Spiro, and Richard Wolf. Inner Magnetospheric Modeling with the Rice Convection Model. *Advances in Space Environment Research*, pages 175–196, January 2003.

[6] R A Wolf, R W Spiro, S Sazykin, and F R Toffoletto. How the Earth's inner magnetosphere works: An evolving picture. *Journal of Atmospheric and Solar-Terrestrial Physics*, 69(3):288–302, March 2007.

[7] K Birkeland. *Archives des Sciences Physiques et Naturelles*. page p. 497.

[8] I F Shaikhislamov, V M Antonov, Yu P Zakharov, E L Boyarintsev, A V Melekhov, V G Posukh, and A G Ponomarenko. Field-aligned currents and magnetospheric generator in experiments on a laser-produced plasma flowing around a magnetic dipole. *Cosmic Research*, 52(4):278–288, July 2014.

[9] H P Warren and M E Mauel. Observation of Chaotic Particle Transport Induced by Drift-Resonant Fluctuations in a Magnetic Dipole Field. *Physical Review Letters*, 74(8):1351–1354, February 1995.

[10] B Levitt, D Maslovsky, and M E Mauel. Measurement of the global structure of interchange modes driven by energetic electrons trapped in a magnetic dipole. *Physics of Plasmas*, 9(6):2507, 2002.

[11] B Levitt, D Maslovsky, M E Mauel, and J Waksman. Excitation of the centrifugally driven interchange instability in a plasma confined by a magnetic dipolea). *Physics of Plasmas (1994-present)*, 12(5):055703, May 2005.

[12] D Maslovsky, B Levitt, and M Mauel. Observation of Nonlinear Frequency-Sweeping Suppression with rf Diffusion. *Physical Review Letters*, 90(18):185001, May 2003.

[13] B A Grierson, M W Worstell, and M E Mauel. Global and local characterization of turbulent and chaotic structures in a dipole-confined plasmaa). *Physics of Plasmas (1994-present)*, 16(5):055902, May 2009.

[14] B A Grierson, M E Mauel, M W Worstell, and M Klassen. Transport Induced by Large Scale Convective Structures in a Dipole-Confined Plasma. *Physical Review Letters*, 105(20):205004, November 2010.

[15] A C Boxer, R Bergmann, J L Ellsworth, D T Garnier, J Kesner, M E Mauel, and P Woskov. Turbulent inward pinch of plasma confined by a levitated dipole magnet. *Nature Physics*, 6(3):207–212, March 2010.

[16] Matthew S Davis, M E Mauel, Darren T Garnier, and Jay Kesner. Pressure profiles of plasmas confined in the field of a magnetic dipole. *Plasma Physics and Controlled Fusion*, 56(9):095021, September 2014.

[17] M E Mauel. Laboratory Observations of Wave-Induced Radial Transport within an. *Le Journal de Physique IV*, 07(C4):C4–307–C4–318, October 1997.

[18] L D Landau. Mechanics: Volume 1 (Course Of Theoretical Physics) Author: LD Landau, EM Lifshitz, Publisher: Butterwor, 1976.

[19] J P Freidberg. Ideal magnetohydrodynamics. 1987.

[20] J D Jackson. Classical Electrodynamics, 1962.

[21] M N Rosenbluth and C L Longmire. Stability of plasmas confined by magnetic fields. *Annals of Physics*, 1(2):120–140, May 1957.

[22] D B Melrose. Rotational effects on the distribution of thermal plasma in the magnetosphere of jupiter. *Planetary and Space Science*, 15(2):381–393, February 1967.

[23] Michael C Kelley, Jonathan J Makela, Odile de La Beaujardière, and John Retterer. CONVECTIVE IONOSPHERIC STORMS: A REVIEW. *Reviews of Geophysics*, 49(2), June 2011.

[24] Michael E Brown and Antonin H Bouchez. The Response of Jupiter's Magnetosphere to an Outburst on Io. *Science*, 278(5336):268–271, October 1997.

[25] N André, A M Persoon, J Goldstein, J L Burch, P Louarn, G R Lewis, A M Rymer, A J Coates, W S Kurth, E C Sittler, M F Thomsen, F J Crary, M K Dougherty, D A Gurnett, and D T Young. Magnetic signatures of plasma-depleted flux tubes in the Saturnian inner magnetosphere. *Geophysical Research Letters*, 34(14), July 2007.

[26] Fabien Darrouzet, Dennis L Gallagher, Nicolas André, Donald L Carpenter, Iannis Dandouras, Pierrette M E Décréau, Johan De Keyser, Richard E Denton, John C Foster, Jerry Goldstein, Mark B Moldwin, Bodo W Reinisch, Bill R Sandel, and Jiannan Tu. Plasmaspheric Density Structures and Dynamics: Properties Observed by the CLUSTER and IMAGE Missions. In *The Earth's Plasmasphere*, pages 55–106. Springer New York, January 2009.

[27] O E Garcia, R A Pitts, J Horacek, J Madsen, V Naulin, A H Nielsen, and J Juul Rasmussen. Collisionality dependent transport in TCV SOL plasmas. *Plasma Physics and Controlled Fusion*, 49(12B):B47, December 2007.

[28] D A D'Ippolito, J R Myra, and S J Zweben. Convective transport by intermittent blob-filaments: Comparison of theory and experiment. *Physics of Plasmas*, 18(6):060501, 2011.

[29] D T Garnier, A Hansen, M E Mauel, E Ortiz, A C Boxer, J Ellsworth, I Karim, J Kesner, S Mahar, and A Roach. Production and study of high-beta plasma confined by a superconducting dipole magnet. *Physics of Plasmas*, 13(5):056111, 2006.

[30] K Rypdal, H Fredriksen, J V Paulsen, and O M Olsen. Coherent structures in the turbulent equilibrium of the simple magnetized torus. *Physica Scripta*, 1996(T63):167, January 1996.

[31] L Federspiel, B Labit, P Ricci, A Fasoli, I Furno, and C Theiler. Observation of a critical pressure gradient for the stabilization of interchange modes in simple magnetized toroidal plasmas. *Physics of Plasmas (1994-present)*, 16(9):092501, September 2009.

[32] Th Pierre, A Escarguel, D Guyomarc'h, R Barni, and C Riccardi. Radial Convection of Plasma Structures in a Turbulent Rotating Magnetized-Plasma Column. *Physical Review Letters*, 92(6):065004, February 2004.

[33] B Levitt, D Maslovsky, and M Mauel. Observation of Centrifugally Driven Interchange Instabilities in a Plasma Confined by a Magnetic Dipole. *Physical Review Letters*, 94(17):175002, May 2005.

[34] M C Kelley, T L Franz, and G Prasad. On the turbulent spectrum of equatorial spread F: A comparison between laboratory and space results. *Journal of Geophysical Research: Space Physics (1978–2012)*, 107(A12):SIA 5–1–SIA 5–6, December 2002.

[35] C Theiler, I Furno, J Loizu, and A Fasoli. Convective Cells and Blob Control in a Simple Magnetized Plasma. *Physical Review Letters*, 108(6):065005, February 2012.

[36] J Callen. Drift-Wave Turbulence Effects on Magnetic Structure and Plasma Transport in Tokamaks. *Physical Review Letters*, 39(24):1540–1543, December 1977.

[37] Amiya K Sen. Observability and controllability of plasma instabilities. *Physics of Fluids (1958-1988)*, 18(9):1187–1191, September 1975.

[38] A K Sen. Control and diagnostic uses of feedback. *Physics of Plasmas (1994-present)*, 7(5):1759–1766, May 2000.

[39] T Simonen, T Chu, and H Hendel. Feedback Control of Collisional Drift Waves by Modulated Parallel-Electron-Current Sink-Experiment and Interpretation. *Physical Review Letters*, 23(11):568–571, September 1969.

[40] Alexander J Klein, David A Maurer, Thomas Sunn Pedersen, Michael E Mauel, Gerald A Navratil, Cory Cates, Mikhail Shilov, Yuhong Liu, Nikolai Stillits, and Jim Bialek. Suppression of rotating external kink instabilities using optimized mode control feedback. *Physics of Plasmas (1994-present)*, 12(4):040703, April 2005.

[41] N Rath, S Angelini, J Bialek, P J Byrne, B DeBono, P Hughes, J P Levesque, M E Mauel, G A Navratil, Q Peng, D Rhodes, and C Stoafer. Adaptive control of rotating magnetic perturbations in HBT-EP using GPU processing. *Plasma Physics and Controlled Fusion*, 55(8):084003, August 2013.

[42] Ronald Prater. Feedback Suppression of a Large-Growth-Rate Flute Mode. *Physical Review Letters*, 27(3):132–135, July 1971.

[43] T Uckan, B Richards, A J Wootton, Roger D Bengtson, R Bravenec, B A Carreras, G X Li, P Hurwitz, P E Phillips, W L Rowan, H Y W Tsui, J R Uglum, Y Wen, and D Winslow. Feedback control and stabilization experiments on the Texas Experimental Tokamak (TEXT). *Journal of Nuclear Materials*, 220-222:663–667, April 1995.

[44] T Uckan, B Richards, R D Bengtson, B A Carreras, Guoxiang Li, P D Hurwitz, W L Rowan, H Y W Tsui, and A J Wootton. Plasma edge turbulence probing and feedback control and stabilization experiments. *Nuclear Fusion*, 35(4):487, April 1995.

[45] B Richards, T Uckan, A J Wootton, B A Carreras, Roger D Bengtson, P Hurwitz, G X Li, H Lin, W L Rowan, H Y W Tsui, A K Sen, and J Uglum. Modification of tokamak edge turbulence using feedback. *Physics of Plasmas*, 1(5):1606, 1994.

[46] Benjamin Joseph Levitt. Global mode analysis of centrifugal and curvature driven interchange instabilities, 2004.

[47] E E Ortiz, A C Boxer, J L Ellsworth, D T Garnier, A K Hansen, I Karim, J Kesner, and M E Mauel. Effects of the Hot Electron Interchange Instability on Plasma Confined in a Dipolar Magnetic Field. *Journal of Fusion Energy*, 26(1-2):139–144, June 2007.

[48] H Saitoh, Z Yoshida, J Morikawa, Y Yano, H Mikami, N Kasaoka, and W Sakamoto. Observation of magnetic fluctuations and rapid density decay of magnetospheric plasma in Ring Trap 1. *Physics of Plasmas (1994-present)*, 19(6):064502, June 2012.

[49] Robert J Goldston and Paul H Rutherford. *Introduction to Plasma Physics*. IOP Publishing Ltd, 1995.

[50] Brian Adam Grierson. Interchange turbulence in a dipole-confined plasma, 2009.

[51] M J Burin, G R Tynan, G Y Antar, N A Crocker, and C Holland. On the transition to drift turbulence in a magnetized plasma column. *Physics of Plasmas*, 12(5):052320, 2005.

[52] Akira Hasegawa and Masahiro Wakatani. Self-organization of electrostatic turbulence in a cylindrical plasma. *Physical Review Letters*, 59(14):1581–1584, October 1987.

[53] Matthew Wales Worstell. Symmetry Breaking and the Inverse Energy Cascade in a Plasma. Columbia University, 2013.

[54] John Bechhoefer. Feedback for physicists: A tutorial essay on control. *Reviews of Modern Physics*, 77(3):783–836, August 2005.

[55] R Mancini. Op Amps for everyone. *Texas Instruments*, 2002.

[56] K Lacanette. *A Basic Introduction to Filters-Active, Passive, and Switched-Capacitor*. National Semiconductor Corporation, April 1991.

[57] H Zumbahlen. Allpass Filters. *Analog Devices*.

[58] H Tennekes and J L Lumley. *A First Course in Turbulence*. 1972.

[59] P Welch. The use of fast Fourier transform for the estimation of power spectra: A method based on time averaging over short, modified periodograms. *IEEE Transactions on Audio and Electroacoustics*, 15(2):70–73, June 1967.

[60] J Kesner. Interchange modes in a collisional plasma. *Physics of Plasmas*, 7(10):3837, 2000.

[61] J Kesner and R J Hastie. Electrostatic drift modes in a closed field line configuration. *Physics of Plasmas (1994-present)*, 9(2):395–400, February 2002.

[62] Paolo Ricci, B N Rogers, W Dorland, and M Barnes. Gyrokinetic linear theory of the entropy mode in a Z pinch. *Physics of Plasmas*, 13(6):062102, 2006.

[63] Michael Mauel. Toroidal Confinement without Parallel Current: Interchange and Entropy Modes in a Warm Electron Dipole Plasma. pages 1–15, March 2015.

[64] Sumire Kobayashi, Barrett N Rogers, and William Dorland. Particle Pinch in Gyrokinetic Simulations of Closed Field-Line Systems. *Physical Review Letters*, 105(23):235004, December 2010.

[65] A H Boozer. Guiding center drift equations. *Physics of Fluids*, 1980.

[66] Steven T Zalesak. Fully multidimensional flux-corrected transport algorithms for fluids. *Journal of Computational Physics*, 31(3):335–362, June 1979.

Appendix A

CTX Parameters

The magnetic field of CTX is approximately dipolar for the experimental regions investigated in this thesis. Figure A.1 plots the magnetic field strength at the equatorial plane as given by Equation 2.1 in green. The magnetic flux is plotted in light blue. Orange shows the differential flux tube volume with radius, Equation 2.6. Notice the magnetic field falls off like $1/r^3$ (magnetic flux like $1/r$), and the flux tube volume increases as r^4. The inner boundary of the plasma on the magnet housing is roughly at r = 21 cm, while the outer boundary is close to 68 cm.

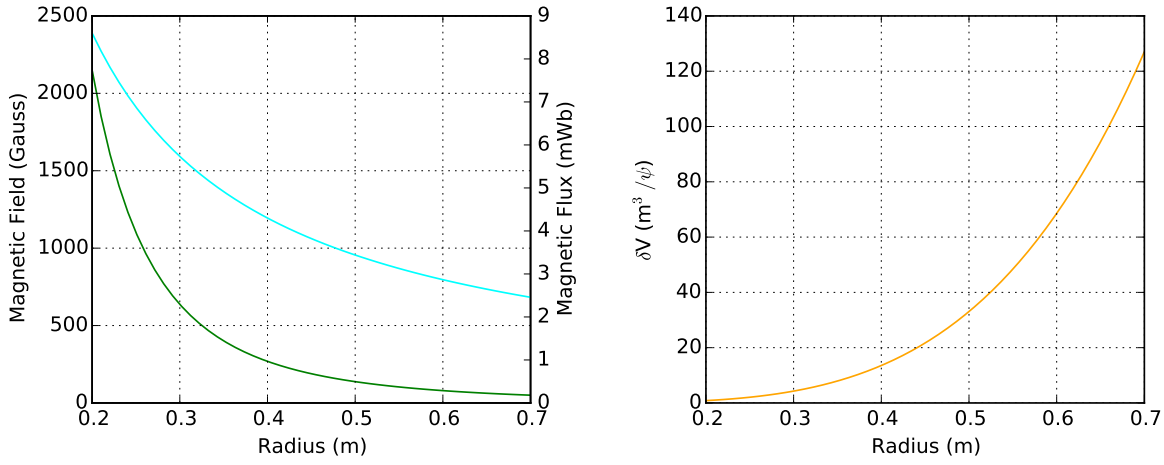

Figure A.1: Left: The equatorial magnetic field strength (green), the magnetic flux (blue). Right: The differential flux tube volume increase like r^4.

Figure A.2 plots the gyro frequency (Equation 1.1) and radius for electrons on the left, ion on

the right. The equation for the gyro radius is assumed from the particle energy:

$$\rho = \frac{v_t}{\omega_c} \tag{A.1}$$

In Figure A.2, $T_e = 25$ eV and $T_i = 1$ eV. These curves change as the temperatures change. Resonance with the microwaves occurs near 27 cm. For the experimental regions of this thesis, the electron have a gyro radius of ~ 4 mm, while the ions gyro radius is closer to an inch.

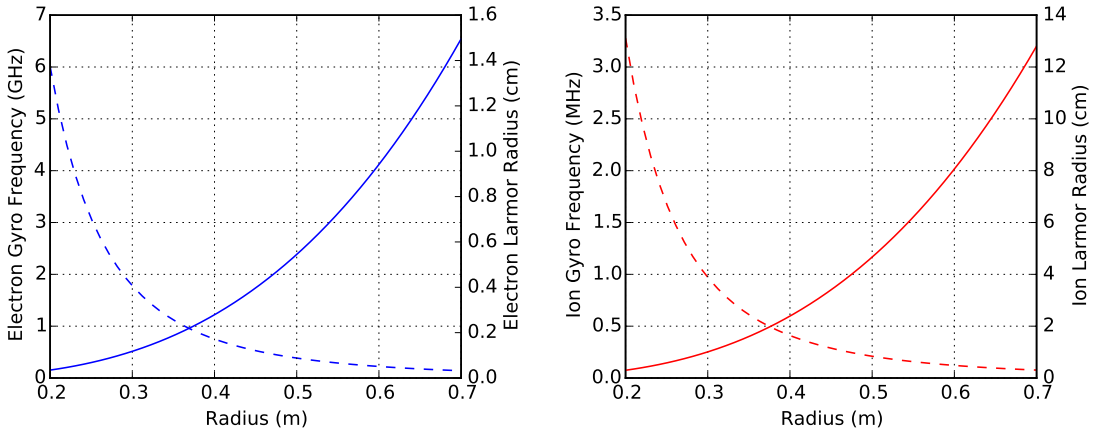

Figure A.2: Electron and ion gyro frequencies (dashed) and Larmor radii (solid) with radius. The electron gyro frequency is resonant with the microwaves near to 27 cm.

We can approximate the bounce frequency of the particles by dividing the thermal velocities of each species by the length of a field line,

$$\omega_b = 2\pi f_b = 2\pi v_t \Big[\int_0^\pi R \sin^2\theta \Big]^{-1} = 2\pi \frac{v_{t,e}}{\pi R/2} = 4\frac{v_{t,e}}{R} \tag{A.2}$$

Figure A.3 plots this values for electrons on the left and ions on the right. We see the electrons are significantly above the band of our turbulent dynamics (MHz), while the ions are bouncing well within the audio range. This is clearly a very rough estimate of the actual bounce frequency which depends on the pitch angle of the particle.

From these values we see that $\omega_c >> \omega_B$, for both the ions and electrons, though the bounce frequency of the electrons is faster than the ion cyclotron frequency. As such, in a flux tube, the rapid motion of the electrons neutralizes any charge imbalance, leaving the flux tube at the same

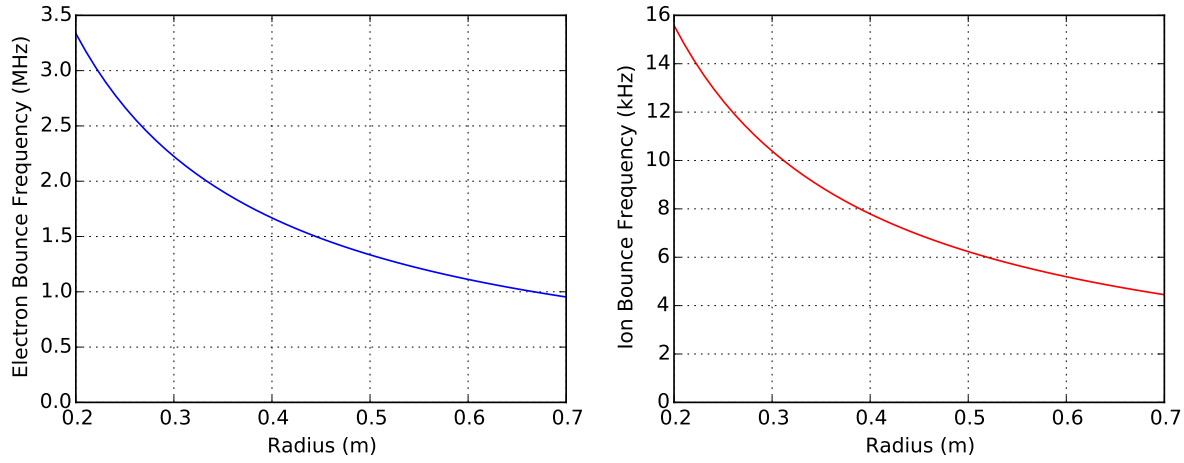

Figure A.3: Approximated bounce frequency for electrons (left) and ions (right).

potential at every location ($E_{\|} \approx 0$).

Azimuthal drifts of particles in a dipole field arise from curvature of the field lines, gradients of the magnetic field strength, and electric fields. We estimate the electron drift in CTX using a guiding center Hamiltonian [65], where the drift frequency is given as the velocity in the periodic coordinate:

$$\omega_d = \frac{3c}{e}\frac{\mu B}{\psi} \tag{A.3}$$

At the cyclotron resonance, taking $T_e = 50$ eV, B = 875 Gauss, and the magnetic flux $\psi = 6\times10^5$ Maxwells, we find the magnetic moment $\mu = kT_e/B = 9 \times 10^{-14}$ ergs/Gauss. From Equation A.3, we find $\omega_d = 2\pi\ 4 \times 10^3$ rads/s, or a drift frequency of 4 kHz. From these very rough estimates, for electrons in CTX, $\omega_c >> \omega_B >> \omega_d$. As a result, when looking at the dynamics of the interchange turbulence of interest to this thesis, it is reasonable to ignore the dynamics of the gyration and bounce of the particles along field lines.

The Debye length is an important parameter is plasmas related to the ability of a plasma to shield imposed electric fields. In CTX, for electron temperature of 25 eV and density of 10^{16} m^{-3},

$$\lambda_D = \sqrt{\frac{\epsilon_0 T_e}{e^2 n_0}} \approx 7440\sqrt{\frac{T_e}{n_0}} = .372\text{mm} \tag{A.4}$$

Appendix B

Dipole Coordinates

Dipole coordinates are a simplified branch of magnetic coordinates which only consider a poloidal field [52]. Although simplified, understanding the transformation from Cartesian coordinates has some subtleties. The most direct approach uses "generalized" coordinates to establish an orthogonal bias. Methods from generalized coordinates allow one to find operators like curl and gradient in a different coordinate system easily. The following sections explain the basics of generalized coordinates going though an example, then goes through the necessary derivations to arrive at the magnetic coordinates of a dipole field.

B.1 Intro to Generalized Coordinates

Cartesian coordinates, (x, y, z), are the simplest and most intuitive coordinate system. We can use these coordinates to describe any three dimensional vector field, but in many cases this can become complicated. Some systems are more easily represented by a different set of coordinates. For example, a charged particle's helical trajectory on a straight magnetic field line would be simplest to describe in a cylindrical coordinate system. This subsection explains some of the basic properties of generalized coordinates following some very clear notes by Qian Peng.

We can generally describe a point in space, $\vec{X}$, in a coordinate system (u_1, u_2, u_3) as:

$$\vec{X}(u_1, u_2, u_3) = \begin{cases} x(u_1, u_2, u_3)\hat{x} \\ y(u_1, u_2, u_3)\hat{y} \\ z(u_1, u_2, u_3)\hat{z} \end{cases}$$

To describe this vector we need a basis. There are two bases we can use, the tangent basis and the gradient basis. Each is useful in certain situations. We find the tangent basis as:

$$\vec{e}_1 = \frac{\partial \vec{X}}{\partial u^1}, \qquad \vec{e}_2 = \frac{\partial \vec{X}}{\partial u^2}, \qquad \vec{e}_3 = \frac{\partial \vec{X}}{\partial u^3} \tag{B.1}$$

Using the tangent vectors, we can define several important quantities. First, the covariant metric tensor is defined by:

$$g_{ij} \equiv \vec{e}_i \cdot \vec{e}_j \qquad \text{covariant metric tensor} \tag{B.2}$$

and from this the Jacobian is found:

$$J = \vec{e}_1 \cdot (\vec{e}_2 \times \vec{e}_2), \qquad J^2 = \det |g_{ij} \cdot g^{ij}| = g \tag{B.3}$$

and therefore $J = \sqrt{g}$. The gradient basis is obtained by considering the gradient of a scalar field f. If we dot this gradient with our tangent vectors, we get:

$$\vec{e}_i \cdot \nabla f = \frac{\partial f}{\partial u^i} \tag{B.4}$$

if we take $f = u^j$, we find:

$$\vec{e}_i \cdot \nabla u^j = \frac{\partial u^j}{\partial u^i} = \delta_{ij} \tag{B.5}$$

where we define our gradient basis as ∇u^j. From these, we can find the contravariant metric

tensor as $g^{ij} = \nabla u^i \cdot \nabla u^j$.

We can now expand a vector in this coordinate system in two bases:

$$\vec{A} = A^i \vec{e}_i = A_i \nabla u^i \tag{B.6}$$

and by definition, dotting with either a tangent vector or gradient vector yields either the covariant or contravariant coefficient:

$$A_i = \vec{A} \cdot \vec{e}_i, \qquad A^i = \vec{A} \cdot \nabla u^i \tag{B.7}$$

These representations will prove to be valuable when deciding how to represent operators in these bases. Note that the gradient basis should be unique if the tangent basis is given. The metric tensors can be used to transform from the tangent and gradient basis as $\vec{e}_i = g_{ij} \cdot \nabla u^j$, and vise versa $\nabla u^i = g^{ij} \cdot \vec{e}_j$. Also note,

$$\epsilon_{ijk} \frac{\vec{e}_k}{\sqrt{g}} = \nabla u^i \times \nabla u^j \qquad \nabla u^i = \epsilon_{ijk} \frac{\vec{e}_j \times \vec{e}_k}{\sqrt{g}} \tag{B.8}$$

Using the properties of these basis vectors, we can now discuss the operators for gradient, divergence and curl in general form. The gradient is simple. As we defined the gradient basis vectors using the example of scalar field f, the gradient is best given by the contravariant form:

$$\nabla f = \frac{\partial f}{\partial u^i} \nabla u^i \tag{B.9}$$

Things get slightly trickier when we consider the divergence operator. If one takes note that $\nabla u^i \times \nabla u^j = \nabla \times (u^i \nabla u^j) = \frac{\vec{e}_k}{\sqrt{g}} \epsilon_{kij}$, we can see it makes sense to use the covariant form for divergence:

$$\nabla \cdot \vec{A} = \nabla \cdot \left(A^i \sqrt{g} \frac{\vec{e}_i}{\sqrt{g}} \right) = \frac{\vec{e}_i}{\sqrt{g}} \cdot \nabla (\sqrt{g} A^i) = \frac{1}{\sqrt{g}} \frac{\partial (\sqrt{g} A^i)}{\partial u^i} \tag{B.10}$$

Similarly, if we use the fact that the curl of a gradient is zero (hence the curl of a gradient vector is zero), the curl operator is easiest to find using the contravariant form for $\vec{A}$:

$$\nabla \times \vec{A} = \nabla \times (A_i \nabla u^i) = \nabla A_i \times \nabla u^i = \frac{\partial A_i}{\partial u^j} \nabla u^j \times \nabla u^i = \frac{\partial A_i}{\partial u^j} \epsilon_{jik} \frac{\vec{e}_k}{\sqrt{g}} = \frac{1}{\sqrt{g}} \epsilon_{ijk} \frac{\partial A_i}{\partial u^j} \vec{e}_k \tag{B.11}$$

B.1.1 Test it out: Spherical Coordinates

Now we'll use generalized coordinates to reproduce something familiar, operators in spherical coordinates. First we define the transformation to spherical from Cartesian:

$$x = r\cos\varphi\sin\theta, \qquad y = r\sin\varphi\sin\theta, \qquad z = r\cos\theta \tag{B.12}$$

$$\vec{x} = x\hat{x} + y\hat{y} + z\hat{z} = r\cos\varphi\sin\theta\hat{x} + r\sin\varphi\sin\theta\hat{y} + r\cos\theta\hat{z} \tag{B.13}$$

Now we find the tangent vectors:

$$\vec{e_r} = \frac{\partial \vec{x}}{\partial r} = \cos\varphi\sin\theta\hat{x} + \sin\varphi\sin\theta\hat{y} + \cos\theta\hat{z} \tag{B.14}$$

$$\vec{e_\theta} = \frac{\partial \vec{x}}{\partial \theta} = r\cos\varphi\cos\theta\hat{x} + r\sin\varphi\cos\theta\hat{y} - r\sin\theta\hat{z} \tag{B.15}$$

$$\vec{e_\varphi} = \frac{\partial \vec{x}}{\partial \varphi} = -r\sin\varphi\sin\theta\hat{x} + r\cos\varphi\sin\theta\hat{y} \tag{B.16}$$

From the tangent vectors we build the metric tensor,

$$g_{rr} = \vec{e_r} \cdot \vec{e_r} = 1 \tag{B.17}$$

$$g_{\theta\theta} = \vec{e_\theta} \cdot \vec{e_\theta} = r^2 \tag{B.18}$$

$$g_{\varphi\varphi} = \vec{e_\varphi} \cdot \vec{e_\varphi} = r^2\sin^2\theta \tag{B.19}$$

where all the off-diagonal elements are zero as the bias vectors are orthogonal. From this we get:

$$g_{ij} = \begin{bmatrix} 1 & 0 & 0 \\ 0 & r^2 & 0 \\ 0 & 0 & r^2 \sin^2\theta \end{bmatrix}$$

and as the matrix is diagonal, the contravariant metric tensor is given by the reciprocal of the diagonal elements,

$$g^{ij} = \begin{bmatrix} 1 & 0 & 0 \\ 0 & r^{-2} & 0 \\ 0 & 0 & (r^2 \sin^2\theta)^{-1} \end{bmatrix}$$

As such, we can find the Jacobian as:

$$J = \sqrt{g} = \sqrt{g_{ij} \cdot g^{ij}} = r^2 \sin\theta \tag{B.20}$$

and we can use this to find the gradient vectors from the tangent vectors as:

$$\nabla\varphi = \frac{\vec{e}_r \times \vec{e}_\theta}{\sqrt{g}} = \frac{1}{r^2 \sin\theta}\Big[- r\sin\varphi\hat{x} + r\cos\varphi\hat{y}\Big] \tag{B.21}$$

$$\nabla\theta = \frac{\vec{e}_\varphi \times \vec{e}_r}{\sqrt{g}} = \frac{1}{r^2 \sin\theta}\Big[r\cos\varphi\sin\theta\cos\theta\hat{x} + r\sin\varphi\sin\theta\cos\theta\hat{y} - r\hat{z}\Big] \tag{B.22}$$

$$\nabla r = \frac{\vec{e}_\theta \times \vec{e}_\varphi}{\sqrt{g}} = \frac{1}{r^2 \sin\theta}\Big[r^2\sin^2\theta\cos\varphi\hat{x} + r^2\sin^2\theta\sin\varphi\hat{y} - r\sin^2\theta\cos\theta\hat{z}\Big] \tag{B.23}$$

We can now derive operators in spherical coordinates. As an example, the Laplacian:

$$\nabla^2 f = \nabla\cdot(\nabla f) = \nabla\cdot\Big(\frac{\partial f}{\partial u^i}\nabla u^i\Big) = \nabla\cdot\Big(\frac{\partial f}{\partial u^i}g^{ij}\vec{e}_j\Big) = \frac{1}{\sqrt{g}}\frac{\partial}{\partial u^i}\Big(\sqrt{g}g^{ij}\frac{\partial f}{\partial u^i}\Big) \tag{B.24}$$

where the term in parenthesis is given as,

$$g^{ij}\frac{\partial f}{\partial u^i} = \begin{bmatrix} \frac{\partial f}{\partial r} \\ \frac{1}{r^2}\frac{\partial f}{\partial \theta} \\ \frac{1}{r^2\sin^2\theta}\frac{\partial f}{\partial \varphi} \end{bmatrix}$$

and we arrive at the correct expression:

$$\nabla^2 f = \frac{1}{\sqrt{g}}\frac{\partial}{\partial u^i}\begin{bmatrix} \frac{\partial f}{\partial r} \\ \frac{1}{r^2}\frac{\partial f}{\partial \theta} \\ \frac{1}{r^2\sin^2\theta}\frac{\partial f}{\partial \varphi} \end{bmatrix} = \frac{1}{r^2}\frac{\partial}{\partial r}\Big(r^2\frac{\partial f}{\partial r}\Big) + \frac{1}{r^2\sin\theta}\frac{\partial}{\partial \theta}\Big(\sin\theta\frac{\partial f}{\partial \theta}\Big) + \frac{1}{r^2\sin^2\theta}\frac{\partial^2 f}{\partial \varphi^2}$$

B.2 Generalized Coordinates to Dipole Coordinates

The magnetic field from a point dipole is well known [20] to have radial and polar dependence as:

$$\vec{B} = -\frac{2M}{r^3}\cos\theta\hat{r} - \frac{M}{r^3}\sin\theta\hat{\theta}, \qquad |\vec{B}| = \frac{M}{r^3}\sqrt{1+3\cos^2\theta} \tag{B.25}$$

As the magnetic flux, ψ, is the surface integral of the magnetic field, and $B = \nabla \times \vec{A}$, where $\vec{A}$ is the magnetic vector potential, following Hasegawa [52],

$$\psi = \oint \vec{B}\cdot d\vec{S} = \oint (\nabla\times\vec{A})\cdot d\vec{S} = \oint \vec{A}\cdot d\vec{l} = 2\pi r\sin\theta A_\varphi \tag{B.26}$$

where the vector potential only has a $-\hat{\varphi}$ components as the dipole field has no toroidal field. From this, we can express the magnetic field in terms of flux by:

$$\vec{B} = \nabla\times(-A_\varphi\hat{\varphi}) = -\nabla\times\frac{\psi}{2\pi r\sin\theta}\hat{\varphi} = \frac{1}{2\pi}\nabla\varphi\times\nabla\psi \tag{B.27}$$

Note that this expression still allows $\nabla\cdot\vec{B} = 0$. Finally, we use the fact that the cross product of two gradient can be expressed as the gradient of a third,

$$\vec{B} = \nabla\varphi \times \nabla\psi = \nabla\chi \tag{B.28}$$

Note the factor of 2π from the azimuthal integration is dropped, which is the convention used in this thesis. The quantity χ is referred to as the magnetic scalar potential is related to position along a field line. These scalar fields and and their gradients are given as:

$$\psi = \frac{M}{r}\sin^2\theta, \qquad \varphi = \varphi, \qquad \chi = \frac{M}{r^2}\cos\theta \tag{B.29}$$

$$\nabla\psi = -\frac{M}{r^2}\sin^2\theta\hat{r} + 2\frac{M}{r^2}\sin\theta\cos\theta\hat{\theta} \tag{B.30}$$

$$\nabla\varphi = \frac{\hat{\varphi}}{r\sin\theta} \tag{B.31}$$

$$\nabla\chi = -\frac{2M}{r^3}\cos\theta\hat{r} - \frac{M}{r^3}\sin\theta\hat{\theta} = \vec{B} \tag{B.32}$$

Note that these are the gradient vector basis for the dipole coordinate system! From this we can find our contravariant metric tensor as:

$$g_{ij} = \begin{bmatrix} \nabla\psi\cdot\nabla\psi & 0 & 0 \\ 0 & \nabla\chi\cdot\nabla\chi & 0 \\ 0 & 0 & \nabla\varphi\cdot\nabla\varphi \end{bmatrix}$$

where $J = \sqrt{g}$ is one over the square root of the determinant of the above matrix:

$$J = \sqrt{g} = (|\nabla\psi||\nabla\chi||\nabla\varphi|)^{-1}$$

and as $B = \nabla\varphi \times \nabla\psi = \nabla\chi$, clearly $J = \frac{1}{|B|^2}$! Given the gradient vectors and the Jacobian, we have the tools for finding the operators in dipole coordinates, some of which are derived in H.

B.3 Dipole Field Lines

We can define a field line as a curve on which any point is aligned with the direction of the field at that point. As such, the ratio of the vector components must match the slope of the field line, or:

$$dl = \frac{dr}{B_r} = \frac{rd\theta}{B_\theta} \tag{B.33}$$

The above can be solved for the equation of a dipole field line in polar coordinates as:

$$\frac{dr}{rd\theta} = \frac{B_r}{B_\theta} \rightarrow r = L\sin^2\theta \tag{B.34}$$

where L is the radius of the field line at the equatorial midplane.

This definition of a field line can be related to our definition of χ simply:

$$B^2 = \vec{B}\cdot\vec{B} = \vec{B}\cdot\nabla\chi = B\frac{d\chi}{dl} \rightarrow dl = \frac{d\chi}{B} \tag{B.35}$$

where as the slope of χ is always in the direction of the magnetic field, the ratio is between $d\chi$ and the total field magnitude.

B.4 Flux Tube Integration

Flux tube volume plays an important role in the dynamics of dipole confined plasmas. We can define the volume of tube of uniform magnetic flux as:

$$V = \int A\cdot dl = \int \frac{\psi}{B}dl = \psi\int\frac{dl}{B} \rightarrow \delta V = \frac{V}{\psi} = \int\frac{dl}{B} \tag{B.36}$$

where δV is the differential volume per unit flux. Combining this with our above definition of dl, we define the differential magnetic flux tube volume as:

$$\delta V(\psi) \equiv \int_{-\infty}^{+\infty}\frac{d\chi}{B^2} \tag{B.37}$$

Flux tube averaging is an integration along field lines over a differential flux tube volume. We perform these averages as the dynamics along the field lines are much faster than the interchange dynamics we are interested in. We can get a better idea of the value of the above integral with a change of variables:

$$\chi = \frac{M}{r^2}\cos\theta = \frac{M}{(\frac{M}{\psi}\sin^2\theta)^2} = \frac{\psi^2\cos\theta}{M\sin^4\theta} \tag{B.38}$$

then we can find an expression for $d\chi$ (taking ψ fixed) as:

$$d\chi = \frac{\partial\chi}{\partial\theta}d\theta = -\frac{\psi^2}{M}\frac{1+3\cos^2\theta}{\sin^5\theta}d\theta \tag{B.39}$$

Next, we find B^2 as:

$$B^2 = \frac{M^2}{r^6}(1+3\cos^2\theta) = \frac{\psi^6(1+3\cos^2\theta)}{M^4\sin^{12}\theta} \tag{B.40}$$

Returning to the integral,

$$\delta V(\psi) = \int_\pi^0 \frac{-\frac{\psi^2}{M}\frac{1+3\cos^2\theta}{\sin^5\theta}d\theta}{\frac{\psi^6(1+3\cos^2\theta)}{M^4\sin^1 2\theta}} = -\frac{M^3}{\psi^4}\int_\pi^0 \sin^7\theta d\theta \tag{B.41}$$

If we take this integral numerically, we find:

$$\delta V(\psi) \approx .91\frac{M^3}{\psi^4} \tag{B.42}$$

With this, we define the flux-tube average of a quantity A as:

$$< A > \equiv \delta V^{-1}\int_{-\infty}^{+\infty}\frac{d\chi A}{B^2} \tag{B.43}$$

Appendix C

CTX Equipment and Running

This section contains information relevant only to someone trying to operate or diagnose a problem on the CTX device. As I received a significant amount of training from the previous graduate students on CTX, it seems only fair to try to pass on what I know to the next generation. These instructions are meant only as a loose guide and a detailed understanding of the equipment should be obtained before attempting operation. That being said, sometimes things just ”work”...

C.1 Starting Up Procedures for Running CTX

This is a brief run down of the necessities to start and run the CTX device. This is how I do them, in order:

1. **Magnet Controls.** Turn on National Instruments SCXI-1000 for magnet power supply control. This is located in the control room on top of the Dell computer. Open the LabVIEW file “Magnet Control.vi” to interact with the magnet controls.

2. **Gas Pressure.** Also in the control room is the hydrogen bottle for gas puffing. This is opened generally with two valves, one on top of the bottle, the other on the regulator. Set the pressure to desired value. Note; this regulator has “creep”. Check it a few minutes after adjustment.

3. **Magnetron Power Supply.** The power supply is located at the bottom of the stairs into the lab. First move the switch on the box marked “Spellman” to the “ON” position. The green standby light should come on. Then move the switch on the power supply for the optical isolation (above the Spellman box) to “AC PWR”. Moving to the blue panel facing the stairs, make sure the central dial is rotated completely counter-clockwise, then press the green power button. Making sure to keep the current (right gauge) under 20 A, *slowly* increase the voltage (left gauge) to 4 V by turning the dial clockwise.

4. **Polar Imager Power.** Near the magnet power supply feed-through are a total of four power supplies for the Polar Imager. An HP 6827A is tuned to bias the detectors to collect ions (-100 V), turn this on. There are two large identical blue and white boxes, one on the floor, the other on the machine (directly above). Flip the switches to power these and a red light should turn on. Finally, there is a small black box marked “Secondary Electron Grid Bias”. Turn this on. Remember to occasionally make sure this bias is still 9 V. The Polar Imager should be ready to collect ions lost to the poles!

5. **Hard X-ray Detector.** In the leftmost blue cabinet, look at the upper rack. Flip the power switch on the “Ortec High Voltage Power Supply”, a red light should turn on. Then flip the small switch all the way to the right. An orange light should turn on directly below.

6. **Gas Valve.** Directly opposite the X-ray power supply on the vacuum chamber is the inlet for the hydrogen (a small copper line). This puffs gas when triggered by a high voltage supply. Depress the small button to purge the line. Note; there is definitely a leak in the line somewhere, and it should be found. Next, turn on the HP 6827A that supplies 12 V to the high voltage supply for this gas valve. Note; using an HP for this is overkill. Make a 12 V supply to replace this.

7. **Isat Bias.** Next to the HP for the gas valve is a small box. Flip this to the “ON” position. If you are operating in “high density”, make sure the dial is set to 100 Ohms.

8. **Digitization.** Moving to the middle, blue cabinet, turn on all three "crate controllers" for crate 11 (middle), 12 (top) and 14 (on the ground). The digitizers for HBT also need to be turned on, ask someone downstairs for help. To ready the crates for digitization, log in to Spitzer and run "`crates_on`", twice. You will get an error the first time, ignore it.

9. **Magnet Power Supply.** The power supply is the huge orange box on the HBT level of the reactor room that say "ACME" on the front. It's a fickle relic. Don't do these operations out of order. Halfway down the stairs to the basement on the left is switch on the wall, this turns on the cooling pump. Flip it. Go back up the stairs and turn on the large red switch on the box marked "277/480 V", then go to the back of the ACME box and flip the breaker marked "Access to main circuit breaker " up high. All of the orange lights on the front will be off except for "Grounded" and possibly "Magnet Failure", which just means you haven't turned on LabVIEW yet. If you forget to turn on the water first, the "Water Flow Failure" light will come on and most likely stay on. This relay (located on the inside of the power supply front left door) sticks and needs to be reset manually. Reverse this procedure for power down.

10. **Taking Shots.** To take shots, on Spitzer run "`take_shot_ctx.py`". This will open the shot window. To take a shot, hit "New Shot", then "Prepare". Prepare the magnets in LabVIEW by flipping the "Interlock" switch (should turn yellow), then clicking the run arrow. Turn the magnets on with "Magnet Start" and wait till the magnet current levels out (roughly 1600 A), then quickly click "Fire", then "Magnet Stop" (big button). You just took your first shot.

C.2 Vacuum Procedures

This section covers the equipment involved in maintaining the roughly 10^{-7} Torr base pressure that makes for nice plasmas in CTX. This vacuum is achieved through three systems; a roughing pump, a turbomolecular pump and cryogenic pump. The "cryo" is the last stage in pumping as it can achieve the highest vacuum, but the others are used for initial pump down or as backup. The cryo should stay at a temperature under 20 K. I'll describe the use of this vacuum equipment in the context of bringing the vacuum system "up to air", which is required for installation of some probes, then back to a high vacuum state.

C.2.1 Going "Up to Air"

In preparation for installing or removing diagnostics, the vacuum of the chamber must be careful broken. In the case of a short or simple installation/removal of a diagnostic, the chamber can be filled with nitrogen (instead of air) as this prevents the accumulation of water in chamber, making for a faster pump down. In the case where someone needs to work in the machine, the chamber must be filled with air. Before doing either of these, close the gate valves to the cryo and/or turbo pumps and turn off the ionization gauge (button marked "Power" on the Varian Ionization Gauge Controller).

The difference between these two procedures are in the valves. Beside the microwave waveguide, there is a valve connecting the hydrogen fill line to the puffing line which can be bypassed into the chamber. By switching the regulator from the hydrogen bottle to the nitrogen, this line can be opened slowly to begin filling the chamber. Alternatively, to fill the chamber with air, set the bypass valve to the open copper line.

If going up to air for a while, the cryo should be switched off. This is not as simple as pushing a button as ice evaporates in the cold head and pressure builds. Left unattended, the cryo could burst! To safely warm the cryo, flip off the red switch on the compressor (box labeled "Ebara Cryocompressor 2.1") and monitor the pressure over the next couple hours. When the pressure goes

over 1 atmosphere, turn on the roughing pump with the switch on the wall behind the ionization gauge controller. Open the gate valve between the pump and the backing lines, then open the line on the back of the cryo. Do this periodically for the next couple hours. This procedure needs to be done a few times a year to remove the built up ice inside the coldhead, and is referred to as "regeneration."

C.2.2 Pump Down

The process of pumping down from atmospheric pressure is as follows; roughing pump till ~ 75 mTorr, turbo pump till 10^{-6} Torr, then cryo. To pump on the chamber with the roughing pump, close the backing valve on the turbo (assuming it's off, which it better be) and open the valve to the chamber. Turn on the roughing pump. Open the gate between the lines and the roughing pump to pump down.

Move the cryo thermocouple to the chamber port (backside near the vent valves). Using the lower gauges on the ionization gauge controller, monitor the vacuum. When it gets below 100 mTorr, begin turning on the turbo. This involves:

1. There is a blue panel below the ionization gauge controller. Switch the interlock to "OFF". There is a second interlock which trips if the roughing pressure is above 100 mTorr.

2. Switch the turbo on.

3. Watch the dial (with very strange units) increase. When it reaches roughly 0.7, close the roughing line to the chamber and open the backing to the turbo *in that order*.

4. Wait a few minutes, watching to make sure nothing fails. Try turning on the ionization gauge. It may not take immediately, sometime pressing and holding the button for a few seconds works. Once the ionization gauge is on, move the interlock switch to the middle. Only now is it safe to leave!

Pumping with the turbo can usually be left overnight or for an entire day or two. Once the pressure is low enough, turn the cryo on to begin cooling. When the cryo has cooled (< 20 K), close the gate to the turbo then open the gate to the cryo. Close the backing line and gate before the roughing pump, then switch off the turbo and roughing.

Appendix D

Polar Imager

Many of the Polar Imager detectors are not connected or no longer measure strong signals. Figure D.1 shows the currently working detectors and the digitizer inputs they map to. Read the diagram as follows; the different concentric rings correspond to the different radii of detectors (8). The circles on the rings are the detectors. If the circle has an "X", it is either not connected or malfunctioning. The numbers in the working detectors map to the A14 digitizer they are connected to according to the key in the upper left corner of the figure. Note the angles of the detectors are indicated on the outer boarder of the circle, and the "L" values (radii) are marked on the right hand side.

Interpretation of this figure is slightly tricky as this image is the "view" from inside the imager looking out. So a very small student *inside* the magnet would be facing the wall opposite the hallway windows, with the control room on his or her right. As an additional note, the "best" radii (most functional, clearest dynamics) are L = 3,4, and 5. The inner and outer most radii don't receive strong signals, and many are not working. As mentioned before, Ben Levitt's [46] and Brian Grierson's [50] theses provide more details on the design, circuitry and use of this powerful diagnostic.

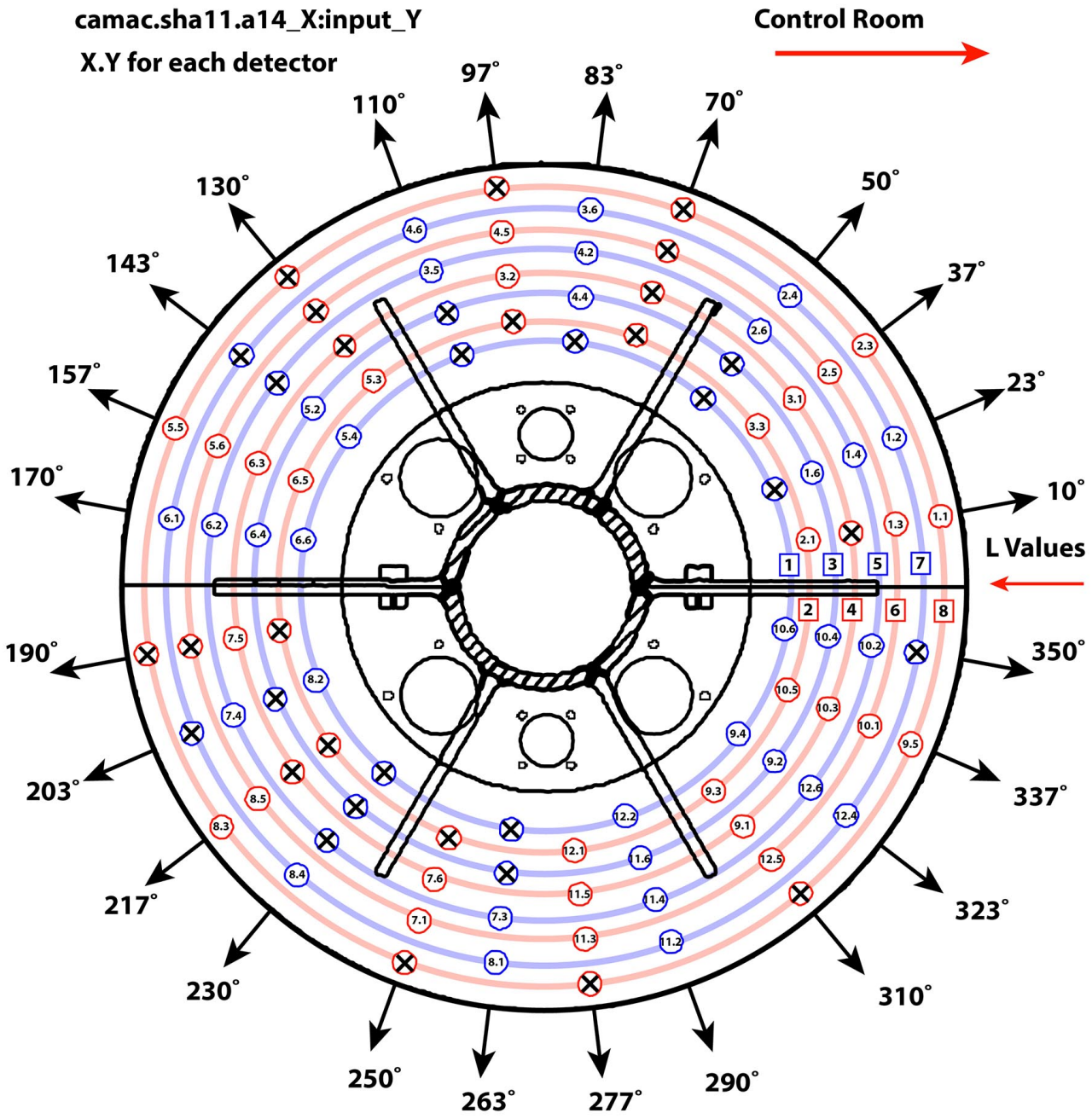

Figure D.1: Polar Imager detectors with mapping to digitizer locations.

Appendix E

Rake Array

A new diagnostic has been installed on CTX with the potential for multi-point measurement of azimuthal structure with high resolution. The "Rake" array consists of 31 tips, which alternate as floating potential probes (16) and ion saturation probes (15). With the 16 potential measurements, we can approximate the electric field at the location of the 15 measurements of density. Thus, we have 15 measurements of radial transport, as

$$\Gamma = \tilde{n}\tilde{v} = \tilde{n}\frac{\tilde{E} \times B}{B^2} \rightarrow \Gamma_r = \tilde{n}\frac{\tilde{E}_\varphi}{B} \tag{E.1}$$

Figure E.1 shows this diagnostic during the construction process and installation in CTX. The circuit for this diagnostic biases all ion saturation probes from one power supply while preventing cross-talk between the signals. Figure E.2 shows the completed circuit and circuit diagram for each floating potential and ion saturation probe. The ion saturation probes are biased to -180V. Notice the 1 mF cap which acts as a charge reservoir. The 100 kΩ resistor allows slow charging of the caps, but prevents coupling between the probes through the power supply. The complete PCB layout is shown in Figure E.3.

Figure E.1: Installation of Rake array (left top and bottom). 31 tips, alternating measurements of floating potential and density, give 15 measurements of radial transport (right, top and bottom).

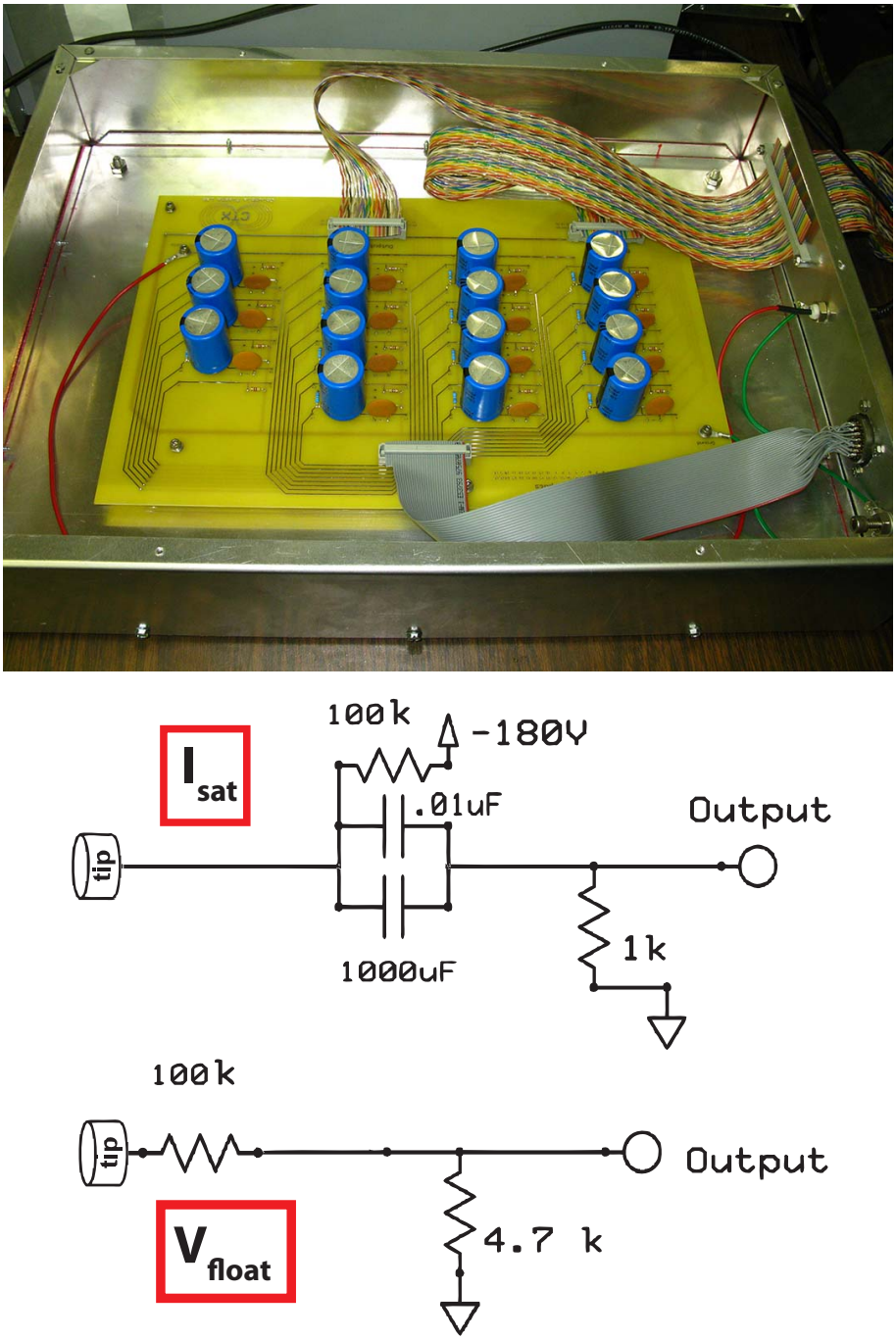

Figure E.2: Top, the complete circuit for the Rake array. The grey ribbon cable connects to the Rake array, the colored twisted pair ribbon cable connect to the digitizer. Bottom, the circuit diagram for the floating potential probes (left) and the ion saturation probes (right). The 1 mF cap and 100 kΩ resistor in the ion saturation circuit allow the use of one power supply for all probes.

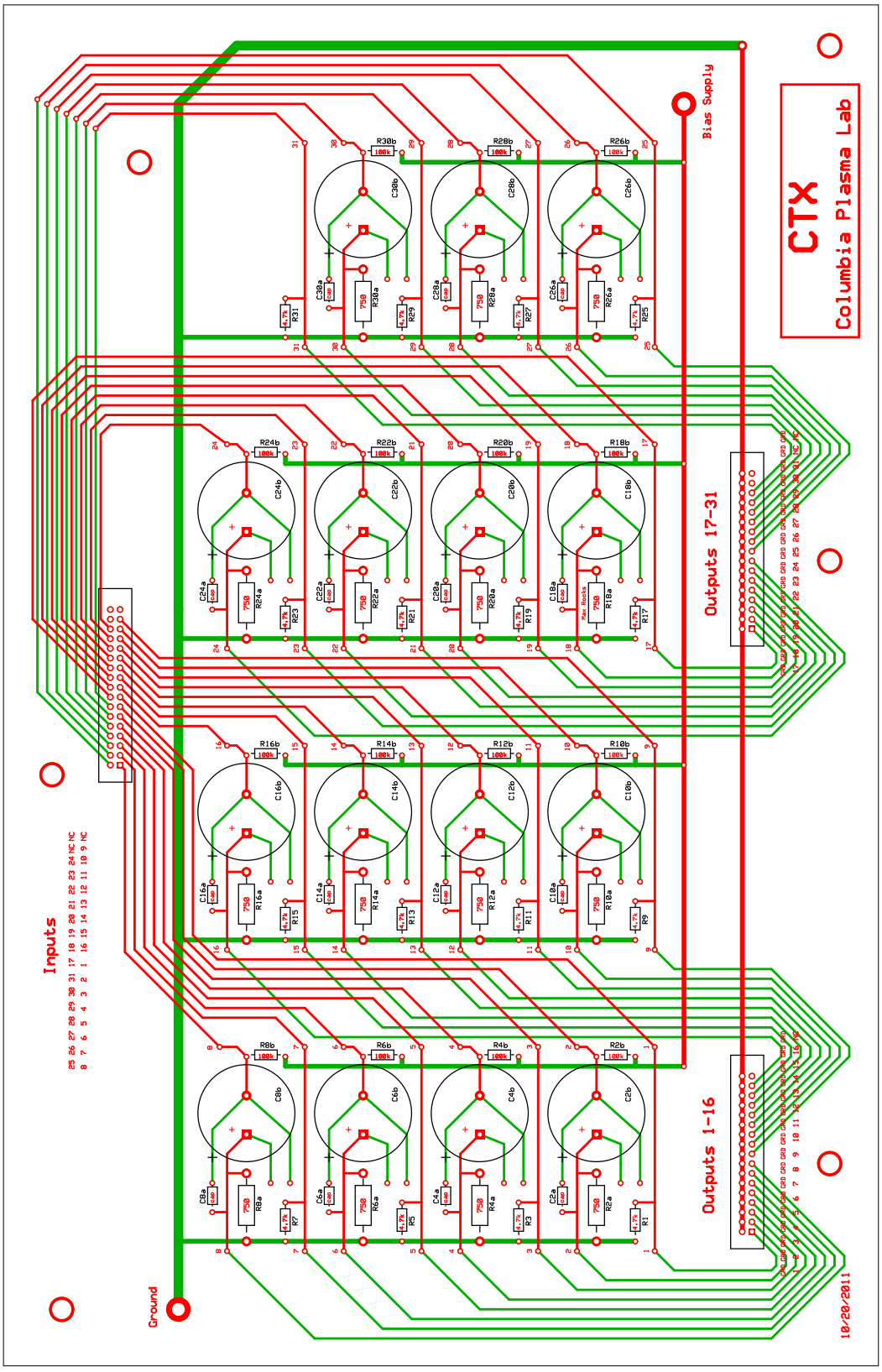

Figure E.3: PCB for the entire Rake array. Red is the top layer copper, green is the lower layer, black is the silk screen.

The output numbers are labeled on the PCB of Figure E.3 in increasing order from 1-31. The odd numbered outputs are the floating potential probes, the evens are ion saturation probes. These leave the enclosure is a twisted pair bundle and connect to LEMO adapters which are then connected to the various TRAQ digitizers in crate 14. At the time of this writing these connection are all labeled correctly. Figure E.4 shows the connector with tips 1 and 31 labeled. The numbers increase in the counter-clockwise direction.

Initial testing of the insertion of the Rake array shows strong signal levels on all tips, confirming the circuit design was functioning correctly. Signals which appeared to be arcing between tips were observed, and the bias to the ion saturation tips was reduced to -90V. While the diagnostic works as expected, the perturbation due to the insertion of 31 tips into the plasma is significant. Extracting the Rake to act as an edge diagnostic is an option, but due to oscillation of the magnet current ($\pm$100 A $\sim$ 6% of total current) the "edge" is poorly defined in CTX. It is the author's belief that this diagnostic could be made significantly less perturbative (hence more useful) by the removal of some of the tips. An array of 5 radial transport measurements might be more reasonable.

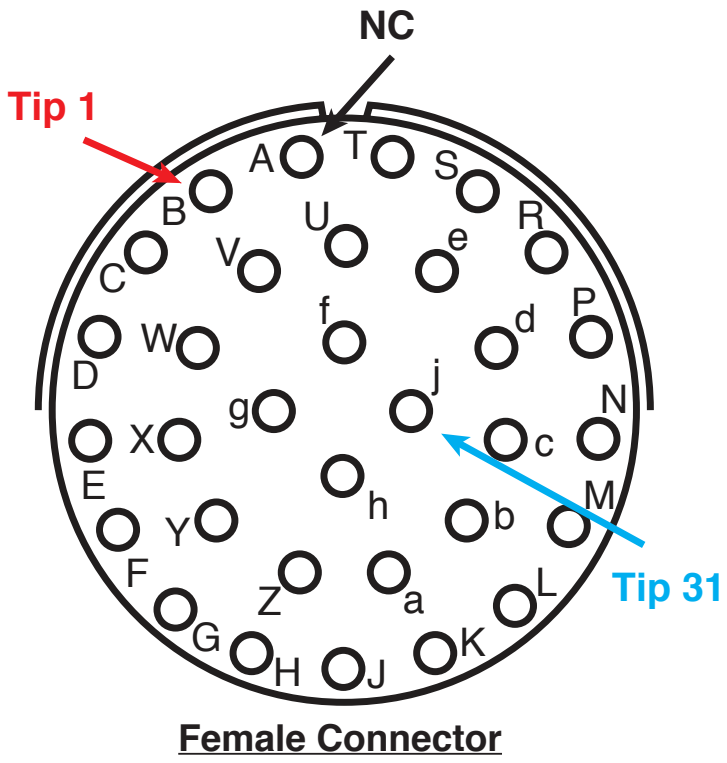

Figure E.4: Connector for the array to the PCB enclosure (female side). Tip 1 connects to "B", and the tips follow sequentially to Tip 31 on "j". "A" is not connected.

Appendix F

Filter Theory

This appendix covers some of the fundamentals of filter theory. Some significantly more detailed literature [56, 57, 55] may be of use to the interested reader.

F.1 Introduction to Filters

A filter is an electrical network which is designed to amplify or attenuate certain components of a signal. The amplification, or gain, from a filter is inherently dependent on frequency and is known as the amplitude response. Similarly, the phase shift applied by a filter depends on frequency and is referred to as the phase response. Control of the phase response is how our feedback system can apply an amplifying or suppressive response given an input signal.

All of the frequency response behavior is described by the filter's "transfer function". The transfer function is the ratio of the Laplace transforms of the filter's output signal to the input signal:

$$H(s) = \frac{V_{\text{out}}(s)}{V_{\text{in}}(s)} \tag{F.1}$$

We get the amplitude response and phase response from the transfer function as:

$$|H(s)| = |\frac{V_{\text{out}}(s)}{V_{\text{in}}(s)}| \qquad \text{amplitude response} \tag{F.2}$$

$$\arg(H(s)) = \arg \frac{V_{\text{out}}(s)}{V_{\text{in}}(s)} \qquad \text{phase response} \tag{F.3}$$

A simple example of a filter is shown on the left of Figure F.1, with a series capacitor followed by a resistor to ground. This configuration is a type of "high-pass" filter, which allows high frequencies to pass but removes low frequencies.

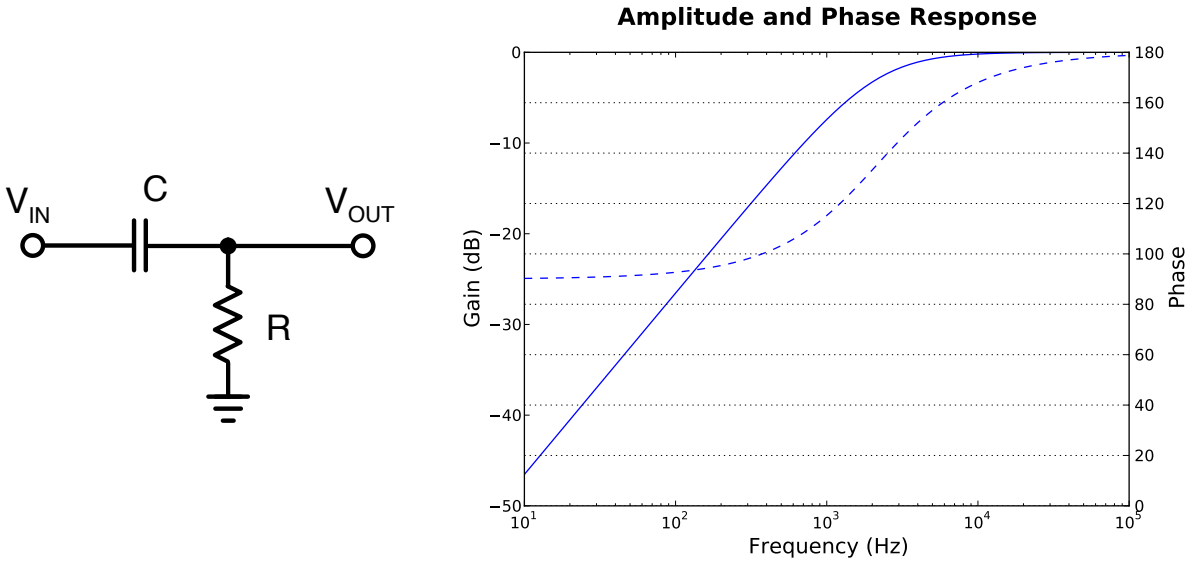

Figure F.1: High-pass filter and frequency response.

Here we find the transfer function as:

$$H(s) = \frac{V_{\text{out}}(s)}{V_{\text{in}}(s)} = \frac{\chi_R}{\chi_C + \chi_R} = \frac{R}{\frac{1}{sC} + R} = \frac{i\omega RC}{1 + i\omega RC} \tag{F.4}$$

where $s = i\omega$. One can see that $H(s)$ goes to unity as $\omega \to \infty$ and zero as the frequency drops to 0, attenuating the low frequency portion of the signal. The amplitude response (solid line) and phase response (dashed) are plotted on the right of Figure F.1. Notice that with the attenuation of frequency also comes a shifting in phase.

The order of a filter is the highest power of s in the transfer function, and is related to the number of capacitors and inductors in the network. The example just discussed had one capacitor and was a first-order filter. A higher order filter generally has more desirable properties (steeper roll-off, increasingly linear phase response, etc), but comes at the cost of having more components and being harder to design. The general transfer function for an n-order filter is given as:

$$H(s) = H_0 \frac{s^n + b_{n-1}s^{n-1} + b_{n-1}s^{n-1} + \ldots + b_0}{s^n + a_{n-1}s^{n-1} + a_{n-1}s^{n-1} + \ldots + a_0} \tag{F.5}$$

where the coefficients a_i and b_i are chosen by the type of filter and completely determine the filter's characteristics.

In the high-pass filter example, the range of frequencies which were allowed to pass, known as the passband, are all frequencies higher than the cutoff frequency. The cutoff frequency is defined as the point at which the gain has fallen by -3 dB. The range of frequencies where the signal has been significantly attenuated is known as the stopband. The sharpness of the transition between the passband and stopband is a parameter we can tune, quantified by Q, the quality factor of the filter.

In addition to the high-pass filter just discussed there are several other filter types. A low-pass filter is the reciprocal to the high-pass filter, allowing low frequencies and removing higher frequencies. If we combine a low and high pass filter correctly, we can select a portion of the spectrum that is passed by the filter, this is known as a band-pass filter. It's reciprocal, the notch-filter, removes only a portion of the passed frequencies.

The last basic filter type is the all-pass filter. An all-pass filter is designed to apply a phase shift to the signal, but have unity amplitude response for all frequencies. These are often used to correct the phase response imposed by other circuit components, but can also be used in a feedback system to apply a desired phase shift between the sensor and actuator (electrode) signals.

An ideal filter would have constant gain for a desired range of frequencies, and a gain of zero for all other frequencies with an discontinuous boundary between the passband and stopband. This is clearly not physically attainable so approximations are made. The steepness and sharpen of the gain roll-off, both near the cutoff frequency and far from it, can be adjusted by increasing the order

of the filter and choice of coefficients. Increasing the order of the filter comes at the cost of adding "ripple" to the passband and stopband. This ripple applies a non-monotonic gain with frequency to your signal. Finally, the transient response of your filter to an input can exhibit "ringing". Higher order filters and higher Q will result in increased ringing.

Optimizing a filter for a particular application depends on the quantities you care about. There are three classic filter polynomials which are optimized for specific filter properties. Butterworth filters have maximally-flat amplitude response with little to no passband ripple, and have medium roll-off steepness. Chebyshev filters trade increased ripple in the passband for a steeper roll-off near the cutoff frequency. Bessel filters have the most mild roll-off of the three, but achieve more linear phase response in the passband. Increasing the order of a Bessel filter makes this response increasingly linear.

For the nature of feedback we wish to apply, a Bessel-type filter is the best choice. As mentioned, the difference between filter types is merely the choice in coefficients used in equation F.5. These are commonly tabulated in frequency-normalized form [55].

The implementation of a filter design can be done in two ways. Similar to the example above, an LRC filter is composed of only passive elements; resistors, capacitors and inductors. These are convenient when the application high frequency (> 1 MHz) or noise is as issue. A significant disadvantage of LRC filter is the the use of inductors, which become very large and expensive for low frequency applications. In addition to this, the complexity of high order filter design, low input impedance and the inability to apply signal gain makes the use of passive filters a challenge. For lower frequency applications, the use of "active" filters, using operation amplifiers, greatly simplifies these issues.

F.2 Active Filters

As mentioned above, active filters have many advantages. Operational amplifiers act to effectively replace the inductors in the passive circuits, and allow us to also apply amplification to the input

signal. The active analog of the high-pass filter from the last section is shown in Figure F.2

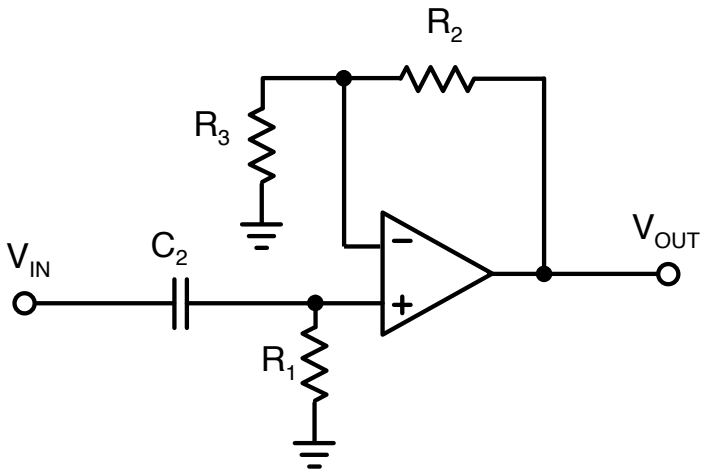

Figure F.2: A first order high-pass filter.

Creating higher-order filters is simplified with active component as the cascading of first and second order filters can be used to produce an n-order filter. We can see this directly from the transfer function F.5 by putting the polynomials in factored form. This factoring can be manipulated to be the product of first and second-order polynomials, relating to first and second-order filters. For an n-order filter:

$$H(s) = H_0 \frac{(s^2 + b_{11}s + b_{10})(s^2 + b_{21}s + b_{20})\dots}{(s^2 + a_{11}s + a_{10})(s^2 + a_{21}s + a_{20})\dots} \qquad \text{even order} \tag{F.6}$$

$$H(s) = H_0 \frac{(s + b_{10})(s^2 + b_{21}s + b_{20})\dots}{(s + a_{10})(s^2 + a_{21}s + a_{20})\dots} \qquad \text{odd order} \tag{F.7}$$

The product of these terms represents the cascading of these low-order filters in series to produce the n-order filter. Second-order active filters come in two main topologies, Sallen-Key and Multiple-Feedback, shown in Figure F.3. Multiple-Feedback filters are generally used in filters with high Q and need high gain. For our application we used Sallen-Key, so we will focus on these. The two resistors (R_3 and R_4 in Figure F.3) allow for independent adjustment of gain, as $H_0 = 1 + R_4/R_4$, but unity gain can be set choosing $R_4 = 0$, and letting $R_3 \to \infty$.

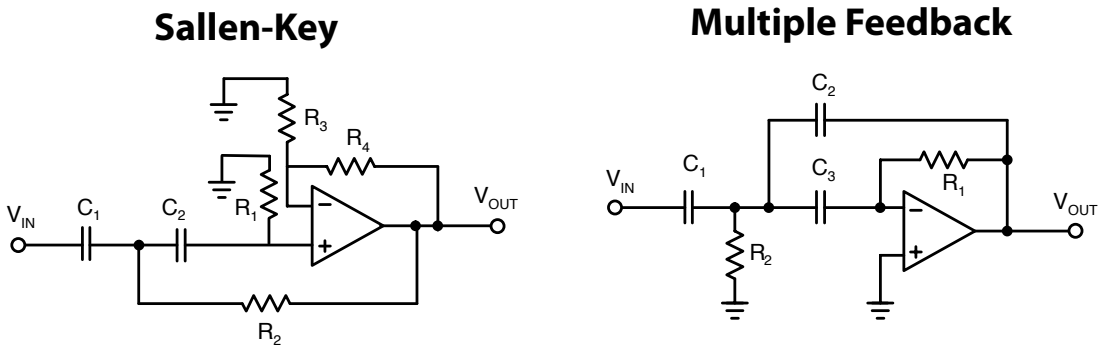

Figure F.3: Sallen-Key and MFB second-order high-pass filter topologies.

The second-order Sallen-Key high-pass filter on the left of Figure F.3 is the topology used in the feedback circuit for improved roll off and phase response.

Appendix G

Additional Circuits

G.1 Triggering Circuit

In order to rapidly turn the feedback on and off, a triggering circuit was implemented using two AQY-277 optical relays. A 5 V pulse from the Jorway triggered the switches. Turn off time was around 20 μs, while the turn on time was significantly longer (50 – 100 μs). This switch was positioned after the 12 μF cap but before the divider for electrode voltage digitization. The current was also measured after the switch. A diagram of the switch is shown in Figure G.1.

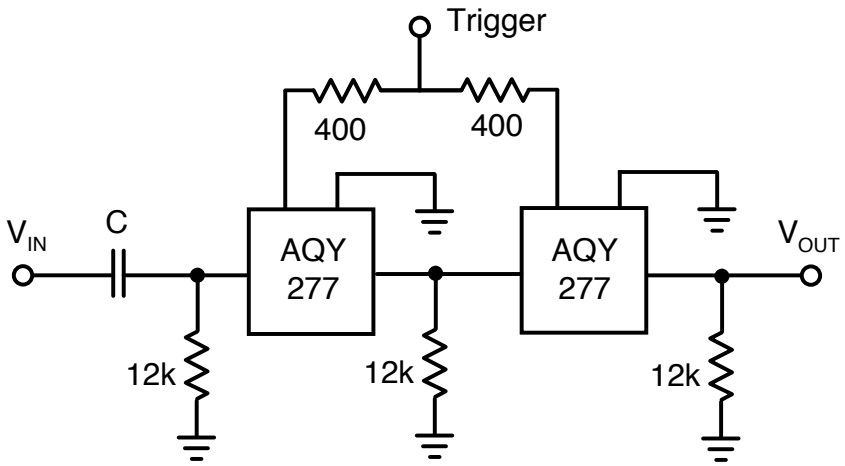

Figure G.1: Triggering circuit for feedback experiments.

G.2 Isolation Transformer

To properly decouple the HP amplifier from ground for the "zero-net-current" experiments, an isolation transformer was used to connect the feedback circuit output to the inputs of the HP. This allowed the bias electrodes to always draw equal and opposite current without ground reference. An A262A2E audio transformer was used for this purpose and a circuit diagram is sketched in Figure G.2

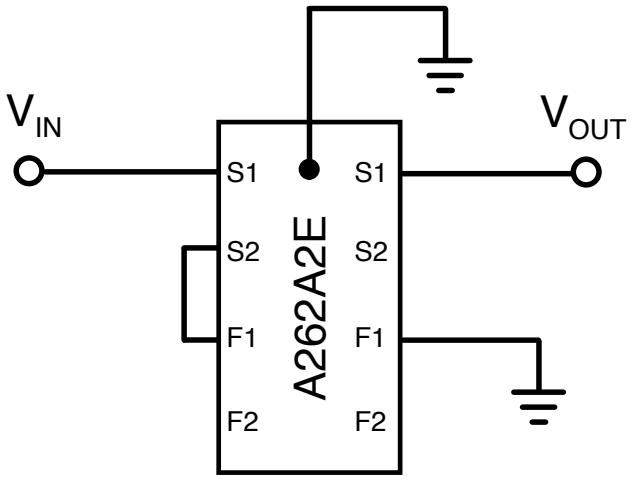

Figure G.2: Isolation transformer for "zero-net-current" experiments.

Appendix H

HEIsim Equations and Numerical Methods

This is a detailed derivation of the equations used to model and numerically solve the Hot Electron Interchange instability. Kinetic electrons are evolved with a guiding center Hamiltonian, using Hamilton's equations of motion to describe the dynamics. The ions are treated as a cold fluid, moving due to E×B and polarization drifts. These two species are coupled via Poisson's equation, and a nonlinear solve is performed to find the rate of change of the potential from the constrained current. All of these equations are in Gaussian units. The derivation of these equations in dipole coordinates will be explained, then some of the related numerical methods will be discussed. The addition of a particle conserving source/sink term for the continuity equations to reproduce high density plasma [50] is also described.

H.1 Equations

The self-consistent evolution of interchange dynamics can be described by the motion of kinetic electrons and cold, fluid ions coupled by the bounce-averaged form of Poisson's equation:

$$\frac{\partial F_e}{\partial t} + \nabla \cdot (F_e V_e) = 0 \qquad \frac{\partial n_i}{\partial t} + \nabla \cdot (n_i V_i) = 0 \qquad \nabla^2 \Phi = -4\pi\rho$$

The electron distribution function is represented by multiple electron species at different energies,

μB. Due to the sufficient separation in frequency of the gyro, bounce and drift dynamics, we can assume that μ and J are conserved. In addition, it has been observed that the interchange dynamics are flute-like, $k_{\|} \approx 0$ [46], justifying the use of flux-tube averages to reduce the problem's dimensionality.

H.1.1 Poisson's Equation

We derive Poisson's equation in dipole coordinates starting with the microscopic version of Gauss's Law:

$$\nabla \cdot E = -\nabla \cdot \nabla\Phi = 4\pi\rho$$

where ρ is the total charge. In covariant notation, the Laplacian is:

$$\nabla^2\Phi = |B|^2 \frac{\partial}{\partial\psi}\left(\frac{|\nabla\psi|^2}{|B|^2}\frac{\partial\Phi}{\partial\psi}\right) + |B|^2 \frac{\partial}{\partial\chi}\left(\frac{|\nabla\chi|^2}{|B|^2}\frac{\partial\Phi}{\partial\chi}\right) + |B|^2 \frac{\partial}{\partial\varphi}\left(\frac{|\nabla\varphi|^2}{|B|^2}\frac{\partial\Phi}{\partial\varphi}\right)$$

Taking a flux-tube average (killing the $\frac{\partial}{\partial\chi}$ term):

$$\begin{aligned} < \nabla^2\Phi > = & \int_{-\infty}^{+\infty} \frac{\partial}{\partial\psi}\left(\frac{d\chi}{|\nabla\varphi|^2}\frac{\partial\Phi}{\partial\psi}\right) + \int_{-\infty}^{+\infty} \frac{\partial}{\partial\varphi}\left(\frac{d\chi}{|\nabla\psi|^2}\frac{\partial\Phi}{\partial\varphi}\right) \\ = & h_\varphi \frac{\partial^2\Phi}{\partial\varphi^2} + h_\psi \frac{\partial^2\Phi}{\partial\psi^2} = \int_{-\infty}^{+\infty} (-4\pi e\rho)\frac{d\chi}{B^2} = -4\pi e(N_i - N_e) \end{aligned}$$

where h_ψ and h_φ are geometric terms given as:

$$h_\psi = \int_{-\infty}^{+\infty} \frac{d\chi}{|\nabla\varphi|^2} = 4M \qquad\qquad h_\varphi = \int_{-\infty}^{+\infty} \frac{d\chi}{|\nabla\psi|^2} = 2\frac{M}{\psi^2}$$

H.1.2 Cold Ion Fluid

Cold ions in a dipole magnetic field move under the influence of $E \times B$ and polarization drifts. The electric field in terms of potential is given as:

$$E = -\nabla\Phi = -\frac{\partial\Phi}{\partial u^i}\nabla u^i = -\frac{\partial\Phi}{\partial\psi}\nabla\psi - \frac{\partial\Phi}{\partial\varphi}\nabla\varphi$$

So our expressions for the $E \times B$ and polarization drifts become:

$$\vec{v}_E = c\frac{\vec{E}\times\vec{B}}{B^2} = -c\frac{\partial\Phi}{\partial\psi}\frac{\nabla\varphi}{|\nabla\varphi|^2} + c\frac{\partial\Phi}{\partial\varphi}\frac{\nabla\psi}{|\nabla\psi|^2}$$
$$\vec{v}_P = \frac{c}{\omega_{ci}B}\frac{dE}{dt} = -c\frac{M_i}{eB^2}\frac{d\nabla\Phi}{dt} = -c\frac{M_i}{eB^2}\frac{d}{dt}\Big[\frac{\partial\Phi}{\partial\psi}\nabla\psi + \frac{\partial\Phi}{\partial\varphi}\nabla\varphi\Big]$$

In the absence of ion sources/sinks, we transform the ion continuity equation into dipole coordinates and plug in our velocities:

$$-\frac{\partial n_i}{\partial t} = B^2\frac{\partial}{\partial\psi}\Big[c\frac{n_i}{B^2}\Big(\frac{\partial\Phi}{\partial\varphi} - \frac{M_i}{eB^2}|\nabla\psi|^2\frac{d}{dt}\frac{\partial\Phi}{\partial\psi}\Big)\Big] + B^2\frac{\partial}{\partial\varphi}\Big[c\frac{n_i}{B^2}\Big(-\frac{\partial\Phi}{\partial\psi} - \frac{M_i}{eB^2}|\nabla\varphi|^2\frac{d}{dt}\frac{\partial\Phi}{\partial\varphi}\Big)\Big]$$

and taking a flux tube average,

$$-\frac{\partial N_i}{\partial t} = \frac{\partial}{\partial\psi}\Big[cN_i\Big(\frac{\partial\Phi}{\partial\varphi} - \varepsilon_\psi\frac{d}{dt}\frac{\partial\Phi}{\partial\psi}\Big)\Big] - \frac{\partial}{\partial\varphi}\Big[cN_i\Big(\frac{\partial\Phi}{\partial\psi} + \varepsilon_\varphi\frac{d}{dt}\frac{\partial\Phi}{\partial\varphi}\Big)\Big]$$

where N is the flux-tube averaged density. The density weighted, flux-tube averaged coefficients for the polarization drifts are found by assuming a $\sin\theta$ distribution of density along a field line:

$$\varepsilon_\varphi = \frac{1}{\delta V}\int_{-\infty}^{+\infty}\frac{d\chi}{B^2}\frac{n_i M_i}{e\langle n_i\rangle B^2}|\nabla\varphi|^2 \approx 0.66\frac{M^2 B_0}{\psi^4\omega_{ci0}}$$
$$\varepsilon_\psi = \frac{1}{\delta V}\int_{-\infty}^{+\infty}\frac{d\chi}{B^2}\frac{n_i M_i}{e\langle n_i\rangle B^2}|\nabla\psi|^2 \approx 0.77\frac{M^2 B_0}{\psi^2\omega_{ci0}}$$

H.1.3 Kinetic Electron Dynamics

The motion of deeply trapped ($J \approx 0$) electrons in a curl free magnetic field is given by the guiding center drift Hamiltonian [65] with Hamilton's equations:

$$H = \frac{\mu c B}{e} - c\Phi \qquad \dot{\varphi} = \frac{\partial H}{\partial\psi} = \frac{\mu c}{e}\frac{\partial B}{\partial\psi} - c\frac{\partial\Phi}{\partial\psi} \qquad \dot{\psi} = -\frac{\partial H}{\partial\varphi} = c\frac{\partial\Phi}{\partial\varphi}$$

where $\mu = m_e v^2/2B$.

For time scales significantly slower than the gyration and bounce periods, μ and J are preserved quantities as an electron moves across field lines. The Vlasov equation for the electron distribution function is given as:

$$\begin{aligned}\frac{dF_e}{dt} &= \frac{\partial F_e}{\partial t} + \frac{\partial\vec{x}}{\partial t}\cdot\frac{\partial F_e}{\partial\vec{x}} = \frac{\partial F_e}{\partial t} + \frac{\partial}{\partial\varphi}(\dot{\varphi}F_e) + \frac{\partial}{\partial\psi}(\dot{\psi}F_e) = 0\\ &= \frac{\partial F_e}{\partial t} + \frac{\partial}{\partial\varphi}\Big[(\frac{\mu c}{e}\frac{\partial B}{\partial\psi} - c\frac{\partial\Phi}{\partial\psi})F_e\Big] + \frac{\partial}{\partial\psi}\Big[c\frac{\partial\Phi}{\partial\varphi}F_e\Big] = 0\end{aligned}$$

We use a bounce-averaged distribution, $F_e = F_e(\mu, J, \psi, \varphi, t)$, where F_e is given as the sum of a cold and hot electron population:

$$F_e = N_{i0}(\psi)\Big([1-\alpha(\psi)]\delta(\mu)\delta(J) + \alpha(\psi)G(\mu)\delta(J)\Big), \qquad G(\mu) = \frac{\mu^{l-1}l^l}{\mu_0^l\Gamma(\mu)}e^{-\mu l/\mu_0}$$

$G(\mu)$ is the electron distribution in μ. Integration over velocity space then returns the number of

electrons per unit flux, $N_e = \int d\mu dJ F_e$. The first azimuthal term represents the hot electron drift frequency $\omega_d \equiv \frac{\mu c}{e}\frac{\partial B}{\partial \psi} = \frac{\mu c}{e}\frac{3B}{\psi}$.

H.1.4 Normalization

We make these equations dimensionless, normalizing them with parameters evaluated at the profile peak (heating resonance). Starting with Poisson's equation, we normalize the following quantities as:

$$\frac{\psi}{\psi_0} \equiv y, \qquad \frac{N_i}{N_i 0} \equiv \hat{N}_i \qquad \frac{e\Phi}{\mu_0 B_0} \equiv \hat{\Phi}, \qquad \omega_{dh0} t \equiv \hat{t} \qquad \frac{\mu}{\mu_0} \equiv \hat{\mu}$$

where the x_0 quantities are defined at the profile peak. We multiply Poisson's equation through by $e\psi^2/M\mu_0 B_0$:

$$\frac{2}{y^2}\frac{\partial^2 \hat{\Phi}}{\partial \varphi^2} + 4\frac{\partial^2 \hat{\Phi}}{\partial y^2} = -4\pi e \frac{eL_0}{\mu_0}\frac{N_{i0}}{N_{i0}}(N_i - N_e) = -.91\frac{L_0^2}{\lambda_{D0}^2}(\hat{N}_i - \hat{N}_e)$$

where $\lambda_{D0}^2 = \mu_0 B_0 / 4\pi e^2 \langle n_{i0} \rangle$.

We normalize the ion continuity equation, dividing by $\omega_{dh0} N_{i0}$,

$$\frac{\partial \hat{N}_i}{\partial \hat{t}} + \frac{\partial}{\partial y}\Big[\hat{N}_i\Big(\frac{1}{3}\frac{\partial \hat{\Phi}}{\partial \varphi} - \hat{\varepsilon}_y \frac{d}{d\hat{t}}\frac{\partial \hat{\Phi}}{\partial y}\Big)\Big] - \frac{\partial}{\partial \varphi}\Big[\hat{N}_i\Big(\frac{1}{3}\frac{\partial \hat{\Phi}}{\partial y} + \hat{\varepsilon}_\varphi \frac{d}{d\hat{t}}\frac{\partial \hat{\Phi}}{\partial \varphi}\Big)\Big] = 0$$

$$\hat{\varepsilon}_\varphi = \frac{0.66}{3y^4}\frac{\omega_{dh0}}{\omega_{ci0}} \qquad \hat{\varepsilon}_y = \frac{0.77}{3y^2}\frac{\omega_{dh0}}{\omega_{ci0}}$$

Finally, dividing the electron equation by ω_{dh0}, with the same normalization for $E \times B$ drift:

$$\frac{\partial F_e}{\partial \hat{t}} + \frac{\partial}{\partial \varphi}\Big[(\frac{\omega_{dh}}{\omega_{dh0}} - \frac{\partial \hat{\Phi}}{\partial \psi})F_e\Big] + \frac{\partial}{\partial y}\Big[\frac{\partial \hat{\Phi}}{\partial \varphi}F_e\Big] = 0$$

where $\frac{\omega_{dh}}{\omega_{dh0}} = \hat{\mu}y^2$.

This normalization shows that the simulation is only dependent on two parameters, the ratio of L_0 to λ_{D0} and hot electron drift frequency over the ion cyclotron frequency.

H.2 Numerical Techniques

The simulation solves the finite-difference approximations to the coupled equations given above. The potential is advanced with a nonlinear solve of the equation for charge continuity. Due to the periodic boundary condition in the φ direction, employing a pseudo-spectral method effectively reduces the dimensionality of the finite difference problem to be solved. We implement a numerical stepping scheme for advancing the ion and electron populations based on a flux conserving method by Zalesak [66].

H.2.1 Trapezoidal Leap-Frog Method

A second-order trapezoidal leap-frog algorithm for explicit time integration is implemented to advance the ion and electron populations and potential. First, the ion and electron populations are advanced a half-step in time by using the existing potential. At this half-step, a new potential and charge density are calculated using the intermediate values of F_e and N_e, and with these we find the intermediate fluxes. With the intermediate fluxes, we advance the populations a full trapezoidal time step, then recompute the potential and charge density. These two steps are identical aside from the time-base of the terms being advanced. If we have a population, $f(t)$, with a rate of change $\dot{f} = -\nabla \cdot \Gamma$, we can describe this method as:

$$f_{t-\Delta t/2} = \frac{1}{2}(f_t + f_{t-\Delta t})$$

$$f_{t+\Delta t/2} = f_{t-\Delta t/2} - \Delta t \Delta \Gamma_t$$

$$f_{t+\Delta t} = f_t - \Delta t \Delta \Gamma_{t/2}$$

where $\Gamma = \Gamma(f(t), \Phi(t), \dot{\Phi}(t))$ is the flux calculated at each half-step, which includes solving for the potential. In this approach, the populations are advanced by fluxes which are always a half-step off in time.

H.2.2 Nonlinear Solve for $\frac{\partial \hat{\Phi}}{\partial t}$

To advance the potential at each half-step, we can consider the rate of change of charge density. We can find this by equating the time derivative of Poisson's equation to the combination of the ion and electron dynamic equations:

$$\frac{2}{y^2}\frac{\partial^2 \dot{\hat{\Phi}}}{\partial \varphi^2} + 4\frac{\partial^2 \dot{\hat{\Phi}}}{\partial y^2} = -.91\frac{L_0^2}{\lambda_{D0}^2}\frac{\partial \hat{\rho}}{\partial \hat{t}} = -.91\frac{L_0^2}{\lambda_{D0}^2}\left(\frac{\partial \hat{N}_i}{\partial \hat{t}} - \frac{\partial \hat{N}_e}{\partial \hat{t}}\right)$$
$$= .91\frac{L_0^2}{\lambda_{D0}^2}\left(\frac{\partial}{\partial \varphi}\left[\hat{\rho}\frac{\partial \hat{\Phi}}{\partial y} + \hat{N}_i \hat{\varepsilon}_\phi \frac{\partial \dot{\hat{\Phi}}}{\partial \varphi} + \Sigma \hat{\mu} y^2 F_{e,u}\right] - \frac{\partial}{\partial y}\left[\hat{\rho}\frac{\partial \hat{\Phi}}{\partial \varphi} - \hat{N}_i \hat{\varepsilon}_y \frac{\partial \dot{\hat{\Phi}}}{\partial y}\right]\right)$$

where $\hat{\rho}$ is the difference of the normalized flux-tube averaged ion density and the electron distribution function integrated over velocity space.

We note the $\dot{\hat{\Phi}}$ terms on both sides of our rate equation. To efficiently implement a pseudo-spectral technique, we bring the azimuthally symmetric part of the polarization terms ($\bar{N}_i = \hat{N}_i - \tilde{N}_i$) to the LHS. We rewrite the equations with an effective dielectric:

$$\frac{2}{y^2}\frac{\partial}{\partial\varphi}\hat{\epsilon}_\varphi(y)\frac{\partial\dot{\hat{\Phi}}}{\partial\varphi}+4\frac{\partial}{\partial\psi}\hat{\epsilon}_y(y)\frac{\partial\dot{\hat{\Phi}}}{\partial y}=.91\frac{L_0^2}{\lambda_{D0}^2}\Big(\frac{\partial}{\partial\varphi}\Big[\hat{\rho}\frac{\partial\hat{\Phi}}{\partial y}+\tilde{N}_i\hat{\varepsilon}_\phi\frac{\partial\dot{\hat{\Phi}}}{\partial\varphi}+\Sigma\hat{\mu}y^2F_{e,u}\Big]-\frac{\partial}{\partial y}\Big[\hat{\rho}\frac{\partial\hat{\Phi}}{\partial\varphi}-\tilde{N}_i\hat{\varepsilon}_y\frac{\partial\dot{\hat{\Phi}}}{\partial y}\Big]\Big)$$

where

$$\hat{\epsilon}_\varphi\approx 1+\frac{\bar{N}_i}{9.99y^2}\frac{L_0^2}{\lambda_{D0}^2}\frac{\omega_{dh0}}{\omega_{ci0}}\qquad\qquad\hat{\epsilon}_y\approx 1+\frac{\bar{N}_i}{17.1y^2}\frac{L_0^2}{\lambda_{D0}^2}\frac{\omega_{dh0}}{\omega_{ci0}}$$

The above equation is iteratively solved for the time rate of change in potential at the half and full leap-frog steps. This must be done before advancing the ions as the polarization velocity depends on the rate of change in potential.

H.2.3 Flux-Corrected Transport Algorithm

The $\Delta\Gamma$ expression in the Leap-Frog section is an operator representing the fourth order FCT process. "High-order" fluxes improve the spatial resolution of the time step, but can cause numerical oscillations and lead to instability. To limit these oscillations, "low-order" fluxes are used as an artificial diffusion, specifically chosen to prevents numerical artifacts from high-order methods to develop. The process at each time step is:

1. Find the ion and electron velocities.
2. Find the ion and electron low and high order fluxes, F^L and F^H.
3. Define the anti-diffusive flux, $A \equiv F^H - F^L$
4. Limit A so as not to produce or enhance extrema in step 5.
5. Find time advanced populations with the limited A.

The low order flux is given by an "upwind" differencing scheme and an ad-hoc diffusion:

$$\Gamma^L_\varphi(l,k+1/2) = \frac{1}{2}[v_\varphi(l,k+1)+v_\varphi(l,k)]F^{DC}(l,k+1/2) - \frac{1}{8}\frac{\Delta\varphi}{\Delta t}[F^0(l,k+1)-F^0(l,k)]$$
$$\Gamma^L_y(l+1/2,k) = \frac{1}{2}[v_y(l+1,k)+v_y(l,k)]F^{DC}(l+1/2,k) - \frac{1}{8}\frac{\Delta y}{\Delta t}[F^0(l+1,k)-F^0(l,k)]$$

where F^{DC} represents the flux from an "upwind" donor cell. The high-order flux is a fourth order finite differencing known as "ZIP" form:

$$\begin{aligned}
\Gamma^H_\varphi(l,k+1/2) &= \frac{2}{3}[v_\varphi(l,k)F(l,k+1)+v_\varphi(l,k+1)F(l,k)] \\
&\quad - \frac{1}{12}[v_\varphi(l,k)F(l,k+2)+v_\varphi(l,k+2)F(l,k) \\
&\qquad + v_\varphi(l,k-1)F(l,k+1)+v_\varphi(l,k+1)F(l,k-1)] \\
\Gamma^H_y(l+1/2,k) &= \frac{2}{3}[v_y(l,k)F(l+1,k)+v_y(l+1,k)F(l,k)] \\
&\quad - \frac{1}{12}[v_y(l,k)F(l+2,k)+v_y(l+2,k)F(l,k) \\
&\qquad + v_y(l-1,k)F(l+1,k)+v_y(l+1,k)F(l-1,k)]
\end{aligned}$$

With these two fluxes, we define $A(l,k) = \Gamma^H - \Gamma^L$, and then limit this flux as described in [66] to prevent the formation of new extrema, or the enhancement of existing extrema. We use a centered differencing method to represent the convection velocities of the ions and electrons.

H.2.4 Numerical Dissipation in Potential

To prevent numerical instability in advancing the potential, dissipation is added. This also acts as the physical nonresonant dissipation which limits the frequency sweeping observed in HEIs. We advance the potential in the leap-frog manner as:

$$\Phi_{t-\Delta t/2} = \frac{1}{2}(\Phi_t + \Phi_{t-\Delta t})$$
$$\Phi_{t+\Delta t/2} = \Phi_{t-\Delta t/2} + \Delta t\dot{\Phi}_t - (-1)^k \Delta t\nu\nabla^{2k}\Phi_t$$
$$\Phi_{t+\Delta t} = \Phi_t + \Delta t\dot{\Phi}_{t+t/2} - (-1)^k \Delta t\nu\nabla^{2k}\Phi_{t+t/2}$$

k sets the dissipation length scale, and adjustment of ν sets the nonresonant dissipation for limiting the frequency sweeping.

H.3 Particle Conserving Source/Sink

To reproduce dynamics related to driven turbulence, we require a mechanism to maintain the unstable profile. Grierson implemented a conservative source and sink of particles and electron energy [50]. In normalized magnetic coordinates, the particle continuity equation becomes:

$$\frac{\partial \hat{N}}{\partial \hat{t}} + \frac{\partial}{\partial \varphi}(\hat{N}v_\varphi) + \frac{\partial}{\partial y}(\hat{N}v_y) = 1.8\hat{D}h_D y^2 \frac{\partial^2 \hat{N}}{\partial \varphi^2} + 3.2\hat{D}\frac{\partial}{\partial y}\Big[h_D \frac{\partial}{\partial y}(y^4 \hat{N})\Big] + \hat{D}D_s h_s \tag{H.1}$$

h_s and h_D are the normalized source and diffusion profiles. Conservation requires the number of particles in the volume to be fixed, therefore the volume integral of the above equation yields:

$$D_s = \frac{-\int 1.8h_D y^2 \frac{\partial^2 \hat{N}}{\partial \varphi^2} - 3.2\frac{\partial}{\partial y}\Big[h_D \frac{\partial}{\partial y}(y^4 \hat{N})\Big] d^2x}{\int h_s d^2x} \tag{H.2}$$

At every time step D_s is calculated, and the ion and electron grids are updated with a source/sink grid that sums to zero. For the electrons we are also conserving energy, so the grid integrated over μ sums to zero as well.

Notice that $\hat{D}$ is on all the new terms, so the effect of this source/sink can be tuned simply by

varying this parameter. A value for $\hat{D}$ is found that maintains a slightly unstable density profile and results in the onset of radially broad convective cells.